UC Berkeley
UC Berkeley Electronic Theses and Dissertations

Title
Optically Functional Nanomaterials: Optothermally Responsive Composites and Carbon Nanotube Photovoltaics

Permalink
https://escholarship.org/uc/item/95v051kv

Author
Okawa, David

Publication Date
2010

Peer reviewed|Thesis/dissertation

eScholarship.org Powered by the California Digital Library
University of California

Optically Functional Nanomaterials:
Optothermally Responsive Composites and Carbon Nanotube Photovoltaics

by

David Christopher Okawa

A dissertation submitted in partial satisfaction of the

requirements for the degree of

Doctor of Philosophy

in

Chemistry

in the

Graduate Division

of the

University of California, Berkeley

Committee in charge:

Professor Jean M. J. Fréchet, Co-chair
Professor Alex Zettl, Co-chair
Professor Peidong Yang
Professor Michael Crommie

Spring 2010

Table of Contents

Acknowledgments

As a graduate student, I was given the opportunity to work in an inherently interdisciplinary position, straddling the Chemistry and Physics departments as a Materials Chemist at UC Berkeley. This came about after spending my undergraduate career investigating reaction methodology and drug discovery: essentially developing an understanding for the way molecules interact, react, and work together – all inherently on the nanoscale. At the same time, I became interested in the expanding field of nanostructured materials. This lead me to spend a year in the Zettl group exploring the synthesis, characterization and thermal properties of inorganic nanostructures, in particular carbon and boron nitride nanotubes.

With this unique combination of experiences, I joined the Chemistry Graduate program the following year with the intention of bringing the soft material experience I obtained as an undergraduate together with my nanomaterials experience from the Zettl group. I quickly found an intellectual connection with the Fréchet groups' approach to solving problems by manipulating the chemistry of materials to obtain responsive or functional structures. In my mind, this complimented the novel physical and electronic properties of the nanostructures I had synthesized and explored in the Zettl group. After joining the two groups, I endeavored to initiate a research program exploring how this might be possible. This necessarily interdisciplinary project was facilitated by the advice and guidance of two advisors with drastically different backgrounds and perspectives on functional materials. Only through discussion with them and with group members, experts in their particular fields, was the development of this new research program, and this body of work, possible.

I am extremely grateful for the guidance, expertise, and support that my two advisors, Professors Fréchet and Zettl, have given me. The clear view of the bigger picture and the vast knowledge of the specific that they supplied were integral to the conception and completion of this work and the development of me as a scientist. I owe all of my current and future success to them.

It would be impossible not to thank Dr. Stefan Pastine, whose creativity and sporadic intensity has kept me on my toes and pushed me to probe and understand the materials we were developing. His brilliance and scientific drive has taught me much about what science is and how to really understand it.

On the physics side, I have to thank Brian Kessler who has shown me (and explained to me) how to understand the physics of materials – and I still have not met anyone that can grasp concepts so deeply so quickly.

I would also like to thank the Solar to Work and the Photovoltaics sub-groups (both in the Zettl group and the Fréchet group) for their intellectual contribution to my projects. In addition, there are countless others who have helped me along the way.

Preface

This body of work encompasses the two major topics I explored as a Graduate Student at UC Berkeley working jointly between the Chemistry and Physics departments. This necessarily interdisciplinary work was a result of a strong collaboration and the diverse expertise of the two departments. The two topics explored are fundamentally linked by the utilization of new materials to absorb light and produce interesting responses. The first topic explores optothermally responsive composites: materials that efficiently convert light into heat to produce changes in their local environment. We were able to realize three major systems: light controlled surface wettability (Chapter 2); conversion of light into controlled motion (Chapter 3); and phototriggerable microcapsules to remotely control chemical reactions (Chapter 4). The second topic investigates the utilization of carbon nanotubes as the electron transporting component in organic photovoltaic devices (Chapter 6). These results suggest that the field of optically responsive materials has fundamentally new directions which require significant work to truly understand their implications.

Abstract

Optically Functional Nanomaterials:
Optothermally Responsive Composites and Carbon Nanotube Photovoltaics

David Christopher Okawa

Doctor of Philosophy in Chemistry

University of California, Berkeley

Professor Jean M. J. Fréchet, Co-chair

Professor Alex Zettl, Co-chair

The utilization of light to produce useful responses holds much potential for changing the world through smart materials and photovoltaic systems. We report the utilization of a variety of carbon nanotube composites as photovoltaic devices or as optothermal materials for the controlled placement of heat. Toward carbon nanotube – polymer photovoltaics we have successfully shown supramolecular compatibilization and functional bilayer devices. Opothermal processes are shown to manipulate a variety of system variables: surface energy, surface tension, and pressure. By manipulating these variables interesting responses are produced. Optothermal surface energy control produced wettability switches of 70º on composite surfaces. Optothermally modulated surface tensions of fluids converted light into work in the form of controlled linear motion, rotational motion, and volumetric expansion. Optothermally heated liquids confined within impermeable microcapsules resulted in the phototriggerable release of chemicals on demand. This release allowed small molecule reactions and polymerizations to be remotely initiated in a spatially selective manner. These results lay the framework for the expansion of the field of advanced optothermally responsive materials.

Part I:

Optothermally Responsive Materials

Chapter 1:

Introduction to Optothermally Responsive Materials

Responsive or 'smart' materials react to environmental stimuli with specifically designed changes in one or more properties. Responsive materials have two key components: a trigger or stimulus and the response itself. Responses can be mechanical, electrical, visual, chemical, structural, or functional. In recent years, this field has burgeoned and developed a variety of different triggers: light, heat, chemical environment, electrical potential[1] and mechanical force. Preeminent examples include: photochemical transformations such as photoacid generators;[2] thermally responsive polymers such as *poly*-N-isopropylacrylamide (*poly*-NIPAAm);[3] acid-degradable linkers for drug delivery vehicles;[4] piezoelectric materials that move in response to applied electric fields (or produce fields in response to physical deformation or motion);[5] and mechanically burstable microcapsules for self-healing polymers.[6]

For the development of new responsive systems, light is a particularly attractive trigger as it provides two levels of control: spatially via focusing and energetically via wavelength selection or frequency filtering. Prominent examples include photoresists used for lithography and caged reagents used to study biological processes. The field of light responsive materials is dominated by photochemical processes, such as bond isomerizations or cleavages. Azobenzene molecules (Figure 1-1) present a classic photochemical transformation: when exposed to ultraviolet light a trans-cis isomerization occurs; exposure to visible light results in relaxation back to the lower energy trans state. A classic example of photochemical bond cleavage is the UV activated photoacid generator, such as derivatives of triphenylsulfonium salts (Figure 1-2). Photoacid generators are an excellent example of why light responsive materials have had such a profound impact on the modern world. As used in photolithography, photoacid generators are mixed with polymers that bear acid-sensitive groups pendant to the polymer chain. When exposed to ultraviolet light the photoacid generator produces protons that catalyze the decomposition or deprotection of the acid-labile groups. The now deprotected polymer has drastically different solubility and can be easily removed via a liquid rinse or developer step. So called chemically amplified photoresists can realize features on the order of tens of nanometers and have been integral to the advancement of the semiconductor industry and truly changed the world in which we live.

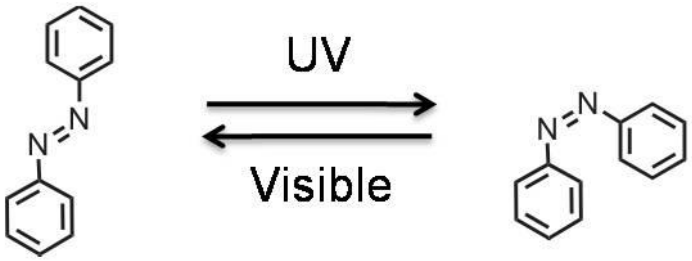

Figure 1-1. A classic example of a photoresponsive molecule, azobenzene. Ultraviolet light produces a trans-cis isomerization. Visible light provides relaxation back to the lower energy trans state.

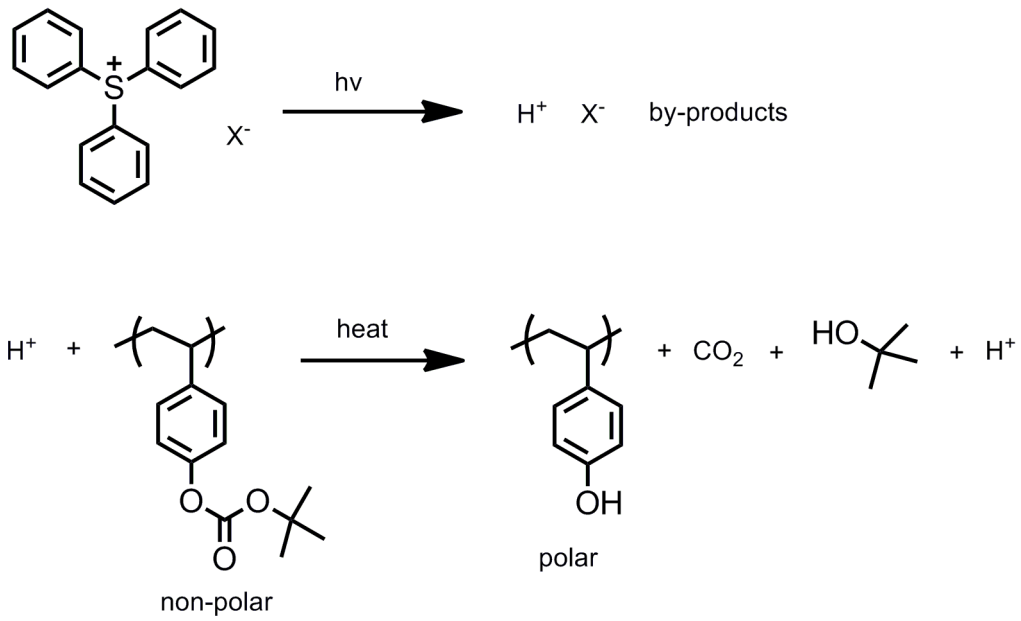

Figure 1-2. An influential phototriggered responsive material: chemically amplified photoresist. A photoacid generator absorbs ultraviolet light to produce a proton which then catalyzes the deprotection of the polymer and a solubility switch. The spatial selectivity of irradiation allows features to be resolved.

It is highly desirable to extend the use of light as a spatially resolved trigger to non-photochemical transformations. To understand how this might be done it is useful to briefly discuss what happens upon absorption of light. When light is absorbed by an organic molecule, the energy of the photon is transferred to the molecule and an electron is excited into a higher energy level. The excited molecule can react via a photochemical reaction or transformation (i.e. dissociation, cycloaddition, isomerization, *et cetera*), transfer the charge to another molecule, or relax back to the ground state. Relaxation to the ground state can proceed via a handful of mechanisms: directly with the emission of a photon (fluorescence), via the emission of a photon after intersystem crossing to a triplet state (phosphorescence), or collisionally via translational, rotational, and vibrational modes resulting in the production of heat (thermalization). The particular mechanism of relaxation is dependent on the specific molecule and the energy of photon that is absorbed as well as the physical and chemical environment of the system. Opto- or photo-thermalization, a process typically associated with waste and the undesirable loss of energy to the environment, is an underutilized energy conversion method that can be used to manipulate a variety of different variables.

Heat is a powerful parameter to manipulate because many system variables are temperature dependent (pressure, refractive index, physical phase, surface tension, entropy, reaction rates, *et cetera*). These parameters seem commonplace as bulk properties, but by using optothermal methods they can be remotely and spatially modulated, producing interesting phenomena. As a result, applications such as photothermal spectroscopy, photothermal therapy,[7] and laser welding have arisen. Photothermal spectroscopy[8] probes the changes in the refractive index or temperature as a result of optothermal heating and has been used to characterize a variety of surfaces and materials with a high degree of sensitivity.[9] Photothermal therapy is used to locally

cauterize tissues via the absorption of ingested dyes or absorbing nanomaterials.[10] Laser welding utilizes optothermal heating to locally enact a solid-liquid phase change to precisely weld two metals together. These three technologies use optothermal processes to manipulate refractive indices, cell viability, and phase transitions – leaving a variety of underexplored temperature dependent phenomena to be investigated. To thoroughly study optothermally responsive materials it is useful to discuss potential absorbers as well as some examples of system variables that are suitable for manipulation.

1.1 Optothermal Absorbers

An ideal optothermal absorber is one that absorbs all incident light and thermalizes the absorbed energy. As a result poorly fluorescing materials are advantageous. Dyes, pigments, carbon nanotubes (CNTs), and nanoparticles all have advantages and disadvantages as optothermal materials. Core-shell nanoparticles which appear to be attractive optothermal materials because of the absorptivity, high degree of tailorability, and potential for precisely defined absorption, have recently been reported to convert 40-60% of incident radiation into heat.[11] CNTs also appear promising as they have been reported to be the blackest known material, with a reflectivity below 0.1%,[12] and notably poor fluorescers, with quantum yields of ~3% for well isolated nanotubes and <0.05% for bundles of CNTs.[13] These factors weigh against their poor solubility and sample inhomogeneity. In our studies, we chose to focus on CNTs as their efficient absorption and poor fluorescence give a potential light to heat conversion approaching 100%, making them an ideal optothermal material. In addition, they have unique topological characteristics that make them advantageous as is discussed in Chapter 2.

1.2 Temperature Dependent System Variables

By intentionally focusing on the conversion of light to heat one can utilize the full energy of absorbed photons, as opposed to other processes where heat is invariably generated as an unintentional byproduct. We briefly discuss here, and in more detail in subsequent chapters, a few system variables that can be optothermally manipulated to produce interesting results.

1.2a Thermally Responsive Polymers

Poly-N-isopropylacrylamide (*poly*-NIPAAm) is one of many thermally responsive polymers that have a lower critical solution temperature (LCST). The LCST is the critical temperature below which a mixture is miscible in all proportions. Above this temperature, solubility decreases, in some cases drastically. This anti-intuitive phenomenon is a result of the combination of hydrogen bonding and non-polar regions along *poly*-NIPAAm chains. The inability of surrounding water molecules to hydrogen bond with the non-polar regions of the polymer forces them to orient themselves in a clathrate-like structure.[14] This substantial ordering results in a negative entropy of mixing with water. With a negative entropy value, as the temperature increases the entropy term dominates the enthalpic hydrogen bonding term. Above the critical temperature this results in a positive Gibbs free energy of solubilization and the

polymer collapses in on itself and phase separates. In the case of *poly*-NIPAAm, the solubility switch occurs very quickly at an environmentally relevant critical temperature of ~33 ºC.

Poly-NIPAAm has two well studied applications: thermally responsive surfaces and thermally responsive hydrogels. When attached to a surface, this effect has interesting implications for surface energy switches. Below the LCST, the surface is hydrophilic (~63º) and above the LCST the surface is hydrophobic (~93º). As discussed in chapter 2, this contact angle switch can be optothermally activated using an appropriately absorbing surface layer such as vertically aligned carbon nanotubes. When *poly*-NIPAAm is cross-linked, it forms a highly hydrated (99%) gel or hydrogel.[3] When heated above the LCST the water of hydration is expelled and the hydrogel collapses, losing about ~90% of its mass. This could potentially be coupled to optothermal absorbers, producing optically modulated solids with applications toward remotely operated valves.

1.2b Surface Tension

Another highly temperature dependent phenomenon is surface tension. Surface tension is the result of the attractive forces between molecules in a liquid or a solid. In the bulk, molecules are surrounded on all sides and thus feel no net force, but at the surface or an interface one side is composed of a different material. This asymmetry results in a net attractive force toward the bulk of the fluid, thus water droplets are spherical (discounting gravitational effects). When a suitably low density object is placed on top of liquid – surface tension supports the object, opposing the force of gravity, and pulling the object upwards (Figure 1-3). The relevant forces are described by the Young-Laplace equation as has been thoroughly discussed elsewhere.[15]

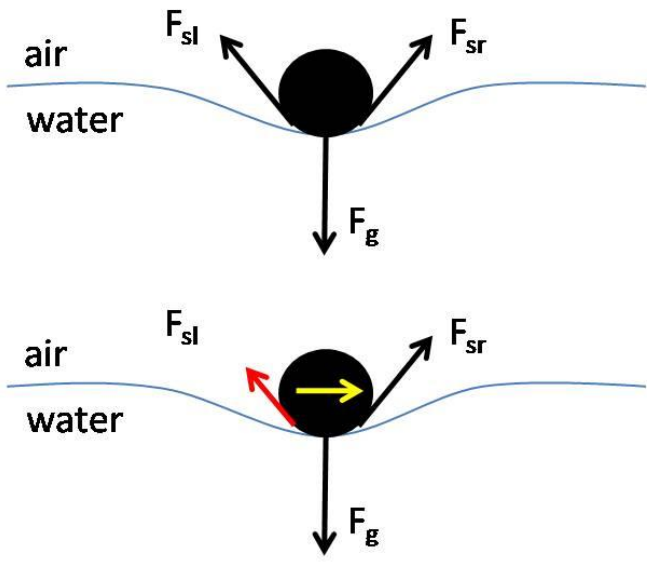

Figure 1-3. Schematic of the forces on a rod floating on the surface of a liquid. Surface tension forces, F_s, pull the object parallel to the contact line with the fluid. The gravitational force pulls the object down into the bulk of the liquid. If an asymmetry in the surface tension forces can be induced a net force is exerted on the object and it is pulled toward the higher surface tension.

For a floating object at rest, the surface tension forces and gravity are balanced (Figure 1-3 top). If one of the three forces is disturbed (Figure 1-3 bottom) an asymmetry arises and a net force acts upon the object resulting in motion. Such asymmetric surface tensions are used to describe the motion of soap boats and camphor chips on the surface of water. In the case of a soap boat, a small piece of soap is placed on the backside of a boat. Soap, which decreases the surface tension of water, dissolves, creating a soap concentration gradient and thus a surface tension gradient surrounding the boat. The boat, which lies within the chemical surface tension gradient, is subject to asymmetric surface tension forces (Figure 1-3 bottom) and as a result moves. This phenomenon has been studied under more precisely controlled conditions,[16] using ethanol as the surface tension manipulator.

Surface tension also depends on the temperature of the system, as described by Eötvös rule:[17]

$$\gamma = k\,(T_c - T)/V^{2/3} \qquad (1)$$

where γ is the surface tension, k is a constant, T_c is the critical temperature of the liquid, T is the temperature, and V is the molar volume of the substance. As T increases to T_c the surface tension decreases to zero. Thus, in an analogous fashion to chemically induced surface tension gradients, thermal gradients, in particular optothermal gradients can induce surface tension gradients and produce motion. In chapter 3 we discuss our investigation of optothermally modulated surface tension gradients for producing controlled motion of objects on fluids.

1.2c Phase Changes and Pressure

As the temperature of a liquid rises the vapor pressure over the liquid increases. In a confined system this increased vapor pressure translates to an increase in pressure. Thus, optothermal materials can produce pressure differentials. Such pressures could be used to modulate pistons for microfluidic diaphragm pumps or, if a suitable amount of pressure can be generated, bursting of the confined system. In chapter 4 we discuss optothermally burst systems for remotely initiated reaction chemistry.

1.2d Reaction Rate

The rate with which a reaction converts starting material to products, or the reaction rate, is dictated by numerous parameters: temperature, concentration, pressure (if gas phase), chemical environment, the presence of a catalyst, *et cetera*. Reaction rates are often empirically described by the Arrhenius equation:

$$k = Ae^{-E_a/RT} \qquad (2)$$

where k is the rate, A is the Arrhenius constant (experimentally determined), E_a is the activation energy, R is the gas constant, and T is the temperature. Consistent with the Arrhenius equation, when the temperature is increased the rate of reaction increases. Under standard laboratory

conditions, this translates to a typical rule of thumb that a reaction rate doubles with every 10 ºC increase in temperature.

The temperature dependence of the reaction rate presents an interesting opportunity for optothermal reaction rate modulation. Spatial modulation of reactions would allow for controlled product concentration gradients, the implications of which have not yet been realized. One system which could be strongly influenced by such work is the platinum catalyzed decomposition of hydrogen peroxide used to produce locomotion of small objects.[18] In these systems the decomposition of hydrogen peroxide produces locomotion either through the evolution of gas bubbles or via an electroosmotic flow[18] created by flowing charge within the nanostructure. Optothermal reaction rate control could act as an accelerator for the motion of these objects or with suitable engineering, spatially controlling illumination could be used to directionally control motion.

1.3 Moving Forward

Currently, the field of optothermally responsive materials is dominated by ablative technologies (photothermal therapy and laser welding) and photothermal spectroscopy. The ability to combine highly efficient optothermal materials and their manipulation of a variety of system variables opens up a wide range of other applications. This extension significantly expands the scope of light responsive materials. We discuss our investigation of three optothermally responsive systems: optothermally modulated surface energies using thermally responsive polymers; optothermally controlled motion of objects on fluids; and optothermally triggered release of chemicals for "on demand" chemistry. We also briefly touch on continuing and future research directions that are particularly promising and important.

---

1 Chang, S. T.; Paunov, V. N.; Petsev, D. N.; Velev, O. D. *Nat. Mater*. **2007,** *6*, 235-240.

2 Fréchet, J. M. J. *Pure & Appl. Chem.* **1992,** *64*, 1239-1248. Shirai, M.; Tsunooka, M. *Bull. Chem. Soc. Jpn.* **1998,** *71*, 2483-2507.

3 Schild, H. G. *Prog. Polym. Sci.* **1992,** *17*, 163-249.

4 Gillies, E.R.; Goodwin, A.P.; Fréchet, J.M.J. *Bioconj. Chem.* **2004,** *15*, 1254-63.

5 Anton, S. R.; Sodano, H. A. *Smart Mater. & Struct.* **2007,** *16*, R1-R21. Alder, J. F.; Mccallum, J. J. *Analyst* **1983,** *108*, 1169-1189.

6 White, S. R.; Sottos, N. R.; Moore, J.; Geubelle, P.; Kessler, M.; Brown, E.; Suresh, S.; Viswanathan, S. *Nature* **2001,** *409*, 794-797.

7 Torti, S. V.; Byrne, F.; Whelan, O.; Levi, N.; Ucer, B.; Schmid, M.; Torti, F.; Akman, S.; Liu, J.; Ajayan, P. M.; Nalamasu, O.; Carroll, D. *Int. J. NanoMed.* **2007,** *2*, 707-714. Levi-Polyachenko, N. H.; Merkel, E. J.; Jones, B. T.; Carroll, D. L.; Stewart IV, J. H. Mol. Pharm. **2009,** *6*, 1092-1099.

8 *Photothermal Spectroscopy Methods for Chemical Analysis;* Bailkowski, S. E., Winefordner, J. D. Eds.; Chemical Analysis: A Series of Monographs on Analytical Chemistry and Its Applications Vol 134; John Wiley & Sons, Inc.: New York, 1996.

9 Berciaud, S.; Cognet, L.; Poulin, P.; Weisman, R. B.; Lounis, B. *Nano Lett.* **2007,** *7*, 1203-1207. Skumanich, A.; Fournier, D.; Boccara, A. C.; Amer, N. M. 4th International Topical Meeting on Photoacoustic, Thermal and Related Sciences, Quebec, Canada, August 4, 1985.

10 Torti, S. V.; Byrne, F.; Whelan, O.; Levi, N.; Ucer, B.; Schmid, M.; Torti, F.; Akman, S.; Liu, J.; Ajayan, P. M.; Nalamasu, O.; Carroll, D. *Int. J. NanoMed.* **2007,** *2*, 707-714. Levi-Polyachenko, N. H.; Merkel, E. J.; Jones, B. T.; Carroll, D. L.; Stewart IV, J. H. Mol. Pharm. **2009,** *6*, 1092-1099. Chen, W. R.; Adams, R. L.; Bartels, K. E.; Nordquist, R. E. *Cancer Lett.* **1995,** *94*, 125-131. Hirsch, L. R.; Stafford, R. J.; Bankson, J. A.; Sershen, S.R.; Rivera, B.; Price, R. E.; Hazle, J. D.; Halas, N. J.; West, J. L. *Proc. Natl. Acad. Sci.* **2003,** *11*, 13549-13554.

11 Cole, J. R.; Mirin, N. A.; Knight, M. W.; Goodrich, G. P.; Halas, N. J. *J. Phys. Chem. C* **2009,** *113*, 12090-12094.

12 Yang, Z. P.; Ci, L.; Bur, J. A.; Lin, S. Y.; Ajayan, P. M. *Nano Lett.* **2008,** *8*, 446-451. Mizuno, K.; Ishii, J.; Kishida, H.; Hayamizu, Y.; Yasuda, S.; Futaba, D. N.; Yumura, M.; Hata, K. *Proc. Nat. Acad. Sci.* **2009,** *106*, 6044-6047.

13 Carlson, L. J.; Maccagnano, S. E.; Zheng, M.; Silcox, J.; Krauss, T. D. *Nano Lett.* **2007,** *7*, 3698-3703. O'Connell, M. J.; Bachilo, S. M.; Huffman, C. B.; Moore, V. C.; Strano, M. S.; Haroz, E. H.; Rialon, K. L.; Boul, P. J.; Noon, W. H.; Kitrell, C.; Ma, J.; Hauge, R. H.; Weisman, R. B.; Smalley, R. E. *Science* **2002,** *297*, 593-596.

14 For a thorough review of *poly*-NIPAAm refer to Schild, H. G. *Prog. Polym. Sci.* **1992,** *17*, 163-249 and the references therein.

15 De Gennes, P. G.; Brochard-Wyart, F.; Quere, D.; *Capillary and Wetting Phenomena – Drops, Bubbles, Pearls, Waves;* Springer: New York, 2004.

16 Su, M. *Appl. Phys. Lett.* **2007,** *90*, 144102.

17 Adam, N. K. *The Physics and Chemistry of Surfaces, 3rd ed.;* Oxford University Press: London, 1941.

18 Laocharoensuk, R.; Burdick, J.; Wang, J. *ACS Nano* **2008,** *2,* 1069-1075. Sundararajan, S.; Lammert, P. E.; Zudans, A. W.; Crespi, V. H.; Sen, A. *Nano Lett.* **2008,** *8*, 1271-1276. Burdick, J.; Laocharoensuk, R.; Wheat, P. M.; Posner, J. D.; Wang, J. *J. Am. Chem. Soc.* **2008,** *130*, 8164-8165. Demiork, U. K.; Laocharoensuk, R.; Manesh, K. M.; Wang, J. *Angew. Chem.* **2008,** *120*, 9489-9491. Wang, Y.; Hernandez, R. M.; Bartlett, D. J.; Bingham, J. M.; Kline, T. R.; Sen, A.; Mallouk, T. E. *Langmuir* **2006,** *22*, 10451-10456. Paxton, W. F.; Sen, A.; Mallouk, T. E. *Chem. Eur. J.* **2005**, *11*, 6462-6470. Ismagilov, R. F.; Schwartz, A.; Bowden, N.; Whitesides, G. M. *Angew. Chem. Int. Ed.* **2002,** *41*, 652-654.

Chapter 2:

Carbon Nanotube Surface Functionalization and Optothermal Surface Energy Modulation

The ability to remotely access and spatially control temperature through optothermal processes has interesting implications for thermally responsive surfaces. A prominent example of a thermally responsive surface is a substrate grafted with *poly-N*-isopropylacrylamide (*poly*-NIPAAm). *Poly*-NIPAAm is a widely studied thermoresponsive polymer with a lower critical solution temperature (LCST) of ~33 ºC.[1] When grafted from a smooth surface, *poly*-NIPAAm displays a wetting switch above and below the LCST, with a contact angle (CA) of 93º and 63º, respectively.[2] By coupling a thermally responsive polymer to an optothermal surface one gains the ability to remotely and spatially selectively dictate the wettability of the substrate. This enhanced control over a surface has a variety of applications from lab-on-chip devices to self-cleaning surfaces. In particular, we became interested in developing surfaces capable of producing a drastic surface energy or contact angle switch (i.e. a hydrophilic surface becoming superhydrophobic) in response to irradiation with a laser or focused sunlight.

To produce drastic wettability switches, it was important to first understand how superhydrophobic and superhydrophilic surfaces can be obtained. A common inspiration for such extreme surfaces is the natural world. So called "bio-inspired" materials chemistry, is a recent field that looks at natural systems to identify patterns, principles, and concepts that can serve as starting points for the development of advanced materials. In nature, a specific function is often provided by a unique combination of surface roughness and chemical composition. Preeminent examples include the Lotus leaf, the Water Strider leg, and the Gecko foot. All of these examples combine nano- and/or micro rough surfaces (Figure 2-1) with waxy coatings to produce superhydrophobic surfaces capable of extra-ordinary feats. Recently, both extremes, superhydrophobicity (contact angle (CA) > 150º; sliding angle < 5º) and superhydrophilicity (CA near 0º) have aroused significant attention for practical applications such as self-cleaning windows and stain resistant textiles.[3]

In the laboratory two dominant, though contested,[4] models exist to explain wetting behavior of rough surfaces: Cassie-Baxter[5] and Wenzel.[6] The Wenzel model assumes a homogeneously functionalized surface modified by a roughness factor and typically describes wetted surfaces with lower contact angles (Figure 2-1 bottom left). The roughness factor is used to describe the increased contact area as a result of the roughness of the surface and is essentially a thermodynamic argument. The Cassie-Baxter model takes into account heterogeneous functionality as well as roughness. This allows it to describe circumstances where droplets are supported by "pillars" on the surface (Figure 2-1 bottom right). In this case, the plane of the "surface" that the droplet is in contact with is composed of both the tops of the pillars and air. Air, which minimally interacts with water, increases the effective hydrophobicity of the surface and, depending on the composition of the pillars, pushes the contact angle into the superhydrophobic regime. Surfaces can transition between the Cassie and Wenzel states[7] depending on the conditions, though typically the quality of a superhydrophobic surface is dictated by how difficult it is to make this transition. Keeping this in mind, to design a surface that has a drastic optothermally modulated wettability switch, the surface must have roughness on the appropriate scale and be able to transition between the Cassie-Baxter regime (superhydrophobic) to the Wenzel regime (hydrophilic or superhydrophilic).

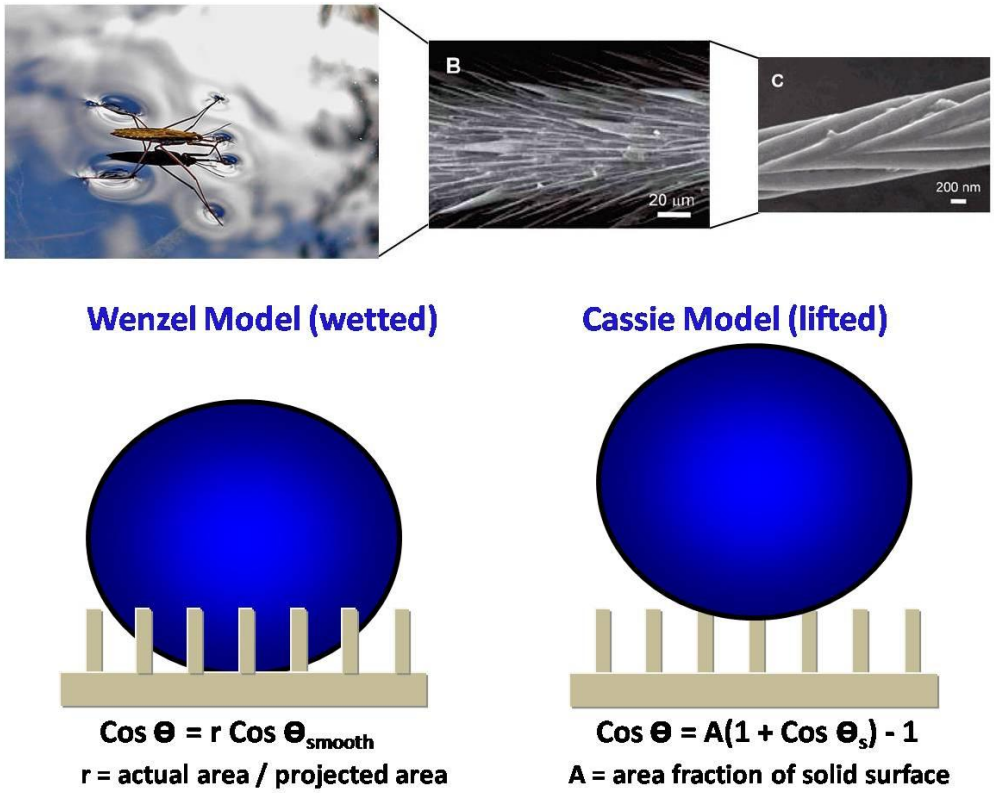

Figure 2-1. A water-strider (top) with scanning electron micrographs depicting the micro and nanoscale roughness of the superhydrophobic legs.[8] Illustrations (bottom) depicting the Cassie-Baxter and Wenzel models. The Wenzel model, which is often used to understand superhydrophilic surfaces, describes the case of a wetted rough surface. The Cassie-Baxter model, which is often used to understand superhydrophobic surfaces, describes a surface with a droplet supported by the rough pillars and air.

Vertically aligned nanotube surfaces (VANTs) provide an ideal optothermal coating material for accessing both the superhydrophilic and superhydrophobic regimes as they can be produced with both nano- and microscale roughness and have the potential for functionalization to optimize these effects.[9] VANTs have excellent optothermal properties as they are broad-band absorbers[10] and typically fluoresce poorly.[11] The combination of efficient optothermal conversion and inherent topology makes VANTs ideal candidates for optothermal contact angle modulation.

The chemical vapor deposition (CVD) of VANTs arrays provides a direct means to confer microscale structure with inherent nanoscale roughness to a surface (Figure 2-2). Hierarchal roughness and the possibility for chemical functionalization make VANTs attractive scaffolds for the fabrication of new materials. However, in order to realize the potential of this biomimetic approach, two issues need to be addressed: (1) the durability of VANTs is typically low; and (2) a facile method for chemical patterning of VANTs is lacking. Herein we describe a simple scheme for functionalizing robust patterned VANTs. We were able to solve both of these issues (*vide infra*), which lead to the development of the first UV-patterning method for the preparation of patterned, stable superhydrophobic/superhydrophilic surfaces. Furthermore, these results

allowed the coupling of chemical modification to the optothermal properties of CNTs for the production of optothermally responsive surfaces with drastic contact angle switches.

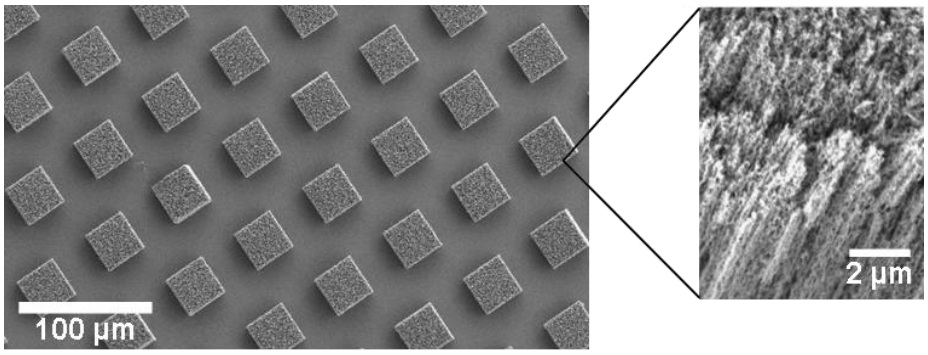

Figure 2-2. Patterned arrays of CNT forests provide both micro- and nanoscale structure to a substrate.

2.1 Carbon Nanotube Surfaces

The structural integrity of VANTs prepared via standard CVD techniques has been limited by weak adhesion of the film to the substrate and the propensity for film deformation upon solvent exposure due to strong van der Waals forces between CNTs (Figure 2-3).[12] Increasing the structural integrity (or robustness) of VANTs was paramount for them to be suitable for surface coating applications. We were able to address this issue by developing a modified CVD technique for the synthesis of multi-walled carbon nanotube (MWCNT) forests. To increase forest adhesion to the substrate, 10 nm thick iron catalyst films and a high ethylene concentration were used during growth. Specifically, silicon substrates were prepared for growth by e-beam evaporation of 10 nm of Alumina followed by deposition of a 1 to 10 nm layer of Iron. The substrates were then inserted into a 1-inch quartz reaction tube and placed in a Lindberg/Blue M Mini Mite Tube Furnace and heated to 750 ºC under Nitrogen (99.9997 %) flow (200 sccm). At the reaction temperature, the gas was changed to 200 sccm ethylene (99.5 %) and held at 750 ºC for 1-20 minutes. The furnace was then cooled to room temperature and the nanotube forests were evaluated by Raman spectroscopy, SEM, and TEM. Importantly, the as-grown forests (Figure 2-4 and Figure 2-5) were resistant to deformation by strong solvent streams and mild mechanical pressure/scratching.

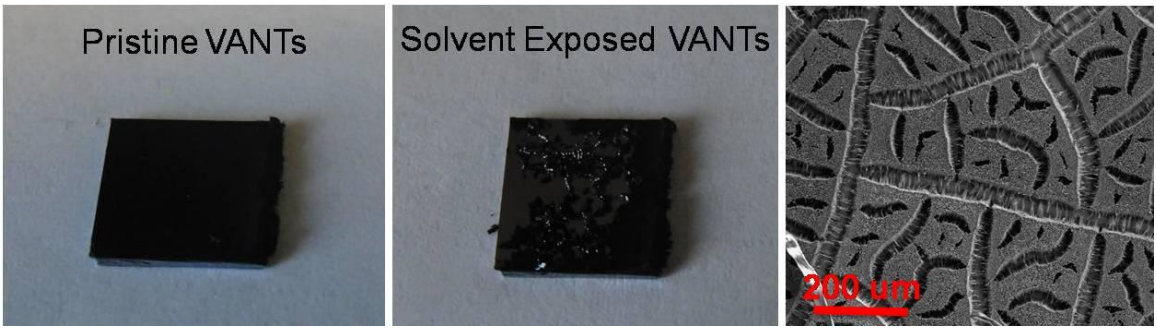

Figure 2-3. VANTs before (left) and after (middle) exposure to ethanol. Solvent exposure results in strong van der waals forces disturbing the surface to the extent of even pulling the nanotubes away from the substrate. SEM image (right) of a VANT substrate after solvent exposure; a drastic reorganization of the surface is evident.

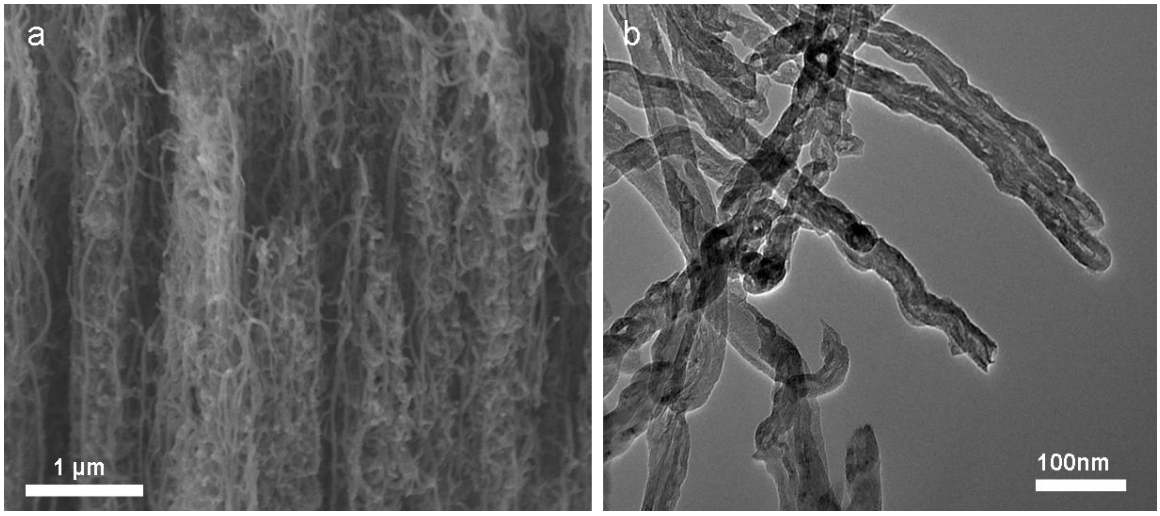

Figure 2-4. Micrograph images of non-robust VANTs grown on a 10 nm thin film of Fe on 10 nm of Al_2O_3 on a Si wafer. (a) SEM. (b) TEM of non-robust MWNT.

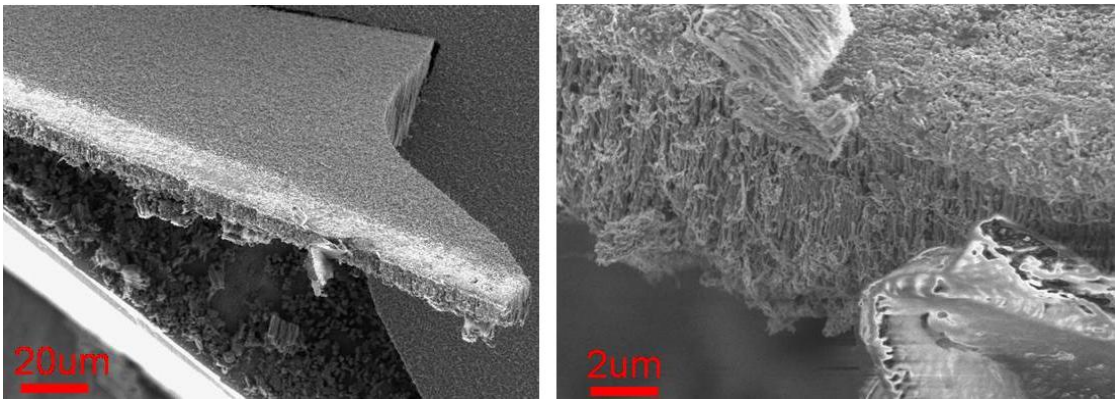

Figure 2-5. SEM of *robust* carbon nanotube forests. Forest has been physically broken off of the silicon wafer (left). Magnified image of forest (right).

To determine the mechanism by which the growth conditions produce robust VANTs we investigated the growth time parameter space. The growth time study found minimal height dependence but considerable diameter dependence (characteristic scanning electron micrographs are shown in Figure 2-6). We hypothesized that the enhanced robustness is the result of the gas phase decomposition of ethylene at the reaction temperature, resulting in the deposition of amorphous carbon on the CNT surface. At high ethylene concentrations, the catalyst is quickly saturated and poisoned, limiting forest heights to 5-50 µm. After the catalyst is inactivated, ethylene that is decomposed in the gas phase continuously deposits amorphous carbon on to the substrates, coating the VANTs and effectively cementing them in place. The deposition of amorphous or highly defective carbonaceous material is supported by Raman spectroscopy. The Raman spectrum of forest prepared via this modified CVD method revealed the presence of sp^3 and sp^2 carbon in a semi-quantitative fashion through characteristic peaks (D peak ~1320 cm^{-1}

for sp^3 bonded carbon and G peak ~1600 cm^{-1} for crystalline sp^2 bonded nanotubes). An assessment of the presence of amorphous carbon was made by comparing the ratio of the areas of the D to G peaks. At longer reaction times, an increase in the D to G ratio was observed (Figure 2-6 bottom), indicating a time dependent deposition of amorphous carbon. Qualitatively, we found that increased reaction time results in increased resistance to deformation by solvents and mechanical forces: ranging from low resistance (1 minute or less) to high resistance (greater than 10 minutes). We found that a growth time of 10 minutes with 10 nm of iron catalyst produced substantially robust forests that were suitable for functionalization experiments. We were also able to take pristine VANTs grown under standard chemical vapor deposition conditions[13] and expose them to high ethylene concentrations at 750 ºC and drastically increase their resistance to chemical and mechanical stress. This result supports our hypothesis that the deposition of amorphous carbon has a "cementing effect" and, importantly, allowed taller VANTs to be made robust after growth.

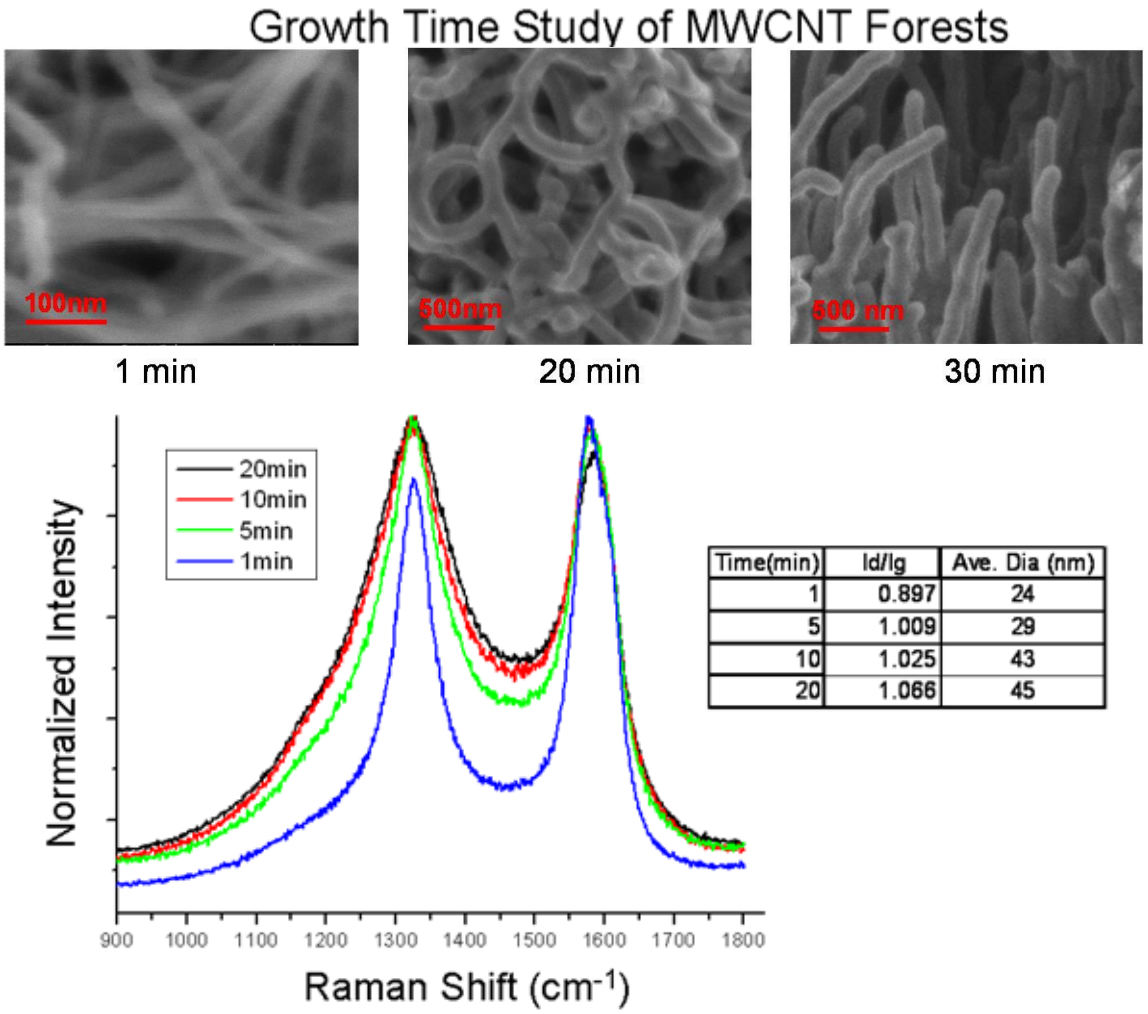

Figure 2-6. VANT growth time study. Scanning electron micrographs showing increasing diameter with reaction time (top). Raman spectra of VANTs grown on 10 nm Fe catalyst on 10 nm of Alumina on a Si substrate (bottom) normalized to the G peak at 1580 cm^{-1}. The D peak at ~1300 cm^{-1} grows taller and wider with increased growth time. Inset table shows the increase in I_d/I_g Peak height ratio and average diameter by SEM as a function of reaction time.

2.2 Chemical Functionalization

To develop a chemical patterning method, we investigated nitrene insertion into CNTs. Nitrenes have been used for the covalent modification of single-wall CNTs (SWCNTs) and MWCNTs.[14,15] Generation of nitrenes by photolytic decomposition of azides provided an opportunity for modifying forests in a spatially controlled manner. With this in mind, generic perfluoroarylazide **1** was selected as a scaffold for displaying molecular information on the surface of CNTs (Figure 2-7). The perfluoroarylazide moiety was selected as the nitrene precursor because of its high intermolecular insertion efficiency relative to other aryl- or alkyl azides.[16] Furthermore, the specific azide chosen has a carboxyl group through which a variety of functionality can be attached via standard coupling reactions. It was envisioned that the R-group in **1** could be used to tailor the surface properties, and that patterning could be achieved via exposure through a photomask.

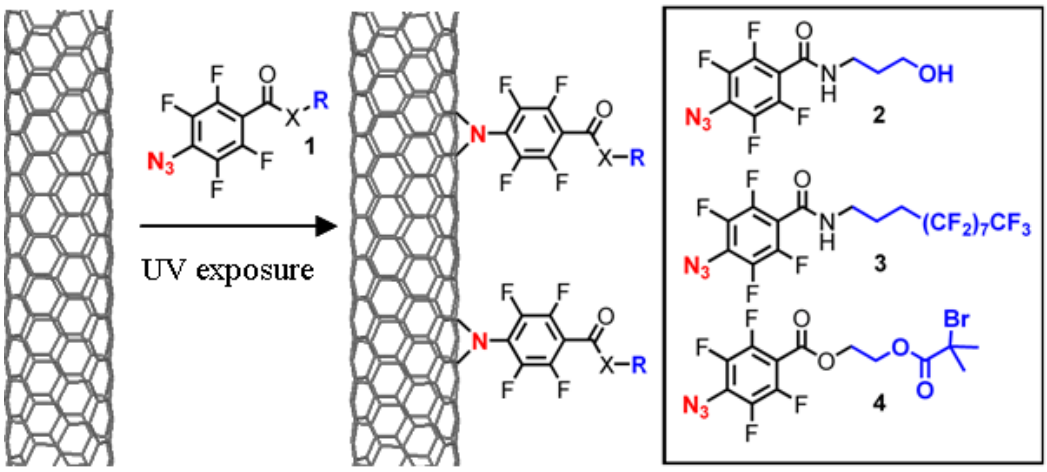

Figure 2-7. Functionalization scheme using perfluoroazides employed to modify CNT forests. Several functional handles were appended to show the versatility of the scheme.

To test if the azide side chain can modify surface properties, model compounds **2** and **3** were prepared. The hydroxyl-containing **2**, and the fluoroalkyl-containing **3** were designed to control the surface energy of the VANTs. As mentioned above, the wetting behavior of a surface is dictated by a combination of surface roughness and chemical composition. Both superhydrophobic surfaces (contact angle (CA) > 150º; sliding angle < 5º) and superhydrophilic surfaces (CA near 0°) have recently been the focus of considerable attention.[17,18] Due to the nanoscale roughness of the VANT template, attachment of **2** was expected to confer superhydrophilic properties to the substrate, while **3** was expected to confer superhydrophobic properties. As a basic procedure, substrates were dipped in a solution of azide in acetone (10 mg/mL), allowed to dry, exposed to UV radiation (λ = 254 nm) for 5 minutes, and then rinsed by an acetone stream. VANTs treated with **2** exhibited "sponge-like" behavior after UV exposure (Figure 2-8) with a water contact angle diminishing to nearly 0º after a few seconds. In stark contrast, forests treated with **3** (Figure 2-8) exhibited superhydrophobic behavior; water droplets were nearly spherical and unstable on the surface due to the small hysteresis between the advancing and receding CAs (Θ_A/Θ_R = 162º/161º).[19]

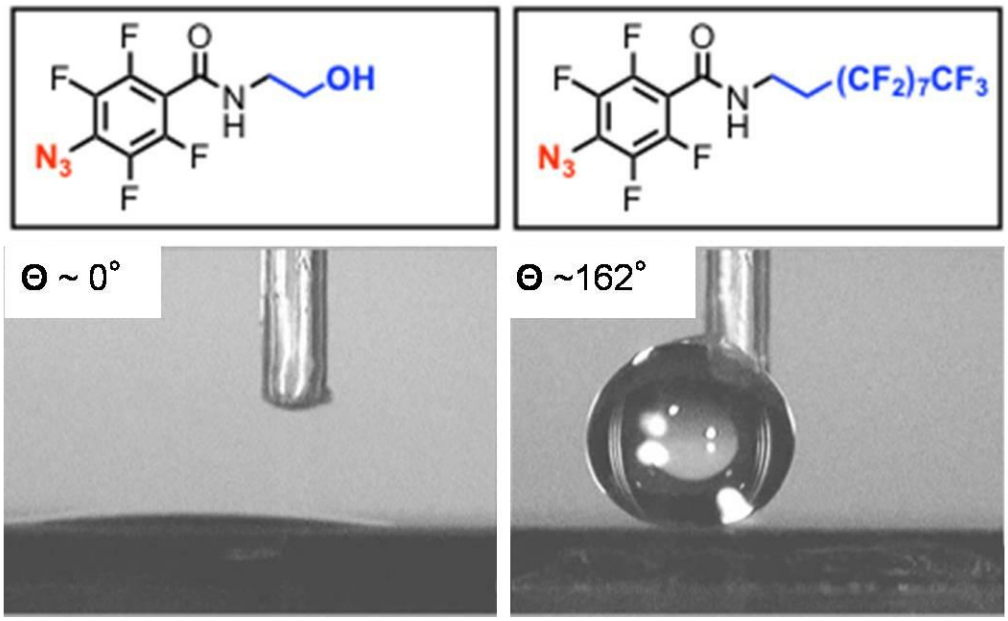

Figure 2-8. Observation of contact angle after functionalization with hydrophilic azide 2 (left) and hydrophobic azide 4 (right). Superhydrophilicity and superhydrophobicity are apparent.

The exact site of functionalization had to be clarified because of the presence of amorphous carbon on the VANT substrates. To ensure that the CNTs themselves can be functionalized under our treatment conditions, we prepared Bucky paper out of highly crystalline single wall carbon nanotubes (SWNTs). Bucky paper was produced by dispersing HiPCO® SWNTs (obtained from CNI, Houston, Texas) via sonication in an aqueous solution of sodium dodecyl sulfate solution (1 mg of nanotubes in 100 mL of 1 wt. % SDS solution). The suspended solution (5mL) was passed through an 800 nm mixed cellulose ester membrane (Metricel® membrane filter) and rinsed with copious amounts of DI water. The Bucky paper was then floated off of the membrane in acetone and rinsed with acetone before depositing on a glass or Teflon slide. The obtained Bucky paper was then treated with hydrophobic azide **3** via the standard UV-modification procedure. Raman and contact angle characterization were then performed on the untreated and treated Bucky paper.

The static CA of the paper increased from 68º to 110º after treatment with **3** (Figure 2-9). Further evidence for covalent attachment was provided by Raman spectroscopy (Figure 2-10). After modification, an increase in the D band intensity (I_D) occurred with a concomitant decrease in the G band intensity (I_G) (Figure 2-10 inset). The observed increase in the I_D/I_G ratio is indicative of the production of defect sites in the nanotube lattice. A second treatment with **3** resulted in a further increase in the I_D/I_G ratio indicating that additional modification of the substrate occurred.

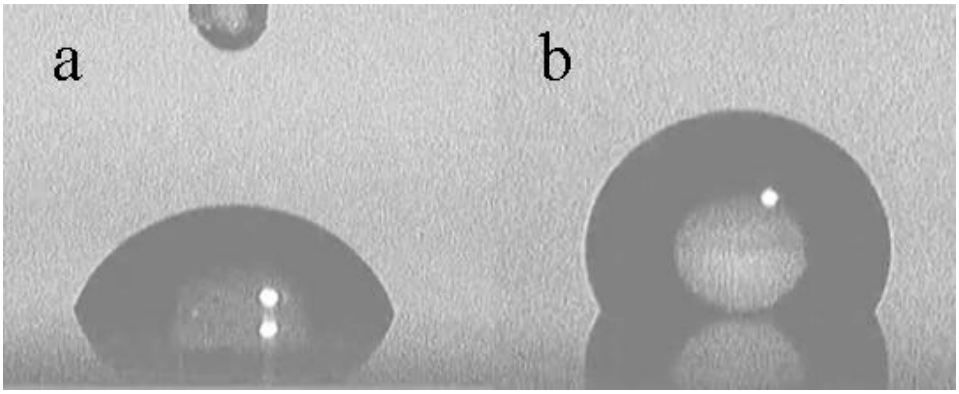

Figure 2-9. Optical images of sessile microliter water droplets on bucky paper. (a) Unmodified. (b) Modified with **3**.

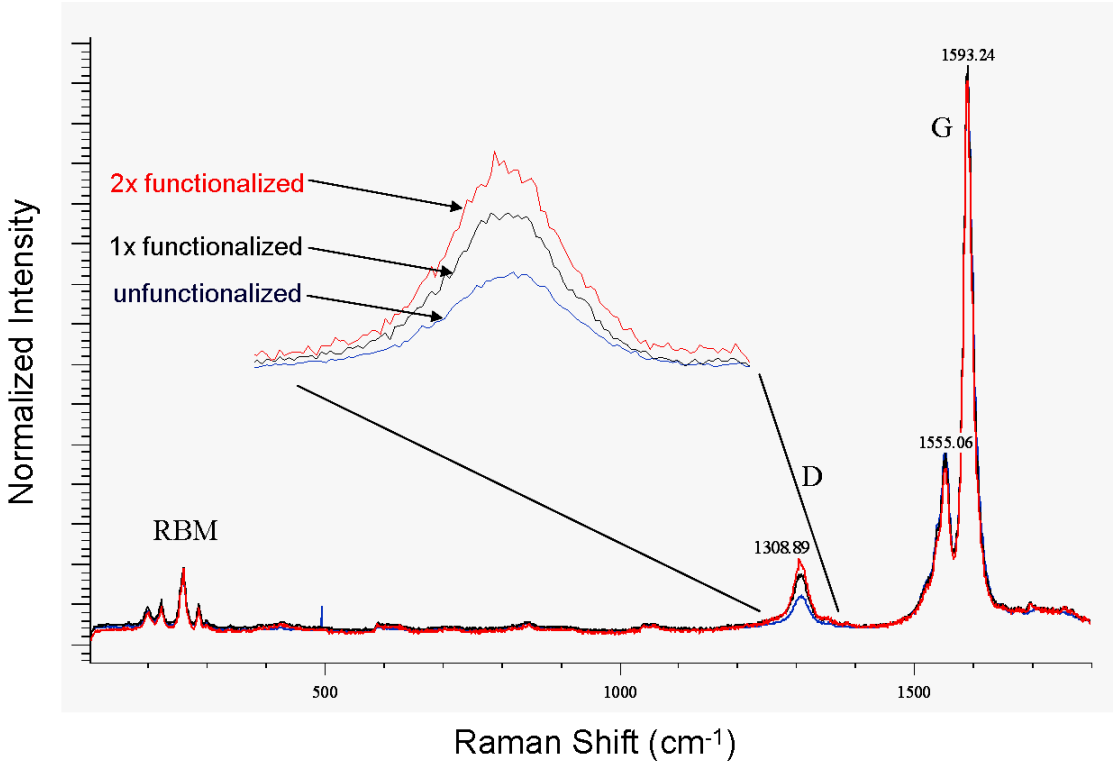

Figure 2-10. Raman study of the functionalization of HiPCO® SWNT Bucky paper at 633 nm excitation. The light blue spectrum is unfunctionalized bucky paper. The inset shows the growth of the D peak at 1309 cm^{-1} with subsequent treatment with azide **3**.

The ability to increase the extent of functionalization by a second and third treatment suggested that multiple azides could be used to further tailor or alter the surface properties of VANT substrates. This was demonstrated by a simple switching of the surface energy of a forest template. As shown in Figure 2-11, superhydrophilic samples produced after modification with **2** became superhydrophobic after a subsequent treatment with **3**. This overriding of hydrophilicity

may be attributed to the significantly longer length of the fluoroalkyl chain in **3,** relative to hydroxyl chain in **2**.

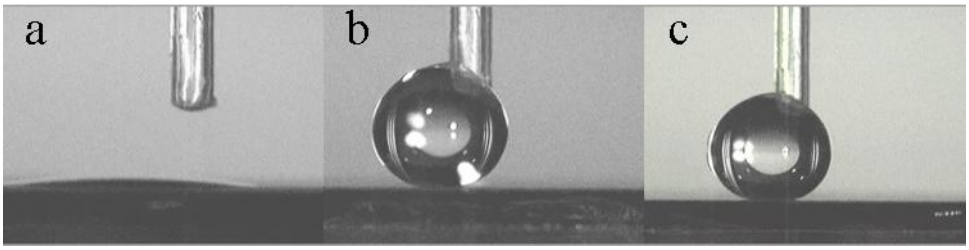

Figure 2-11. Optical images of microliter water droplets on VANT substrates. (a) Modified with **2**. (b) Modified with **3**. (c) Modified with **2** and subsequently modified with **3**.

2.3 Patterned Functionalization

Considerable attention has been paid to developing surfaces with differential wettability;[20] however, only a few examples of stable patterned superhydrophilic-superhydrophobic surfaces have been reported.[21] The ability of **3** to override **2** allowed the fabrication of superhydrophobic substrates with hydrophilic regions in two simple steps: (i) blanket modification with **2**; and (ii) treatment with **3** followed by irradiation through an appropriate photomask. Figure 2-12a shows the wetting characteristics of a prepared macro channel. Water was effectively confined to the hydrophilic region of the substrate by the superhydrophobic background. Droplets that landed on the superhydrophobic region either rolled off the substrate or into the hydrophilic channel. The macro-patterned films remained stable for at least one month. A micro-patterned substrate was also prepared using a quartz mask with 80 μm squares. A micro droplet array was produced from selective condensation of water vapor in the hydrophilic regions of the surface (Figure 2-12b). This specialized surface effectively serves as a synthetic mimic to the back of the Stenocara beetle of the Namib Desert.[22] To the best of our knowledge, this was the first demonstration of a stable superhydrophobic surface with hydrophilic features of less than 100 microns.

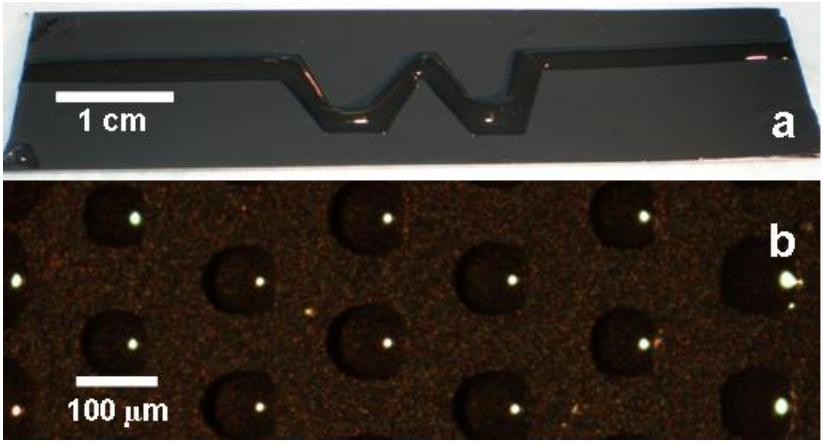

Figure 2-12. Superhydrophilic patterns on superhydrophobic backgrounds: (a) a macroscopic superhydrophilic channel; (b) dark field image of selective condensation on micro-patterned hydrophilic regions.

2.4 Attachment of Azide Polymer Initiator and Polymerization

Having demonstrated that azides **2** and **3** can transform the properties of VANTs, we next turned our attention to azide **4**. The 2-bromoisobutyrate moiety in **4** serves as an initiator for atom transfer radical polymerization (ATRP)[23] and enables the grafting of a variety of polymers (as performed by Stefan Pastine). UV triggered attachment of **4** followed by polymerization of NIPAAm under ATRP conditions resulted in modification of the forest surface with *poly*-NIPAAm.[24] Specifically, the reagent ratio of NIPAAm/CuBr/PMDETA/H_2O/Methanol used for polymerization was 2.2 mmol/0.05 mmol/0.05 mmol/1 mL/0.1 mL. The basic procedure consisted of a forest substrate modified with **4** being placed in 20 mL vials with a pierceable Teflon screw cap. The vials were evacuated and refilled with nitrogen (three times). NIPAAm, H_2O, and methanol were then placed in a Schlenk Flask and degassed via three freeze-pump-thaw cycles. In a separate, Schlenk Flask was placed CuBr and a magnetic stirring bar. The flask was evacuated and refilled with nitrogen (two times), and then PMDETA was added via syringe, and then the flask was evacuated and refilled with nitrogen (two times). The degassed NIPAAm solution was cannula transferred to the copper containing flask. After vigorous stirring for five minutes (not all of the copper dissolves), the polymerization mixture was cannula transferred to the substrate containing vials. After the appropriate reaction time, substrates were washed with copious amounts of water and acetone. Fourier transform infrared spectroscopy (FTIR) confirmed the presence of *poly*-NIPAAm on the substrate, Figure 2-13b.

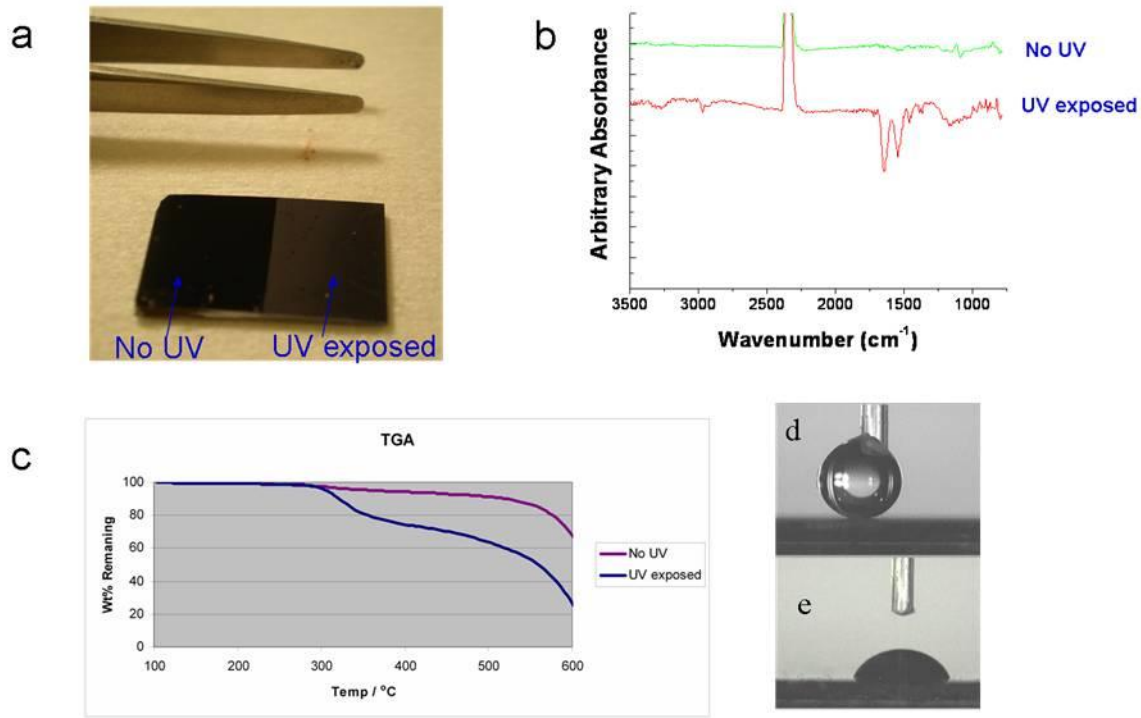

Figure 2-13. Evidence for selective modification of VANT substrate with *poly*-NIPAAm and contact angle images. (a) Image of the substrate. (b) FTIR spectrum of the masked and unmasked regions after polymerization. (c) TGA comparison between the masked and unmasked regions after polymerization. (d,e) Optical images of microliter water droplets on functionalized nanotube forest substrates. (d) Modified with polymer imitator 4. (e) After polymerization.

To determine if modification was a result of grafting from the nanotube surface, a forest was coated in **4** and half of the substrate was masked during UV exposure. The entire substrate was subjected to the standard ATRP conditions for four hours. Significant differences existed between the masked and unmasked region of the substrate in qualitative visual analysis, TGA analysis,[25] and FTIR analysis (Figure 2-13). Substrates modified with polymer initiator **4** were superhydrophobic (Θ_A/Θ_R = 167º/163º) and became hydrophilic after polymerization (Θ_{static} = 64º; Θ_A/Θ_R = 99º/4º). No distinctive signals were observed in the FTIR spectrum of the masked region. Furthermore, no polymer decomposition was observed by thermogravimetric analysis (Figure 2-13). These results indicated that a surface initiated polymerization was enabled by the photo-triggered attachment of azide-initiator **4**. Using appropriate photomasks we prepared substrates with isolated polymerized features as small as 5 μm, as well as a polymerized background with isolated pristine regions as small as 60 μm (Figure 2-14).

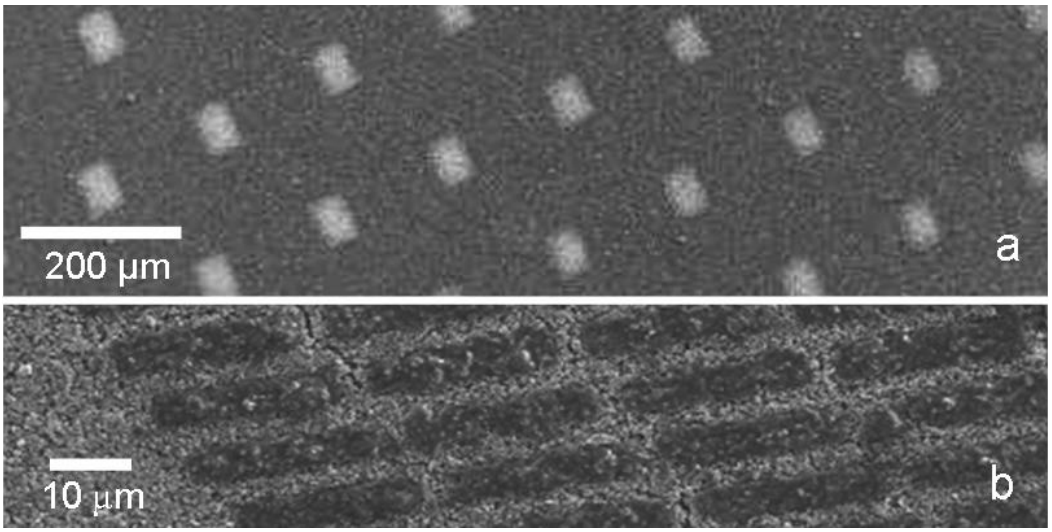

Figure 2-14. Scanning electron micrographs of *poly*-NIPAAm patterned on VANTs via polymerization initiator azide **4**. Dark areas represent polymer region. (a) Polymerized background with isolated unmodified regions. (b) Unmodified background with patterned regions of polymer.

2.5 Optothermal Surface Energy Control

As mentioned above, *poly*-NIPAAm is a widely studied thermoresponsive polymer with a lower critical solution temperature (LCST) of 37 ºC. When grafted from a smooth surface, *poly*-NIPAAm displays a wetting switch above and below the LCST, with a CA of 93º and 63º above and below 37 ºC. This difference has been magnified by grafting *poly*-NIPAAm from rough substrates.[26] The development of the nitrene-based UV patterning method set the stage for exploring the coupling of the optothermal properties of VANTs to the thermoresponsive properties of *poly*-NIPAAm to produce substrates whose wetting properties respond to light. As depicted in Figure 2-15, the nanotubes act as optothermal heaters to switch the *poly*-NIPAAm coating between hydrophilic and hydrophobic states. To test this, we observed the temperature dependence of the contact angle of *poly*-NIPAAm functionalized forests using a temperature and humidity control chamber (Figure 2-16). *Poly*-NIPAAm functionalized forests showed a contact

angle switch from 138º at 40 ºC to 100º at 25 ºC. Though the specific angles varied depending on a number of parameters, the relatively modest temperature dependence (~40º) was constant.

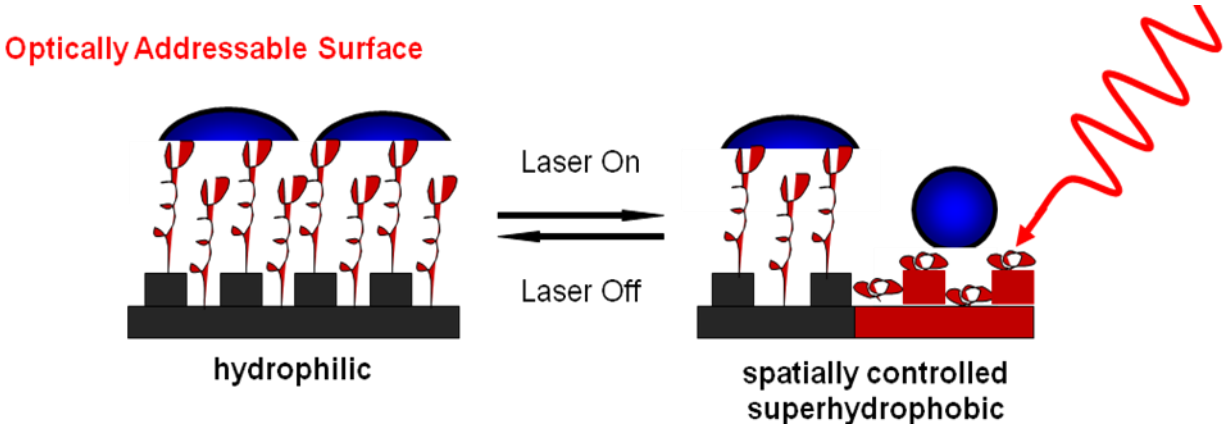

Figure 2-15. Depiction of a substrate for optothermal surface energy control capable of obtaining drastic contact angle switches.

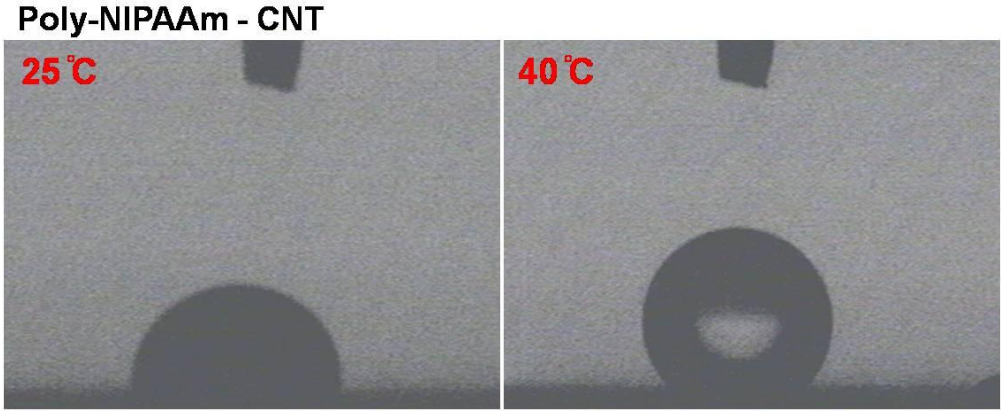

Figure 2-16. Contact angle images of unpatterned VANT substrate functionalized with azide polymer initiator and subsequently subjected to NIPAAm polymerization conditions above and below the LCST of *poly*-NIPAAm. Contact angle at 25 ºC is 100º. Contact angle at 40 ºC is 138º. Unpatterned VANT : *poly*-NIPAAm substrates often showed inhomogeneous contact angles which is explained by varying degrees of polymerization across and between substrates.

To increase the contact angle switch we pushed the system into the Cassie regime, i.e. supported on pillars, by adding microscale roughness to the substrates. Such roughness was obtained by growing robust VANTs on photolithographically patterned square catalyst arrays (Figure 2-2). Patterned nanotube substrates were found to be initially superhydrophobic, but relaxation down to superhydrophilic state was common as the water wicks along the hydrophilic silicon surface. After functionalization and polymerization, a consistent and increased temperature dependence of the contact angle was observed, with the substrates switching between 120º (hot) and 60º (cold).

Optothermal contact angle switching was also observed using a nIR diode laser (785 nm 450 mW) focused on the substrate (Figure 2-17a). Under laser irradiation, the contact angle was maintained at 120º, relaxing to 60º when irradiation ceased. This was repeatable, though the substrate could char if overheated. In an attempt to increase the hot contact angle and access the superhydrophobic regime, we utilized the fact that the azide functionalization employs chemistry that is selective for carbonaceous materials, leaving the silicon substrate undisturbed. This allowed the hydrophobicity of the silicon substrate to be increased through further functionalization. This was accomplished by exposing the functionalized substrate to a perfluoro-alkyltriethoxysilane. This surface treatment increased the hot contact angle to 136º and the cold contact angle to 65º (Figure 2-17b), though superhydrophobicity was not realized. In a final effort to increase the hot contact angle and decrease the likelihood of pinning, we attempted to grow VANTs of the top of Silicon pillars (obtained by Si etching after photolithography, obtained from Brian Kessler). Unfortunately, the ability to evaporate catalyst solely on the top of the pillars was not realized (Figure 2-18) and the complicated substrates performed much as the arrays of VANTs. Although we were not able to switch the surfaces to the superhydrophobic regime (sliding angle <5º), this work represents the first demonstration of *poly*-NIPAAm surfaces that respond to light.

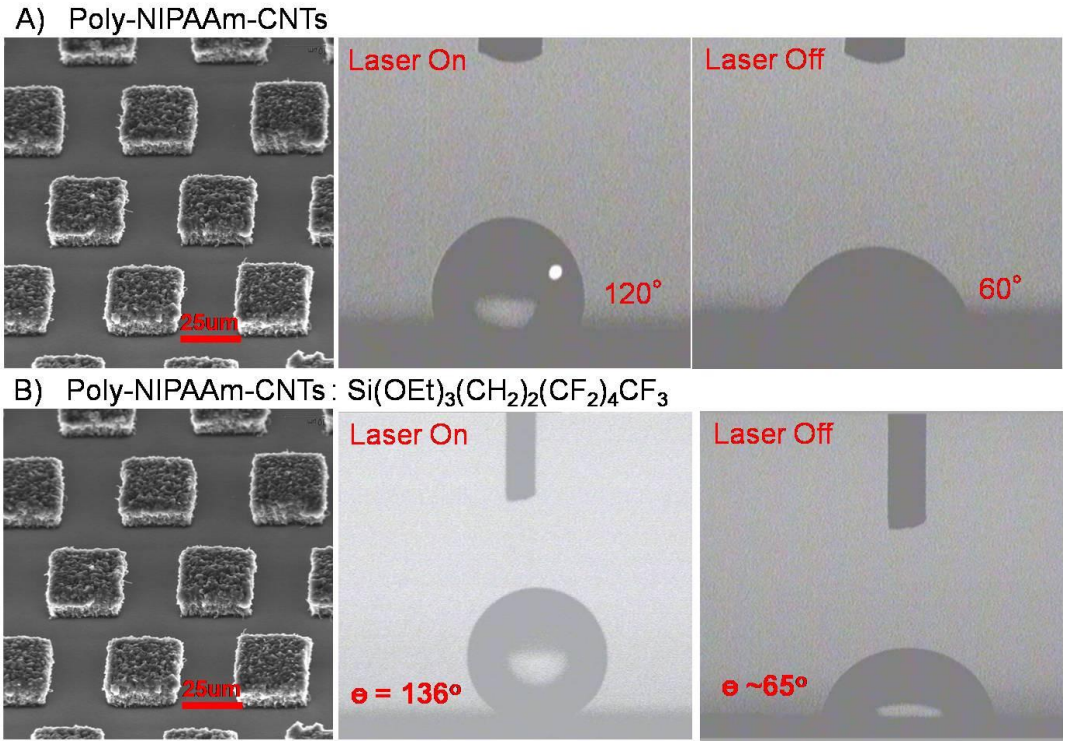

Figure 2-17. Scanning electron micrograph of poly-NIPAAm functionalized patterned VANT substrates. Contact angle images with and without optothermal heating. For as functionalized substrates optothermal heating produces a contact angle of 120□ vs. 60□ when at room temperature. For functionalized substrates with a perfluoro alkyl self assembled monolayer on the surface, optothermal heating produces a contact angle of 136□ vs. 65□ when at room temperature.

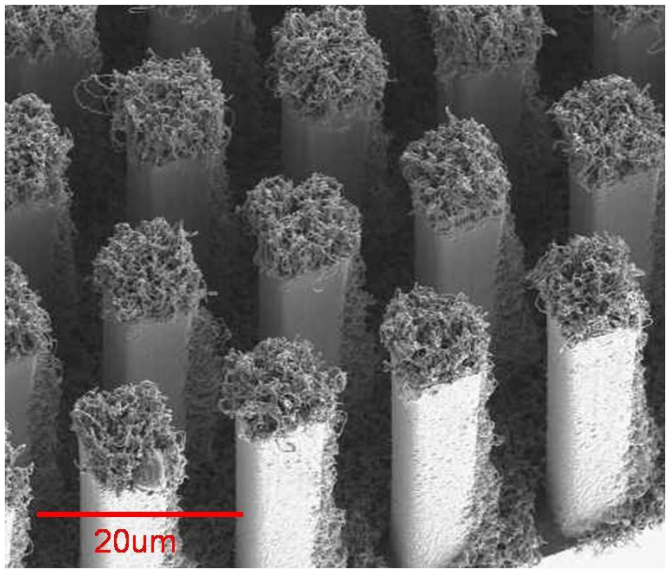

Figure 2-18. SEM of Silicon pillars with VANTs grown off the top and one side as a result of poorly controlled catalyst deposition.

2.6 Conclusion

We have developed a CVD technique for producing robust VANTs that are suitable for surface coating applications. We further developed a simple and selective patterning method for the functionalization of VANTs. This was used to produce superhydrophilic patterns on superhydrophobic backgrounds at the micro- and macroscale. Functionalization with a thermally responsive polymer imparted an optothermally modulated surface energy–allowing for remotely controlled contact angles with switches greater than 70º. These developments enable the possibility of further designing VANT-based materials that couple the optical and/or electrical properties of aligned CNTs to chemical modification.

---

1 Schild, H. G. *Prog. Polym. Sci.* **1992,** *17*, 163-249.

2 Sun, T.; Wang, G.; Feng, L.; Liu, B.; Ma, Y.; Jiang, L.; Zhu, D. *Angew. Chem. Int. Ed.* **2004,** 43, 357-360.

3 Feng, X.; Jiang, L. *Adv. Mater.* **2006,** *18* , 3063-3068.

4 Gao, L.; McCarthy, T. J. *Langmuir* **2007**, *23*, 3762-3765.

5 Cassie, A. B. D.; Baxter, S. *Trans. Faraday Soc.* **1944,** *40*, 546. Cassie, A. B. D. *Discuss. Faraday Soc.* **1948**, *3*, 11–16.

6 Wenzel, R. N. *Ind. Eng. Chem.* **1936,** *28*, 988.

7 Johnson, R. E. Jr.; Dettre, R. H. *Adv. Chem. Ser.* **1964,** *43*, 112.

8 Images adapted from: Feng, X.; Gao, X.; Wu, Z.; Jiang, L.; Zheng, Q. *Langmuir* **2007**, 23, 4892-4896.

9 Tasis, D.; Tagmatarchis, N.; Bianco, A.; Prato, M. *Chem. Rev.* **2006,** *106*, 1105-1136.

10 Yang, Z. P.; Ci, L.; Bur, J. A.; Lin, S. Y.; Ajayan, P. M. *Nano Lett.* **2008,** *8*, 446-451.

11 Carlson, L. J.; Maccagnano, S. E.; Zheng, M.; Silcox, J.; Krauss, T. D. *Nano Lett.* **2007,** *7*, 3698-3703. O'Connell, M. J.; Bachilo, S. M.; Huffman, C. B.; Moore, V. C.; Strano, M. S.; Haroz, E. H.; Rialon, K. L.; Boul, P. J.; Noon, W. H.; Kitrell, C.; Ma, J.; Hauge, R. H.; Weisman, R. B.; Smalley, R. E. *Science* **2002,** *297*, 593-596.

12 (a) Watts, P, C, P.; Lyth, S. M.; Mendoza, E.; Silva, S. R. P. *Appl. Phys. Lett.* **2006,** *89*, 103113. (b) Chakrapani, N.; Wei, B.; Carrillo, A.; Ajayan, P. M.; Kane, R. S. *Proc. Natl. Acad. Sci. U.S.A.* **2004,** *101*, 4009-4012.

13 Hata, K.; Futaba, D. N.; Mizuno, K.; Namai, T.; Yumura, N.; Iijima, S. *Science* **2004,** *19*, 1362-1364.

14 Thermal attachment of azides to CNTs: (a) Holzinger, M.; Abraham, J.; Whelan, P.; Graupner, R.; Ley, L.; Hennrich, F.; Kappes, M.; Hirsch, A. *J. Am. Chem. Soc.* **2003,** *125*, 8566-8580. (b) Holzinger, M.; Vostrowsky, O.; Hirsch, A.; Hennrich, F.; Kappes, M.; Weiss, R.; Jellen, F. *Angew. Chem. Int. Ed.* **2001,** *40*, 4002-4005.

15 Photochemical attachment of azides to CNTs: (a) Moghaddam, M. J.; Taylor, S.; Gao, M.; Huang, S.; Dai, L.; McCall, M. J. *Nano Lett.* **2004,** *4*, 89-93. (b) Lee, K. M.; Li, L.; Dai, L. *J. Am. Chem. Soc.* **2005,** *127*, 4122-4123.

16 (a) Keana, J. F. W.; Cai, S. J. X. *J. Org. Chem.* **1990,** *55*, 3640-3647 (b) Cai, S. X.; Nabity, J. C.; Wybourne, M. N.; Keana, J. F. W. *Chem. Mater.* **1990,** *2*, 631-633

17 Feng, X.; Jiang, L. *Adv. Mater.* **2006,** *18* , 3063-3068.

18 Gao, L.; McCarthy, T. J. *Langmuir* **2007**, *23*, 3762-3765.

19 Forests coated with fluorinated material: (a) Lau, K. K. S.; Bico, J.; Teo, K. B. K. Chhowalla, M.; Amaratunga, G. A. J.; Milne, W. I.; McKinely, G. H.; Gleason, K. K. *Nano Lett*. **2003,** *3*, 1701-1705. (b) Li, H.; Wang, X.; Song, Y.; Liu, Y.; Li, Q.; Jiang, L.; Zhu, D. *Angew. Chem. Int. Ed.* **2001,** *40*, 1743-1746.

20 Representative examples: (a) Lopez, G. P.; Biebuyck, H. A.; Frisbie, C. D.; Whitesides, G. M. *Science* **1993**, *260*, 647-649. (b) Sun, T.; Wang, G.; Liu, H.; Feng, L.; Jiang, L.; Zhu, D. *J. Am. Chem. Soc.* **2003**, *125*, 14996-14997.

21 (a) Zhai, L.; Berg, M. C.; Cebeci, F. C.; Kim, Y.; Milwild, J. M.; Rubner, M. F.; Cohen, R. E. *Nano Lett.* **2006,** *6*, 1213-1217. (b) Garrod, R. P.; Harris, L.G.; Schofield, W. C. E.; McGettrick, J.; Ward, L. J. Teare, D. O. H., Badyal, J. P. S. *Lagmuir*, **2007,** *23*, 689-693.

22 Parker, A. R.; Lawrence, C. R. *Nature* **2001**, *414*, 33.

23 Matyjaszewski, K.; Xia, J. *Chem. Rev.* **2001,** *101*, 2921-2990.

24 Sun, T.; Liu, H.; Song, W.; Wang, X.; Jiang, L.; Zhu, D. *Angew. Chem. Int. Ed.* **2004,** *43*, 4663-4666.

25 Xu, G.; Wu, W-T.; Wang, Y.; Pang, W.; Wang, P.; Zhu, Q.; Lu. F. *Nanotechnology* **2006,** *17*, 2458-2465

26 Sun, T.; Wang, G.; Feng, L.; Liu, B.; Ma, Y.; Jiang, L.; Zhu, D. *Angew. Chem. Int. Ed.* **2004,** 43, 357-360.

Chapter 3:

Optothermally Controlled Motion via Surface Tension Manipulation

Temperature influences a multitude of system parameters, allowing optothermally defined temperature gradients to be translated into gradients for other system parameters. For instance, an optothermal temperature gradient on the surface of a liquid is in effect a surface tension gradient due to the temperature dependence of the surface tension. When an object is placed in a surface tension gradient it feels an asymmetry of attractive forces[1] and is pulled toward higher surface tension. Thus, if optothermal methods can be used to spatially define surface tension gradients, they can be used to move objects on liquids. This is a particularly interesting concept because light, specifically sunlight, provides a vast resource that has spurred the development of various methods to convert photons into work: photovoltaics for conversion to electricity, solar thermal for water heating, fast growing plants to produce bio-fuels, and solar water splitting to produce hydrogen and oxygen.[2] Though useful, these disparate methods are often based on complicated, capital intensive, multistage processes:[3] light is collected and converted to a high energy intermediate (e.g. electrical potential, thermal loading, or chemical fuel), which is then used to run a process, such as an engine, that performs work. This multistage approach is ubiquitous and allows for a myriad of applications, but requires production, transportation, and possible storage of energetic intermediates. Considerable effort has been devoted to improving energy collection, storage, and utilization,[3,4] however strategic simplification through the removal of the intermediates remains under-investigated and could reduce capital costs. Here we report that a simple and robust solid/fluid interfacial system can convert light into useful work through thermally manipulated surface tension effects. This was demonstrated by the propulsion of objects on the surface of water. The simplicity of the system allows for work in the form of controlled linear motion, rotational motion, and volumetric expansion.

Few strategies exist for the direct conversion of light into work. Concepts such as the solar sail[5] for interstellar travel and optical trapping of small particles[6] rely on weak momentum transfer from photons. Harnessing the energy of photons is a far more powerful process. A few optothermal methods have been developed;[7] for example, the Crookes Radiometer produces rotational motion in part via light-based heating of gases, but requires stringent conditions (i.e. low pressure) to function. When applied to liquids, local heating can produce thermally induced surface tension gradients. Such gradients have been shown to induce thermocapillary convective flows in oil-water systems[8] and as first realized by Brochard-Wyart et al., can move silicone oil droplets on hydrophobic surfaces[9] or water droplets in oil filled channels.[10] Nature has shown that surface tension gradients, created from chemical gradients, can move solids, such as insects, on the surface of water.[11] Similarly, camphor chips,[12] soap boats,[13] and decomposing hydrogen peroxide[14] have been used to produce surface tension gradients and motion in the laboratory, but all inherently rely on the exhaustible supply of chemical intermediates to function. Our goal was to couple optical heating with the capability of surface tension gradients to move objects on the surface of liquids. With this approach, a direct means of converting light into useful work was realized, and a simple strategy for remotely powering and controlling small objects was demonstrated.

We showed that with a highly absorptive material capable of locally converting light energy into heat, concentrated light can be used to selectively generate thermal surface tension gradients and move objects on the surface of a liquid, such as water (Figure 3-1). This approach combines energy collection and utilization into one material. Furthermore, the interfacial system allows control to be readily enacted in two ways: (i) selectively focusing light on different regions of the absorber to affect the direction of the exerted forces (section 3.4 Controlled Linear Motion from

Focused Irradiation); and (ii) through device design providing specific orientations of the light absorbing material within the device (section 3.5 Rotational Motion from Blanket Irradiation). This versatility gives access to work in the form of controlled linear motion, rotational motion, and volumetric expansion (section 3.6 Controlled Self-Assembly).

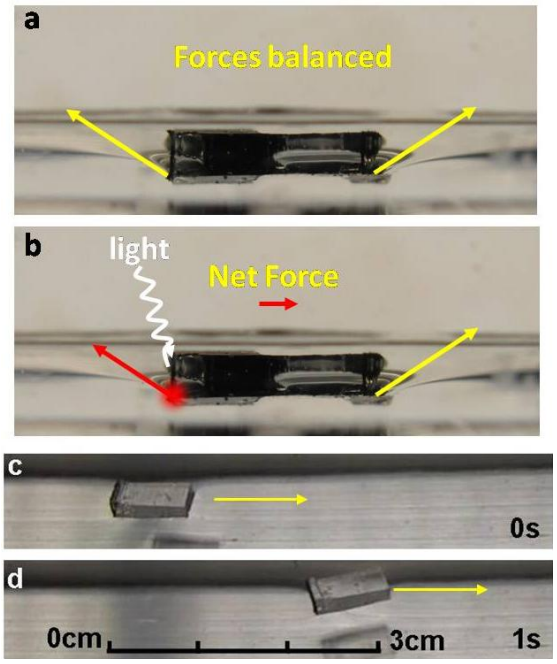

Figure 3-1. Light-based control of absorbing objects on water. Side-view of an opaque PDMS boat floating on water (a-b) with surface tension forces depicted by yellow arrows. When at rest the surface tension forces are equal and opposite and no motion is produced (a). When one face of the object is heated by light (b), the surface tension locally decreases (red arrow), resulting in asymmetric surface tension forces and a net force toward the right. Motion ensues. Optical images (c-d) of a VANT-PDMS composite in a water filled trough show the linear propulsion described in (b). The VANT-PDMS object is briefly irradiated at time zero with focused near-IR light (450 mW) just right of center on the back (left), absorbing face of the object. The laser source is roughly 13 cm away, with the beam nearly grazing the surface of the water, and the focus set to coincide with the absorbing face of the object.

Carbon black, multiwall carbon nanotubes (MWNT), and vertically aligned carbon nanotube forests (VANTs) can be used to produce responses.[15] We focused on VANTs as a highly absorptive surface material to maximize heating close to the interface with the liquid. Low density VANTs, with very high surface roughness, have recently been reported to be the blackest known material, absorbing greater than 99.9% of incident visible light.[16] Thermal relaxation of excited electrons converts absorbed light into heat, thus making VANTs ideal light-activated thermal switches which can heat the surrounding liquid and maximize surface tension gradients.

3.1 Carbon Nanotube Synthesis

VANTs were grown by chemical vapor deposition[17] on silicon substrates with ~1.5 nm Fe on 10 nm Al_2O_3 as a catalyst system. The substrates were loaded into a 1" quartz tube in a

Linderberg/Blue M Mini-Mite Tube Furnace, heated to 450 °C under 200 standard cubic centimeters per minute (sccm) nitrogen, soaked in a reducing atmosphere (hydrogen 40 sccm: nitrogen 200 sccm) for 5 minutes, and then heated to 750 °C. Ethylene (40 sccm) was introduced for 2 - 30 minutes along with 2 sccm of water saturated nitrogen. VANTs were characterized with scanning electron microscopy (SEM) conducted with a FEI Sirion XL30 SEM. The VANTs were tens to hundreds of microns tall with average diameters of ~10 nm, Figure 3-2.

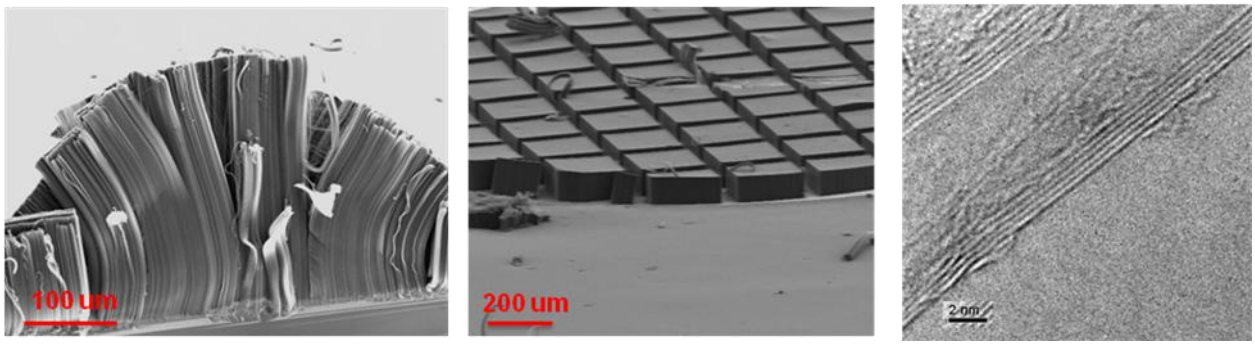

Figure 3-2. Scanning electron micrographs of as grown VANTs (left, center). Transmission electron micrograph of a carbon nanotube (right).

3.2 Composite Production

To increase the structural integrity and maintain the roughness necessary for high absorptivity, VANTs were embedded in a supporting polymer (Figure 2-3). Polydimethylsiloxane (PDMS) was employed for four reasons: (i) it is optically transparent, focusing absorption on the thin nanotube surface layer; (ii) it has a density similar to that of water; (iii) it strongly adheres to the VANTs; and (iv) it provides elasticity while maintaining the nanoscale roughness and macroscopic structure of the forests. VANT-PDMS composites were prepared by contact curing PDMS (Slygard 184 Silicone Elastomer Kit) on VANT substrates preheated to 200 °C, followed by pulling the cured composite off the substrate. This prevented the PDMS from fully impregnating the VANT substrate and left the bottom ends of the nanotubes exposed. The embedded forests emerge from the PDMS by ~100 μm (Figure 3-3) and are stable to solvents and mild mechanical pressure.

The VANT-PDMS composites (Figure 3-3a,b) are stable to water and solvents, are superhydrophobic with contact angles of >155º (Figure 3-4) and can be created with various shapes and orientations. Surface contact angles were measured on a Krüss Model G10 goniometer at room temperature and ambient relative humidity using 18 MΩ water according to the sessile drop method. Composites can be cut to any desired shape. Alternative light absorbing materials such as homogenous carbon black-PDMS and MWNT-PDMS composites were made by thoroughly mixing the absorbing material (1-5 wt%) with PDMS and curing at 100 ºC in a box furnace for 2 hours.

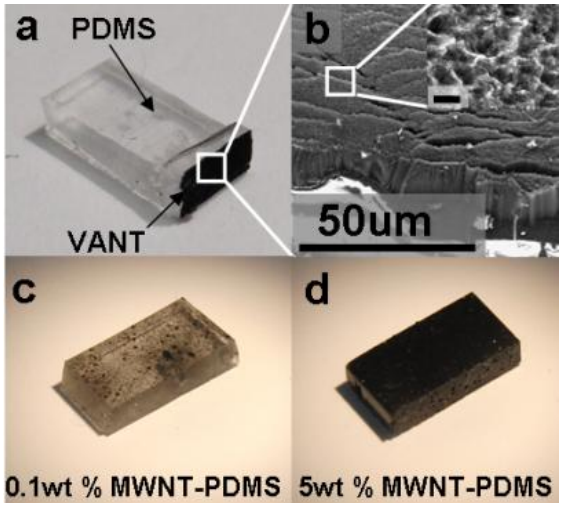

Figure 3-3. Nanotube-PDMS composites. VANT-PDMS (a) with zoomed in scanning electron micrographs (b) and inset, after exposure to water and isopropyl alcohol. Scale bar in inset is 10um. Optical images of 0.1 wt% MWNT-PDMS (c), 5 wt% MWNT-PDMS composites (d). The VANT-PDMS composite contains roughly 0.1 wt% NTs localized at the back face.

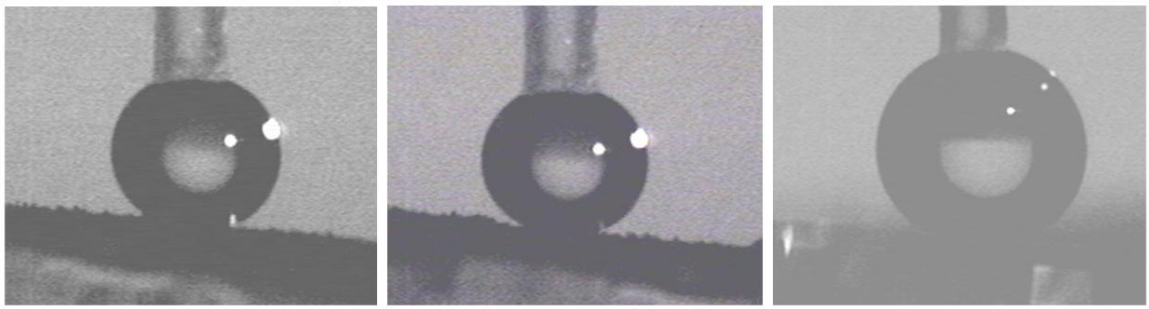

Figure 3-4. Characteristic contact angle images for VANT-PDMS composites. Droplets quickly roll off the substrate if not held by the needle. Contact angles are consistently >155º. Droplets bounce off the surface when dropped from a distance. Pinning only occurs at defect sites.

When subjected to focused sunlight or a near-infrared (nIR) laser[18] (450 mW, 785 nm B&W Tek, Inc 785-450E/55371 Diode Laser), the VANT-PDMS composites heat dramatically. Laser induced heating of composites was tested by embedding a thermocouple in the PDMS support, close to the back of the VANT. Collimated laser irradiation was used to observe the temperature change. This gave an estimate of the temperature change in air at 150 °C. This is likely a lower limit as the thermocouple was not placed directly at the interface to avoid direct heating of the probe or photoelectric effects. A temperature change as a result of the direct irradiation of the thermocouple was eliminated as no change in temperature was found when the thermocouple was placed behind, but not in contact with the composite under illumination. Under static conditions, water droplets can be boiled and carbonaceous material on the VANTs can be burnt in air. When placed in a liquid, this dramatic heating of the VANTs lead to significant temperature gradients as the substrate transfers energy to the surrounding liquid.

3.3 Composite Testing

To test the ability of light to control linear motion, VANT-PDMS composites were floated on liquids and sunlight or laser light was focused on the VANTs. Illumination conditions varied, though motion was typically tested with the object near the focal point and roughly 5-20 cm away. Light induced heating resulted in linear propulsion (Figure 3-1c-d) without boiling.

Surface tension based force responses are directly related to the temperature differential and the contact length of the heated interface. For our test system we chose to focus on the millimeter scale, where powering and controlling motion are normally difficult due to viscous effects[13,19] and machining limitations. For VANT-PDMS composites of millimeter dimensions under focused laser illumination, we obtained speeds up to 8 cm/s and forces of 29 μN.[20] These results are at par with reports from chemically fueled surface tension based propulsion systems.[21] This force suggests a local increase in temperature of as much as 50 ºC. In principle, the power density of the motors may be raised by increasing the length of the heated area, perhaps through the use of a multi-fin system (section Future Work).

Speed tests for force quantification were performed in an aluminum trough filled with the appropriate liquid. Both continuous illumination and single pulse illumination experiments were undertaken. Objects tested ranged from 20 mg to 25 g and <1 mm to multiple centimeters and showed light responses. Resulting motion was recorded using a Casio Exlim Pro EX-F1 at 30-1200 frames per second. Video analysis was performed using ImageJ.[22] Motion typically began within 0.1 s of illumination. For heavy composites a qualitatively longer lag was observed but not quantified. Analysis and results are discussed in the 3.3a Force Quantification section.

To verify that the motion of the objects was the result of optothermal heating we performed a number of control experiments as discussed thoroughly in the following sections. Briefly, we verified that optothermal heating was occurring; verified that non-absorbing objects did not move (Figure 3-6); verified that the direction of incident irradiation did not drastically affect the resulting motion (3.3b Absorber Comparison section); verified that disrupting the surface tension of the liquid reduced motion (3.3c Surfactant Effect and 3.3d Solvent Effect sections); verified that the forces generated were of the order of magnitude anticipated from theory; and verified that carbon nanotubes were not the only absorber to produce motion (3.3b Absorber Comparison section).

3.3a Force Quantification

Force values were determined by evaluating the recorded motion of the composites using ImageJ[23] software with Manual Tracking to determine the location of the object at each time point. With this location and time information Igor Pro 6.04 was used to fit the data to theory. To determine the force associated with constant illumination we began with the net force equation:

$$F_{net} = F_L - Rv^2 = ma \tag{1}$$

$$R = \tfrac{1}{2}\rho A C_D \tag{2}$$

where F_{net} is the net force, F_L is the force due to the light based modulation of the surface tension, m is the mass of the composite, R is defined from the drag equation as in (2): v is the velocity, a is the acceleration, ρ is the density of the solution, A is the cross-sectional displaced area, and C_D is the drag coefficient. Integrating equation 1 twice gives the location as a function of time (equation 3):

$$X = \frac{m}{R}\log\left[\cosh\left(\frac{\sqrt{F_L * R}}{m}(t - t_0)\right)\right] - D \qquad (3)$$

where X is the location, and t_o, and D are integration constants. A typical location vs. time plot with fit is shown in Figure 3-5.

Temperature changes were calculated from the force measurements using the temperature dependence of the surface tension. For instance, the temperature dependence of the surface tension for water is ~1.8 μN/cm K. If the absorber has an absorbing face of 0.2 cm and the derived force is 10 μN, one obtains a change in temperature of ~28 K as shown in equation 4:

$$\frac{10\mu\text{N}}{1.8\mu\text{N/cm K} * 0.2\text{cm}} = 28K \qquad (4)$$

With these values in hand we are able to evaluate the performance of different absorbing materials and liquids.

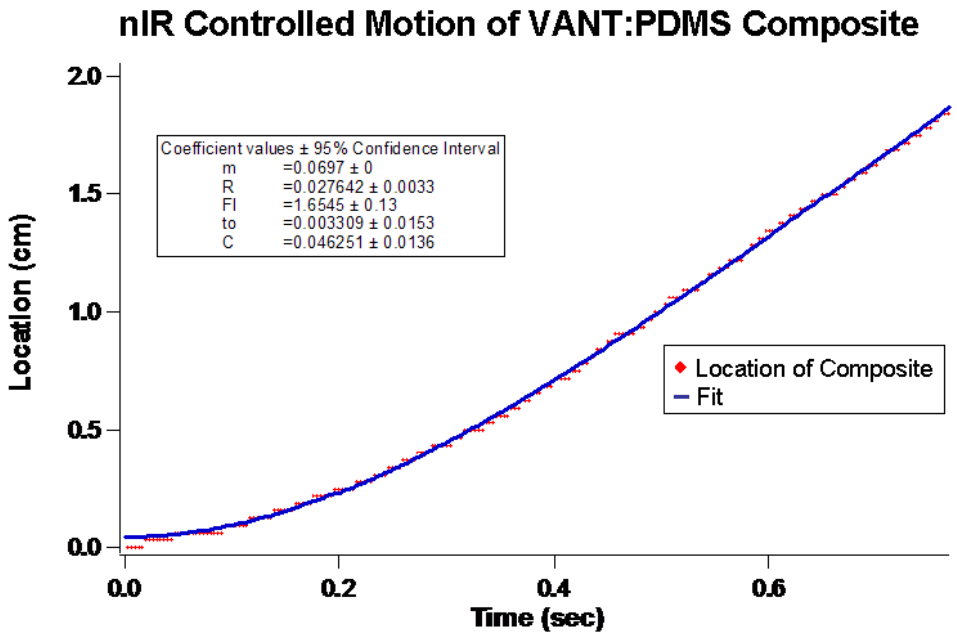

Figure 3-5. Motion induced by the continuous irradiation of a VANT-PDMS composite with 400 mW of 785 nm laser light. The location data and fit with fit parameters are shown. For the fit, m is in grams, R is in grams/cm, t_o is in seconds, Fl is in 10 μN, and C is in cm. In this case, the force on the object was roughly 16.5 μN.

3.3b Absorber Comparison

To investigate the effect of light absorption on the system, we compared VANT-PDMS composites with dispersed composites of MWNT and PDMS (MWNT-PDMS) as shown in Figure 3-3a-d. Larger composites (~250 mg) were tested so as to normalize the effective absorbing area.[24] Typical motion curves are shown in Figure 3-6. Incorporation of 1-5 wt% MWNT produces an opaque black composite that performs similarly to the VANT-PDMS composite, with forces of 1.9 ±0.3 μN, 2.2 ±0.3 μN, 2.9 ±0.9 μN for the 1 wt%, 5 wt% and VANT composites respectively (errors are reported as the standard deviation). Less absorbing 0.1 wt% MWNT-PDMS composites were gray (Figure 3-3c) and produced ~60% less force, 1.0 ±0.1 μN, compared to VANT-PDMS. It should be noted that latent heat of the objects, after testing, causes them to continue to be propelled forward. This is more obvious with the dispersed composites, which absorb throughout the material, then with the VANT-PDMS composites. This suggests that the VANT-PDMS composites transfer heat more effectively to their surroundings then the dispersed composite and with further study may provide significantly better performance.

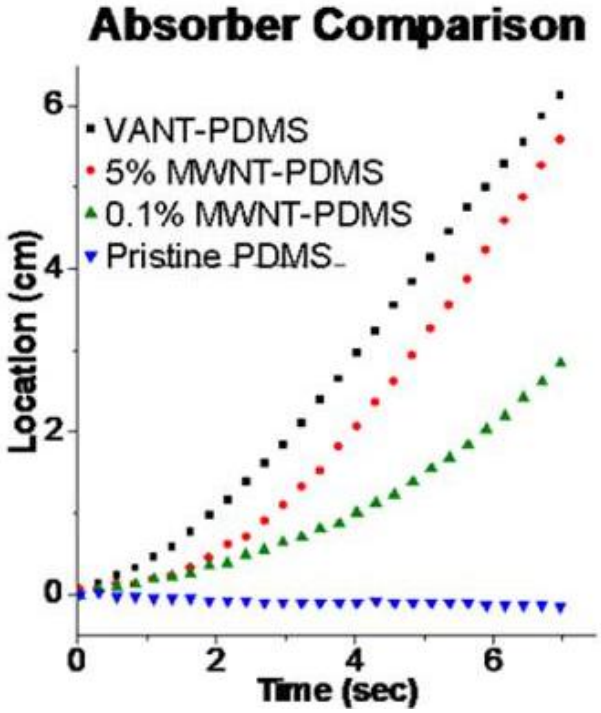

Figure 3-6. Motion curves for VANT-PDMS, 5 wt% MWNT-PDMS, 0.1 wt% MWNT-PDMS and pristine PDMS under constant, collimated laser illumination beginning at t ~0 s.

Because VANT-PDMS composites only have absorbing material on one face (i.e. the back of the boat) and are otherwise transparent, one can optothermally heat the absorber both from behind (Figure 3-7) and from the front (with the laser beam passing through the transparent

PDMS). Typical forward motion is observed in both cases, suggesting that radiation pressure from the incident light is not a dominant factor.

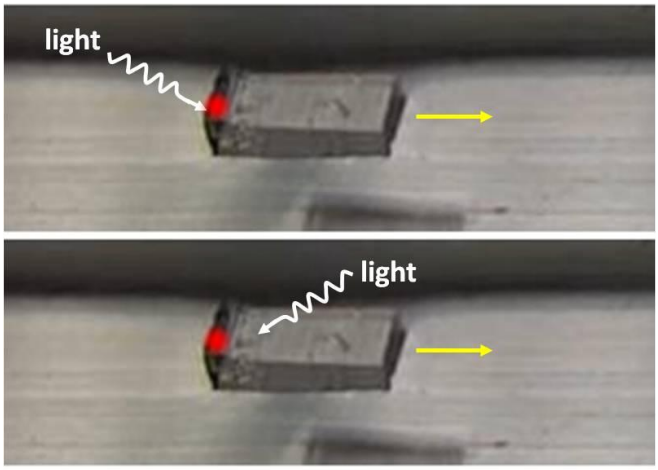

Figure 3-7. Optical images depicting radiation pressure control experiment. The direction of irradiation and location of absorption were added. Top, irradiation from the back (left) heats up the back absorbing face and produces forward (right) motion. Bottom, irradiation from the front (right), through the PDMS, heats up the absorbing face and also produces forward (right) motion.

3.3c Surfactant effect

Surfactants have recently been observed to eliminate surface tension responses in liquids[25] and thus provide a useful control to verify the cause of motion in our system. To test surfactant effects on the light controlled motion of objects, VANT-PDMS composites (3 mm x 10 mm x 1 mm) were floated on water in an aluminum trough (64 cm x 3.3 cm x 1.5 cm) and irradiated with a nIR laser to verify light induced motion. Sodium dodecyl sulfate (SDS) (~70 mg) was dropped onto the surface of the solution and allowed to dissolve (~0.5 min). The composite was then irradiated with nIR light. No motion was observed even under the highest focus, as shown in Figure 3-8. When laser light was highly focused, bubbles formed as the water locally boiled, a phenomenon not observed in pure water. If an intermediate amount of surfactant was used (~30 mg), light induced motion was retarded but not completely eliminated for highly focused irradiation. This suggests that the laser induced motion is a surface tension related phenomenon.

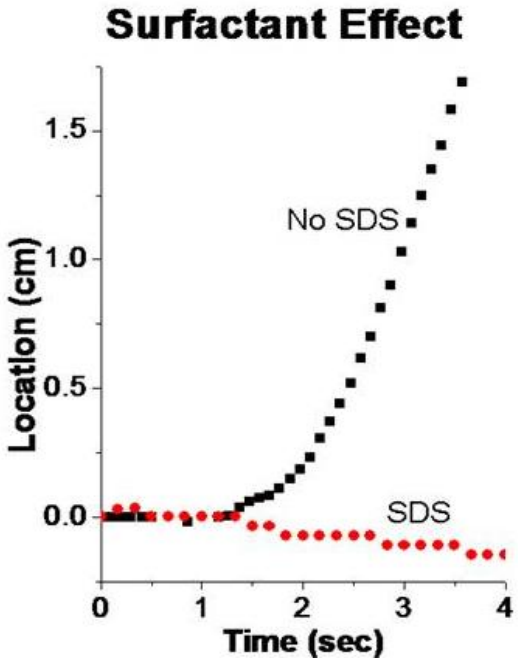

Figure 3-8. Location vs. time plot for a VANT-PDMS composite under constant collimated laser illumination with and without the addition of surfactant, SDS. The quenching effect of the surfactant results in no motion of the composite. Illumination began at t~1.3 s.

3.3d Solvent Comparison

To test the effect of the liquid on the light controlled motion of objects, VANT-PDMS composites (3 mm x 10 mm x 1mm, 36.2mg) were floated on water, isopropyl alcohol, or DMF (Figure 3-9) and the response was quantified.[26] Small composites were used so as not to break the surface tension holding the object above the surface. The objects were then irradiated with nIR laser light at an angle of 45º and the motion recorded. In order to control illumination intensity, constant collimated laser conditions with a spot size larger than the absorbing area of the boat (~4.5 mm) were used. Forces were determined as described in the *Force Quantification* section. In water, forces of 1.19 ±0.36 μN were observed over seven measurements, error is reported as plus or minus one standard deviation. We anticipated smaller forces with other liquids, as their thermocapillary coefficients are smaller. In isopropyl alcohol, forces of 0.23 ±0.12 μN were observed over five measurements. In DMF, forces of 0.13 ±0.03 μN were observed. The forces correlate to temperature changes of 2.9 ºC for the water system and 0.96 ºC for the isopropyl alcohol system. Motion was also observed on Fluorinert® FC-75, brine, glycerol, or at the boundary between water and Fluorinert®, but the forces were not quantified. The obtained solvent dependence on the generated force appears complicated and may be attributed to differences in the heat capacities, buoyancy, viscosity and the temperature dependence of the surface tension. These effects require further investigation.

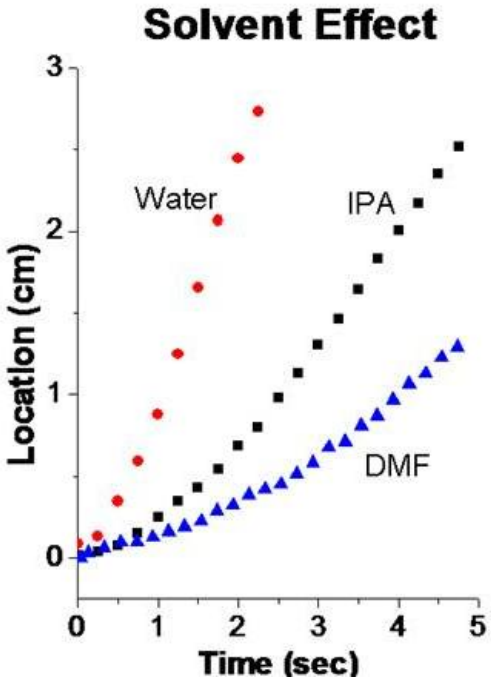

Figure 3-9. Location vs. time plots for a VANT-PDMS composite under constant collimated laser illumination. Motion curve depicting the distance travelled by VANT-PDMS composites in water, IPA or DMF filled troughs under nIR laser illumination, beginning at t~0 s.

To summarize the results: (i) no response was observed when irradiating transparent PDMS objects lacking absorbing materials; (ii) substantial heating of substrates was observed when irradiated; and (iii) motion was quenched upon addition of surfactant, which cuts surface tension effects. With these facts in mind, it appears clear that optothermal surface tension gradients are the cause of the laser induced motion.

3.4 Controlled Linear Motion from Focused Irradiation

The simplicity of this system allows it to be easily applied to multiple forms of work: spatially controlled illumination gives controlled "linear" motion, while specific device design can produce rotational motion. Controlled linear motion was obtained by focusing light on different parts of the object, dictating the loci of the relevant temperature gradient and thus the direction of the exerted surface tension force and the motion (Figure 3-10 top). This remotely controlled and powered sub-centimeter object, which is not limited by external fields,[13,22] is a clear example of the utility of the technique. Our approach provides a simple, scale-independent[27] and robust way to produce directionally controlled linear motion. Objects ranging in size from the millimeter (milligrams) to tens of centimeters (tens of grams) were controllably moved with a laser or concentrated sunlight. This scale independence and versatility of light sources presents an advantage over other optical techniques such as optical trapping.

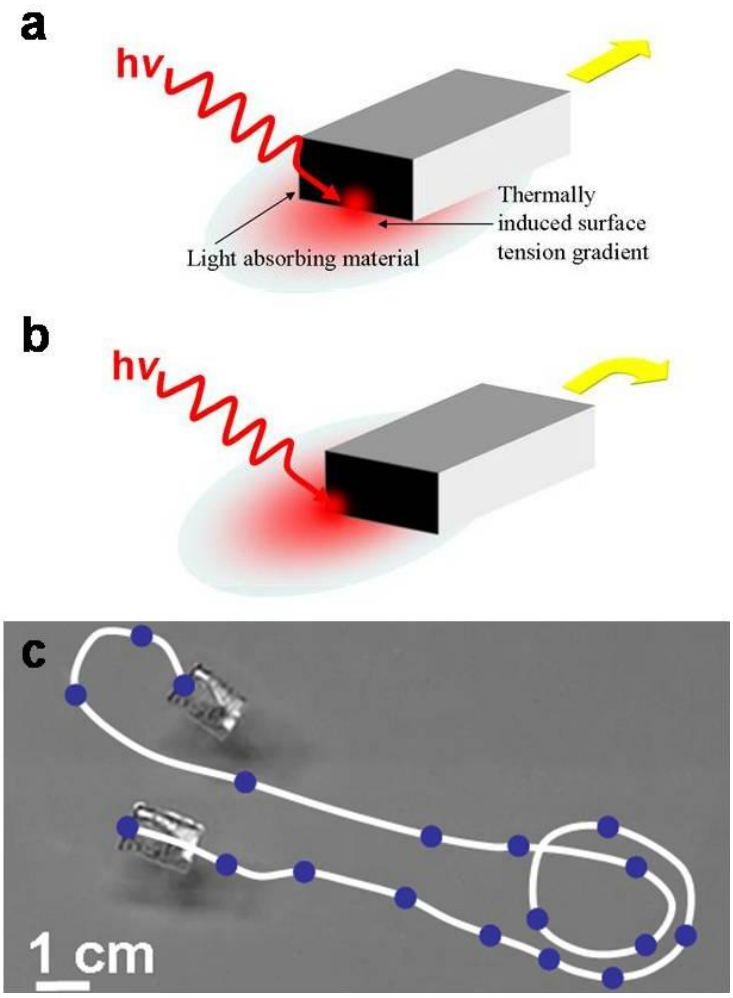

Figure 3-10. Light controlled linear motion of a VANT-PDMS composite floating on water. When illuminated, as in (a), the retarding surface tension force diminishes and the object is pulled forward. Alternatively, when the back-left side is heated (b), an asymmetry of forces is created, resulting in forward and right turning propulsion. Such selective irradiation can be used to produce and remotely control motion. Top view composite image of a VANT-PDMS object floating on water (c) with the top colored black to aid the eye. The white line shows the path of the composite, with the dots representing two second time points. The composite is directed to the right, turned around in a circle and sent back to the left. The final location of the boat has been superimposed upon the original image.

3.5 Rotational Motion from Blanket Irradiation

Rotational motion can be achieved by introducing directionality into the device design. For instance, by placing light absorbing VANTs on the clockwise face of each fin of a rotor (Figure 3-11), localized heating produces surface tension forces that cause the object to rotate in the counterclockwise direction. Alternatively, flipping the object over affords clockwise rotation. As shown in Figure 3-11, when placed under focused sunlight or irradiated with a near-IR laser these rotors spin at rates up to 70 rpm. Built-in directionality is particularly useful for sunlight powered motion, as it is relatively difficult to focus the sun on small moving objects. In this case, Fresnel lenses can be used to focus sunlight on floating rotors, resulting in continuous

rotation. Rotors can also be mounted on an axle or stiff metal wire, which may increase the utility of the rotors with potential application for simple solar powered pumps.

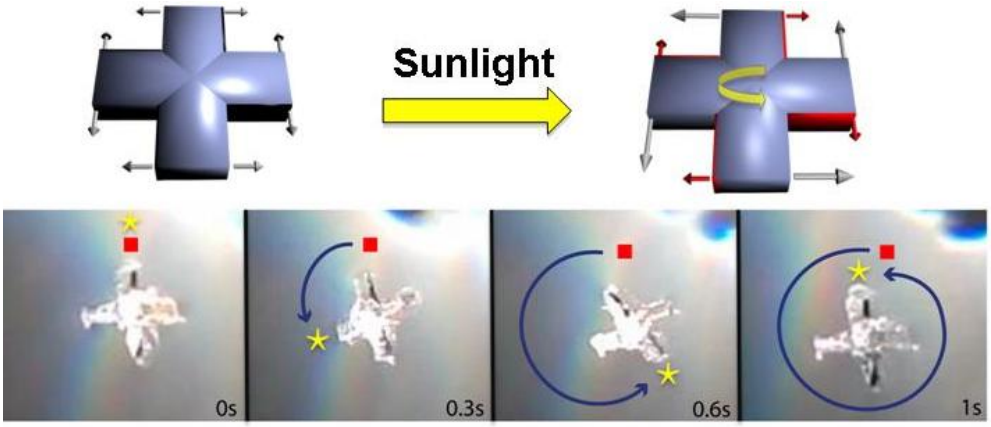

Figure 3-11. VANT-PDMS rotor timeline. Schematic (top) showing forces (gray arrows and with heating, red arrows) on the rotor with absorbing material embedded on the clockwise face of each fin while dark and illuminated. Timeline (bottom) of a VANT-PDMS rotor floating on deionized water with embedded VANTs on clockwise face of each fin and irradiated with focused sunlight. The square remains stationary as the star follows one fin.

3.6 Controlled Self-Assembly / Volumetric Expansion

Absorptive heating can also be directly translated into work in the form of volumetric or 2D expansion. On the surface of water, hydrophobic objects are pulled together by attractive capillary forces (Figure 3-12a).[28] Placing light-absorbing materials on a face of the hydrophobic objects introduces a handle for controlling capillary interactions. When focused light heats an interface between objects, the surface tension drops and the objects are pulled apart in a form of 2D expansion. The use of light-induced 2D expansionary work enables the study of the self-assembly of mesoscale objects on a surface. Whitesides and coworkers[27] have demonstrated that engineering the capillary forces on the faces of small PDMS objects can lead to their predictable self-assembly into ordered arrays. This notion was used to mimic biological and molecular self-assembly processes on the mesoscale.[29] In our system, instead of chemically defining surface interactions, we use light to control the capillary forces. This allows the sampling of energy states of an assembly through the use of light to generate an unstable high-energy state; this is then followed by relaxation into a new state, a process analogous in concept to protein folding methods that start from high-energy states and proceed through relaxation to various energy minima.

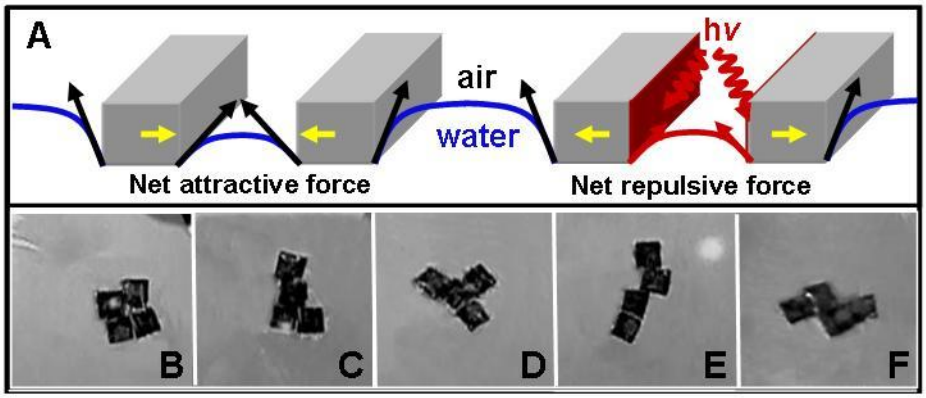

Figure 3-12. Energy states of VANT-PDMS Self-Assembly System. Schematic, **A,** of the assembly of two objects (left) and light induced control of the capillary forces (right). Top view optical images of five representative energy states of the mesoscale assembly of four VANT-PDMS objects (each 1 mm x 1 mm). States **C-F** are roughly equivalent in interfacial free energy while state **B** is close to the global minimum. Where necessary, shadows have been digitally removed for clarity.

In our system, PDMS objects with VANTs embedded on their bottom face self-assemble on the surface of liquids. The highly absorptive VANTs introduce superhydrophobicity and a high interfacial free energy and thus a significant driving force for assembly. Typically such systems have numerous local minimum energy states. For example, states **c**-**f** in Figure 3-12 are local energy minima, whereas state **b** is a global energy minimum that minimizes interfacial area. Figure 3-13 shows an example of laser-mediated introduction of energy into global minimum state **a**, with the eventual relaxation to state **e**. Repeated irradiation can move the objects through different states, allowing sampling of all possibilities. This tool may allow further understanding of dynamic multistate systems and the investigation of light-induced dynamic systems: systems that are active during the day while static at night.

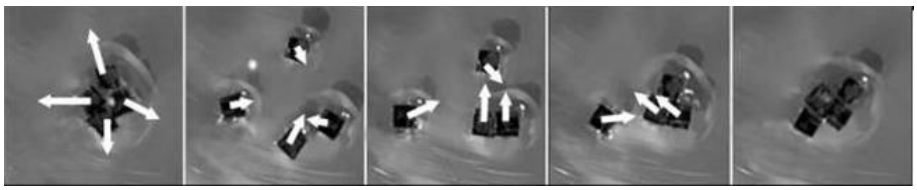

Figure 3-13. Timeline showing a light disrupted system. Mesoscale assembly of four VANT-PDMS objects (each 1 mm x 1 mm). Top view time sequence of laser induced disruption from one state (left-most panel, similar to the state of Figure 3-12b) to the reassembly to another state (right-most panel, similar to the state of Figure 3-12f). Laser irradiation only occurs at the junction between the four blocks in the first frame. Subsequent frames show capillary induced relaxation. Entire process occurs over a period of approximately three seconds. Arrows indicate instantaneous velocities. Where necessary, glare has been digitally removed for clarity.

3.7 Conclusion and Potential Extensions

In summary, we have presented a simple and versatile method for the conversion of light energy into useful linear, rotational, and volumetric work expressed through the motion of

objects on a liquid. Additionally, this demonstrates a solution to the challenging problem of remotely controlling the motion of small objects on water. It is important to note that in addition to harnessing sunlight to do work this effect scales linearly and can be extended into the micro and macro regimes. Future areas of interest for this system include direct quantification of the forces; force amplification through multiple absorbing fins; utilizing differential absorption to realize wavelength controlled motion on the microscale; and utilizing microscale rotors for microfluidic pumps.

3.7a Characterization and Optimization of Forces and Efficiencies

The utilization of light to produce motion is highly desirable and could have broad applications given sufficiently large forces and high efficiencies. To improve our current process it is necessary to better characterize the forces produced, possibly using cantilever deflection experiments. This allows us to obtain better metrics for efficiencies and forces and will allow further design enhancements and an improved understanding of the ultimate utility of the system. Surface tension forces scale with the length of the fluid/fluid(or gas)/solid contact line. To take advantage of this fact, we propose that a multi-finned design can be used to increase the effective contact line length per given area, and thus the amount of force generated (Figure 3-14). To maximize the force produced fins should be placed as closely as possible. There is likely a minimum effective fin thickness (w) and spacing (d) (Figure 3-14), which will dictate the obtainable force density that must be determined experimentally.

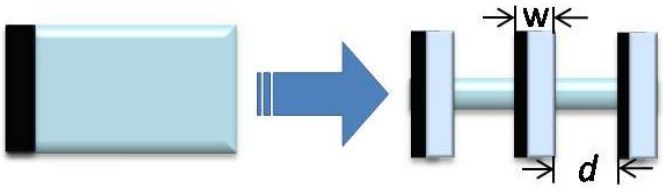

Figure 3-14. Since surface tension forces pull on all contact points with an object, increasing the heated contact line should increase the force. Fin thickness, w, and spacing, d, will dictate the effective force density.

Improved efficiencies may also be obtained by increasing the amount of light absorbed. This has been partially achieved using forests of carbon nanotubes (VANTs), which absorb >99.9% of incident light,[30] but further engineering of the placement and orientation of the nanotubes as well as the supporting material could substantially improve performance. Finally, the interaction between the VANTs and the surrounding liquid is of great importance. This interaction dictates the efficiency of the heat transfer from the composite to the solution. As a result, the magnitude of the surface tension gradient generated. To this end, we have recently developed a facile means of chemically modifying VANTs using azide containing small molecules (Chapter II). This technology can be used to modulate the surface energy of the VANTs and provide a means for optimizing the interaction of the absorbing material with the surrounding liquid.

3.7b Micro / Nanoscale Controlled Motion

An obvious extension for this surface tension driven system is to investigate the miniaturization of these optothermal motors. Because surface tension has a linear dependence on length, it can be a dominant force for systems of any size, including the very small. This presents an ideal opportunity for developing a new propulsive mechanism for nanomachines. Composites with spatially defined absorption, such as asymmetrically functionalized rotors can be directly scaled down because they function under blanket irradiation. Ultraviolet and e-beam lithography can be used to produce micro- and nanoscale rotors, which can be mounted onto axles and incorporated into microfluidics, potentially acting as solar powered pumps.

Scaling down composites to produce controlled linear motion on the nanoscale presents new challenges, as the spatially defined irradiation necessary to produce controlled motion on the centimeter scale is no longer viable. To circumvent this difficulty we propose to engineer composites with spatially discrete regions of distinct absorbers that are tailored to selectively absorb specific wavelengths of light. Precise placement of dissimilar absorbers will allow blanket irradiation of the objects with different wavelengths of light to produce different responses. For instance, we will use Au and Ag nanoparticles tuned to absorb 532 nm and 785 nm, respectively. By placing these absorbers in specific regions of an object (Figure 3-15a), we can get a wavelength specific response. For example, blanket irradiation with 532 nm, green light, will selectively heat the yellow region, resulting in forward, right turning motion (Figure 3-15b). On the other hand, blanket irradiation with 785 nm light (red light), will selectively heat the blue region, resulting in forward left turning motion, and irradiation with white light will give forward motion. In this manner, blanket irradiation can be used to produce controlled motion of objects of any size. Such materials can also be incorporated into rotors, resulting in wavelength dictated clockwise or counterclockwise motion, as depicted in Figure 3-15c.

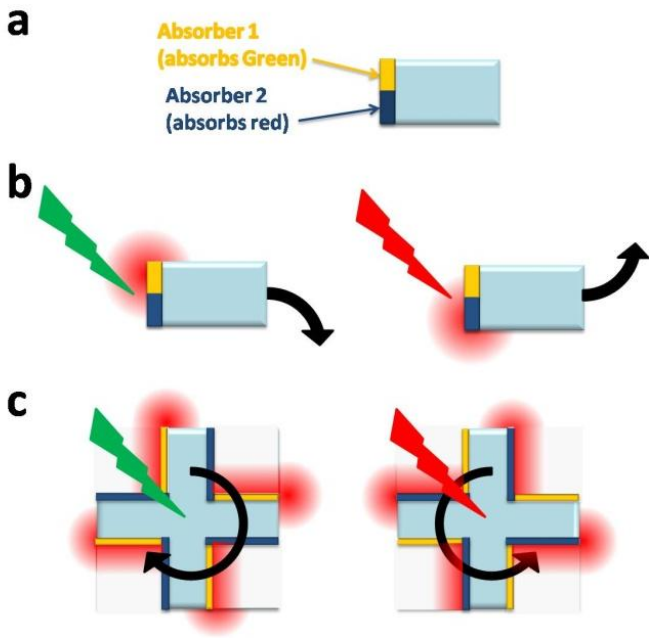

Figure 3-15. To control motion on the micro/nanoscale it is necessary to use differential absorption of light. Two different absorbers are selectively patterned onto an object (a) to produce controlled linear motion. Red regions indicate heated area. (b) Blanket irradiation of the entire region with green light

selectively heats the orange material, resulting in right turning motion. Irradiation with red light results in left turning motion. Analogously, rotors (c) can be controlled to produce either clockwise or counter-clockwise motion.

Controlled motion on these length scales has applications in lab-on-a-chip devices, microfluidic water pumps, roving sensors, and nanoscopic cargo carriers.[31] For instance, one could use this premise of differential absorption to produce composites that can be controlled to pick up an object, carry it to a second location and drop it off. These extensions of the current work show promise for developing a technological framework with which one can produce innovative solutions to a variety of problems by converting light directly into motion.

---

1 Bush, J. W. M.; Hu, D. L. *Annul. Rev. Fluid Mech.* **2006,** *38,* 339-369.

2 (Photovoltaic) Hagfeldt, A.; Gratzel, M. *Acct. Chem. Res.* **2000,** *5,* 269-277. (Solar Thermal) Cuomo, J. J.; Ziegler, J. F.; Woodall, J. M. *Appl. Phys. Lett.* **1975,** *26,* 557-559. (Bio-fuel) St. Clair, S.; Hillier, J.; Smith, P. *Biomass & Bioenergy* **2008,** *32,* 442-452. (Water splitting) Khan, S.; Al-Shahry, M.; Ingler, W.B. *Science,* **2002,** *297,* 2243-2245.

3 Basic Research Needs for Solar Energy Utilization, Report of the BES Workshop on Solar Energy Utilization April 18-21, 2005.

4 Gratzel, M. *Phil. Trans. R. Soc. A.* **2007,** *365,* 993-1005. Burke, A. *J. Power Sources* **2000,** *91*, 37-50.

5 Forward, R. L. *J. Spacecraft* **1990,** *27,* 411-416.

6 Ashkin, A. *Proc. Natl. Acad. Sci.* **1997,** *94*, 4853-4860.

7 (a) Denninghoff, D. J.; Starman, L. A.; Kladitis, P. E.; Perry, C. *IEEE Circuits and Systems 48th Midwest Symposium* **2005,** *1*, 367-370. (b) Crookes, W. *Phil. Trans. Roy. Soc. Of London* **1874,** *164*, 501-527.

8 Rybalko, S.; Magome, N.; Yoshikawa, K. *Phys. Rev. E.* **2004,** *70,* 046301.

9 (a) Brzoska, J. B.; Brochard-Wyart, F.; Rondelez, F. *Langmuir*, **1993,** *9,* 2220-2224. Brochard, F. *Langmuir* **1989,** *5,* 432-438. (b) Farahi, R.H.; Passian, A.; Zahrai, S.; Lereu, A.L.; Ferrell, T.L.; Thundat, T. *Ultramicroscopy* **2006,** *106,* 815-821.

10 Baroud, C. N.; de Saint Vincent, M. R.; Delville, J. P. *Lab Chip* **2007,** *7*, 1029-1033.

11 Schildknecht, H. *Angew. Chem. Int. Ed. Engl.* **1976,** *15,* 214-222.

12 Nakata, S.; Kirisaka, J.; Arima, Y.; Ishii, T. *J. Phys. Chem. B.* **2006,** *110,* 21131-21134.

13 Bush, J. W. M.; Hu, D. L. *Annu. Rev. Fluid Mech.* **2006,** *38,* 339-369.

14 (a) Kline, T. R.; Paxton, W. F.; Mallouk, T. E.; Sen, A. Catalytic, *Angew. Chem. Int. Ed.* **2005,** *44,* 744-746. (b) Ismagilov, R. F.; Schwartz, A.; Bowden, N.; Whitesides, G. M. *Angew, Chem. Int. Ed.* **2002,** *41,* 652-654.

15 5 wt% MWNT produce a similar response to VANT absorber.

16 Yang, Z. P.; Ci, L.; Bur, J. A.; Lin, S. Y.; Ajayan, P. M. *Nano Lett.* **2008,** *8*, 446-451.

17 Hata, K.; Futaba, D. N.; Mizuno, K.; Namai, T.; Yumura, N.; Iijima, S. *Science* **2004,** *19*, 1362-1364.

18 In principle, any laser absorbed by the composite should be effective.

19 (a) Shapere, A.; Wilczek, F. *Phys. Rev. Lett.* **1987,** *58*, 2051-2054. (b) Chang, S. T.; Paunov, V. N.; Petsev, D. N.; Velev, O. D. *Nat. Mater.* **2007,** *6*, 235-240.

20 Forces were derived from location vs. time, as discussed in the *Force Quantification* section.

21 Luo C.; Luo, H.; Li, X.; Liu, *J. Micromech. Microeng.* **2008,** *18*, 1-6.

22 Rasband, W.S., ImageJ, U. S. National Institutes of Health, Bethesda, Maryland, USA, http://rsb.info.nih.gov/ij/, 1997-2009.

23 Abramoff, M.D.; Magelhaes, P.J.; Ram S.J. *Biophotonics Int.* **2004,** *11*, 36-42.

24 Composites larger than the spot size of the laser were used to allow absorption to be focused solely on the back face. This resulted in larger forces being produced compared to the previous examples, where the spot size was larger than the back face of the composites.

25 Gugliotti, M.; Baptista, M. S.; Politi, M. J. *Langmuir* **2002,** *18*, 9792-9798.

26 We chose water, IPA, and DMF because of the broad range of temperature dependence of surface tension and heat capacity.

27 As surface tension forces scale linearly with contact length proportionally larger or smaller objects should be moved with equal efficiency.

28 Bowden, N. B.; Terfort, A.; Carbeck, J.; Whitesides, G. M. *Science*. **1997,** *276*, 233-235.

29 Bowden, N. B.; Weck, M.; Choi, I. S.; Whitesides, G. M. *Acc. Chem. Res.* **2001,** *34*, 231-238.

30 Yang, Z. P.; Ci, L.; Bur, J. A.; Lin, S. Y.; Ajayan, P. M. *Nano Lett.* **2008,** *8*, 446-451.

31 Sundararajan, S.; Lammert, P. E.; Zudans, A. W.; Crespi, V. H.; Sen, A. *Nano. Lett.* **2008,** *8*, 1271-1276.

Chapter 4:

Phototriggerable Microcapsules

The ability for optothermal methods to remotely manipulate system variables has attractive implications for chemical reactions. Two methods standout that would allow optothermal techniques to modulate chemical reactions: either through temperature induced reaction rate control or via an alternative system variable that could initiate or hinder a reaction. We found the idea of an optothermally initiated reaction to be appealing as it could be used to spatially selectively and remotely initiate a complex response even within a confined system. The ideal system would have a negligible background reaction rate and a fast reaction after optothermal initiation. To obtain a negligible background rate we decided to physically isolate a reaction component in an impermeable, liquid-filled microcapsule (MC). Incorporation of an absorbing material inside the MCs affords an optothermal trigger that functions through a heat induced increase in internal pressure to burst the MC.[1] By using a heat/pressure based triggering mechanism the only requirement is that the encapsulated component be thermally stable – providing a wide range of potential substrates.

While liquid filled microcapsules[2] are widespread with applications as varied as carbonless copy paper, agrochemicals, or self-healing polymers,[3] remote triggering of content release is not common. Langer et al. have described the remote release of chemicals from a microchip by dissolution of a polymer membrane triggered by application of an electric potential.[4] More commonly, release is induced through crushing or the application of other forms of mechanical stress.[1-2] We have developed remotely triggerable liquid-filled, free-flowing solid microcapsules (MCs) with impermeable shell walls that enable the coexistence of otherwise incompatible chemical species in a single container until their reaction is desired.

Triggering the release of the contents of MCs by light is attractive as light can easily address a small object or blanket an entire surface. To achieve this goal we have designed remotely triggered MCs in which the encapsulated liquid contains an optothermally active species, such as carbon nanotubes (CNTs), which can rapidly heat up the liquid content when irradiated. Irradiation of an MC would then trigger a rupture mechanism involving an increase in internal pressure. In early light initiated work, Masuhara et. al., reported the escape of toluene/pyrene droplets from an optically trapped melamine/formaldehyde microcapsule when irradiated with a second laser that caused ablation of the capsule wall.[5] Similarly, Au or Ag nanoparticles have more recently been used as optothermal triggers for the breakdown of semi-permeable polyelectrolyte membranes.[6]

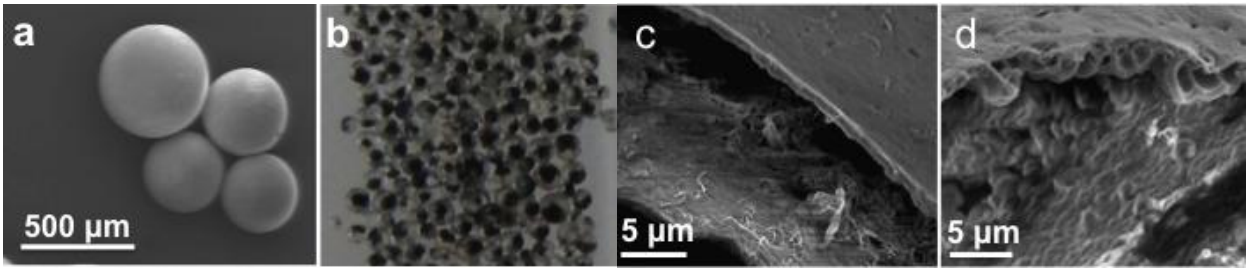

Figure 4-17. Toluene filled polyamide microcapsules containing 1 wt% CNTs. (a) Scanning electron micrograph, and (b) Optical image of filled MCs. (c,d) Scanning electron micrographs of crushed MCs. CNTs (white bundles) are visible in the interior and on the exterior of the capsule (c) and incorporated into the wall (d). Smaller hollow capsules also adhere to the interior face of the capsules (d) with some open particles found on the edge of the upper wall.

CNTs were selected as the optothermal-triggering element because they absorb light across the entire spectrum[7] and efficiently convert the absorbed light into heat. Unfortunately, CNTs are poorly soluble in most organic solvents; therefore, it was imperative to identify a robust microencapsulation method that not only prevented the partitioning of the CNTs into the continuous phase, but also permitted the isolation of free-flowing solids. The interfacial polymerization of triamines and di- or triacid chlorides in an oil-in-water emulsion, a technique thoroughly studied by Mathowitz and Cohen,[8] was found to be well suited for these purposes. CNT functionalization was also investigated for encapsulation but was found to be unnecessary when using the polyamide microencapsulation.

4.1 Microencapsulation

A typical encapsulation procedure begins with the addition of 3 mL of a 0.4 wt.% polyvinyl alcohol (PVA; 87-89% hydrolyzed) solution in water to a 20 mL glass vial equipped with a 1/2" x 1/8" magnetic stir bar. To a separate 8 mL glass vial was added multiwall CNTs (1 mg), terephthaloyl chloride (45 mg, 0.22 mmol) or trimesoyl chloride (55 mg, 0.21 mmol) and 1 g of solvent (toluene, phenylacetylene, or chloroform). The mixture was sonicated (~5 min) and then added to the PVA solution with magnetic stirring. Stirring (500-1500 rpm; IKA stir plate setting) was continued for an additional 0.5-1 min, and then diethylenetriamine (DETA; 650 µL, 5.98 mmol, ~27 equiv.) in 1 mL distilled water was added dropwise over approximately 0.5-1 min. After the addition of DETA, the stirring was stopped, and the MCs were allowed to set for 1.5-24 h (at times, small amounts wispy white polymer material formed, which was physically removed). Membrane formation around the oil droplets was nearly instantaneous but the particles were allowed to set to ensure that solid-walled and impermeable MCs were obtained. A longer setting period is not detrimental, but rather, ensures the likelihood that free-flowing particles will be obtained. Isolation by filtration afforded free-flowing, liquid-filled MCs (Figure 4-1a,b) with diameters of 100-1000 µm in yields ranging from 80-95%. Shell thickness was determined to be ~1 µm by SEM (Figure 4-1c, d), and the liquid fill content for toluene-filled capsules was determined to be ~ 95 wt%. Optical images (Figure 4-1b) reveal that the majority of the CNTs are located inside the MCs. Further SEM analysis of crushed particles showed that some of the CNTs are embedded in the shell material. Small capsules, with diameters less than 5 µm, which are also formed during the microencapsulation process, may become incorporated into the interior of the larger MCs (Figure 4-1d). A variety of encapsulated liquids were investigated and optical images are shown in Figure 4-2.

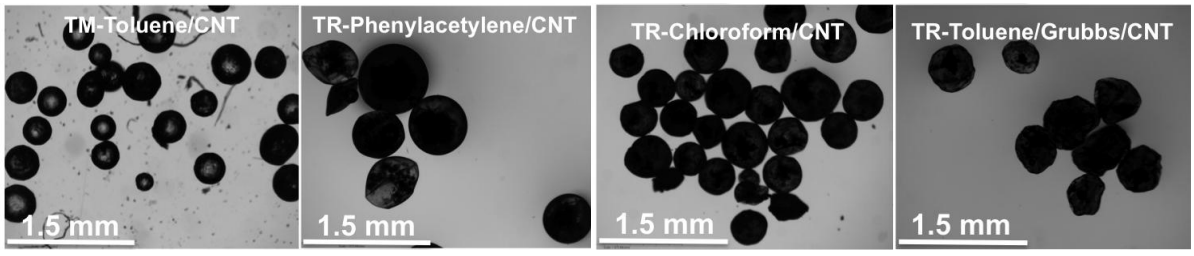

Figure 4-2. Black and white optical images of different MCs prepared under the general conditions. Images were taken in oil or on a thin film of PDMS (top left).

4.2 Microcapsule Characterization

Average MC size can be controlled with emulsification stir rate (Figures 4-3 and 4-4). If a narrow distribution of a particular MC diameter is desired, then the isolated MCs can be sieved through standard meshes. The average size appears to be fixed upon the addition of DETA. For the purposes of this work it was of interest to have a wide-range of MC diameters, and the influence of emulsification time and stir rate on the MC size distribution was not thoroughly investigated. The synthesis, characterization, and properties of polyamide walled microcapsules are well documented, and the reader is directed to a series of papers[9] by Mathowitz and Cohen if more information is desired.

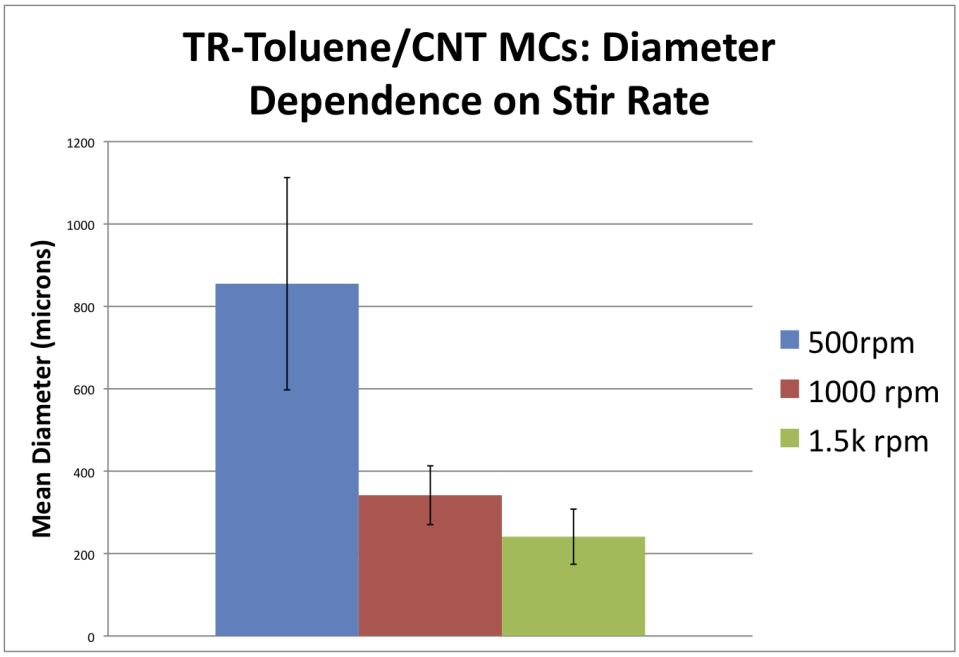

Figure 4-3. The mean diameter and standard deviation (error bars) for TR-toluene/CNT MCs as a function of stir rate. For each case, the emulsion was stirred for 30 s before the addition of DETA.

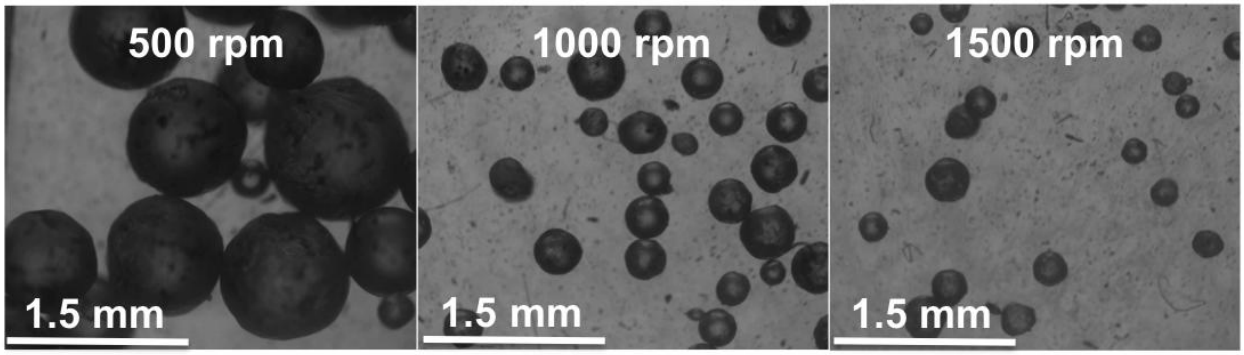

Figure 4-4. Optical comparison of TR-Toluene/CNT MCs prepared at three different stirring rates. Images were taken on thin films of PDMS.

Physical crushing of the MCs produced an audible pop and resulted in ejection of the encapsulated liquid, demonstrating the good physical barrier properties of the shell-wall. Notably, no significant decrease in fill content of the MCs was apparent after standing in air for over 2 months. This was determined by placing a known amount of TR-toluene/CNT MCs at various time points in a tarred vial, physically crushing the microcapsules, and removing the volatile liquid fraction under reduced pressure (Table 1).

Table 4-1. Comparison of Liquid Fill Content of TR-toluene/CNT MCs with Time

	1 Days After Isolation	30 Days After Isolation	64 Days After Isolation
Tarred Weight	115.3 mg, 161.9 mg	93.1 mg	110 mg
Weight after removal of volatiles	5.3 mg, 6.5 mg	3.9 mg	4 mg
Liquid Fill Content	95%, 96%	96%	96%

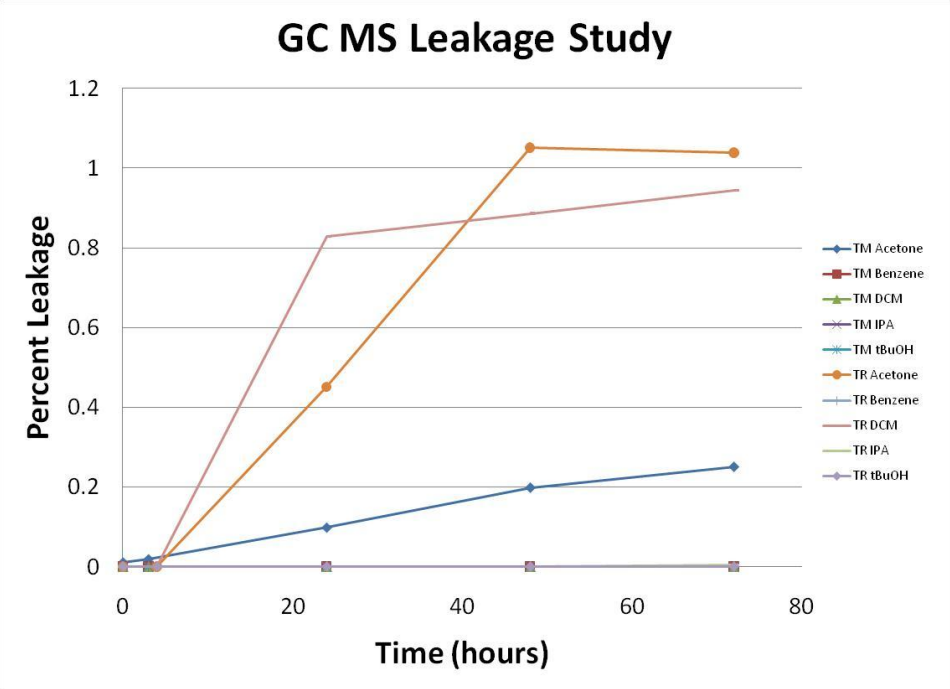

Figure 4-5. Leakage study of phenylacetylene filled particles monitored by GC-MS. Increasing cross-linking density by incorporating TM decreased permeability. Substantial leakage was observed for TR-MCs in acetone and DCM. TM-MCs only showed leakage in acetone.

Furthermore, leakage studies with encapsulated phenylacetylene revealed that little to none of the liquid content escaped when the MCs were immersed in solvents that do not swell the cross-linked polyamide shell wall such as *t*-butanol, benzene, hexanes, and dichloromethane . Specifically, phenylacetylene/CNT MCs made using either terephthaloyl chloride (TR) or trimesoyl chloride (TM) were placed in GC-MS vials containing dodecane (1 µL) as an internal standard and solvent (acetone, benzene, hexanes, *t*-BuOH, isopropyl alcohol, or dichloromethane). The appearance of phenylacetylene was monitored periodically via GC-MS. For MCs made with TR, no phenylacetylene was detected for isopropyl alcohol, benzene, hexanes, and *t*-BuOH over the monitored period (72 h); significant leakage occurred in acetone and DCM (Figure 4-5). Increased cross-linking, as a result of incorporation of TM instead of TR reduced or eliminated leakage except in swelling solvents such as DMF, THF, and methanol, which result in considerable leakage almost immediately after immersion (data not shown).

4.3 Optothermal Release Studies

Having confirmed negligible leakage of the liquid contents under a broad range of conditions, we next tested if liquid release could be optically triggered with a near-IR laser.[10] Indeed, as depicted in Figure 4-6, encapsulated toluene can be optothermally released via laser irradiation (785 nm, 450 mW diode laser) in air. Bursting of the MCs occurred within 0.02 s, and observation of the process under an optical microscope revealed that swelling occurred immediately prior to bursting (Figure 4-6a-c). For comparison, heating of toluene filled MCs in a standard melting point capillary resulted in considerable swelling and bursting at ~171 ˚C, which correlates to an internal pressure of ~4.5 atm.[11] Importantly, the MCs can also be optothermally ruptured by IR laser irradiation when immersed in liquids such as water or alcohols, and a release efficiency of >95% was obtained for phenylacetylene MCs.

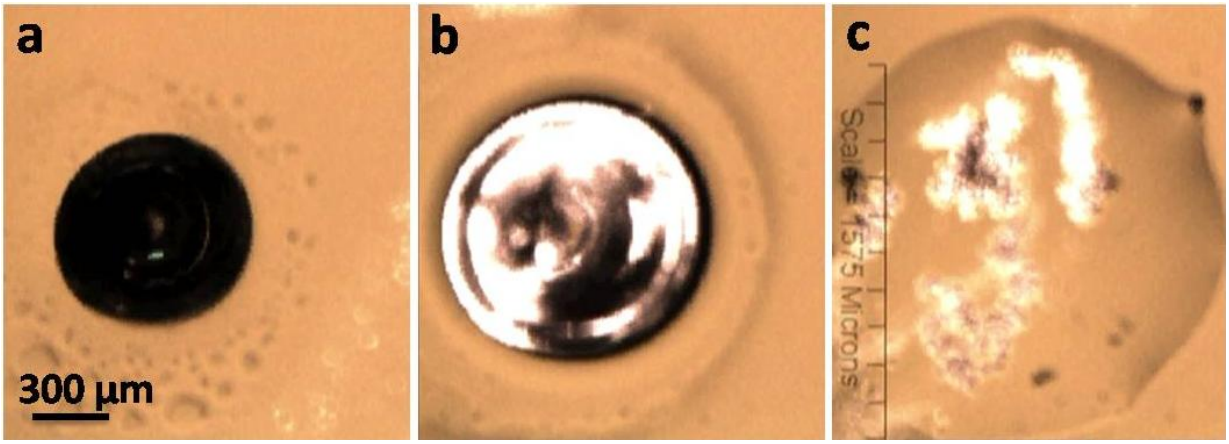

Figure 4-6. Optical micrographs of a nanotube filled microcapsule prior to irradiation (a), during irradiation (b), and after bursting (c). Swelling is evident during irradiation (b), resulting in an increase in internal volume on the order of 2.5 times.

Release efficiency was determined by immersing two phenylacetylene/CNT MCs in *t*-BuOH in a quartz cuvette. A single MC was burst with a laser and the absorbance at 270 nm was monitored by UV-Vis spectroscopy. After one hour, the burst particle was physically crushed and any further release was monitored by UV-Vis. The process was repeated with the second MC. This was performed for both TR and TM based phenylacetylene/CNT MCs and the release efficiency was stated as the percent released from laser bursting compared to that from complete crushing (Figures 4-7 and 4-8).

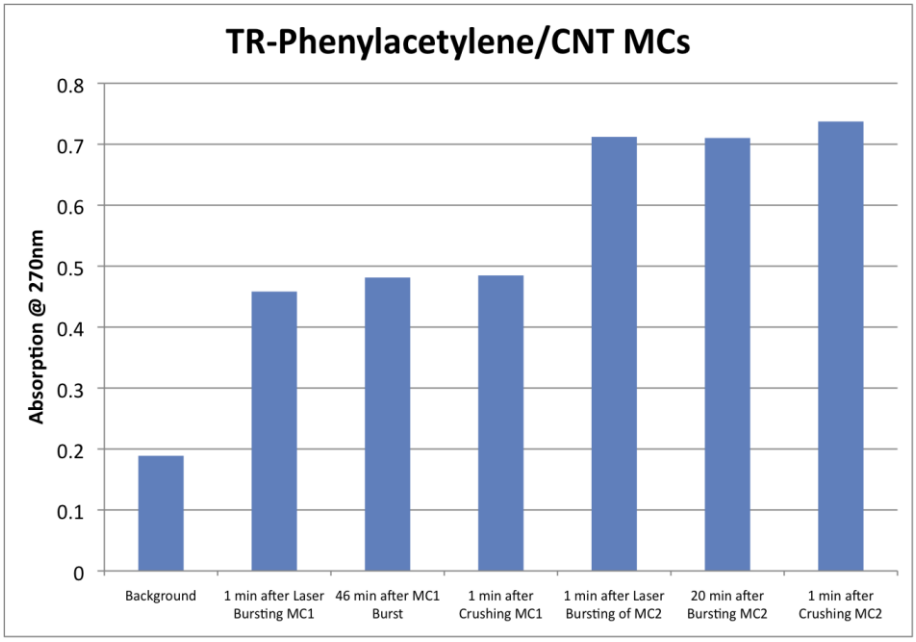

Figure 4-7. Laser induced release of phenylacetylene from TR-MCs in tBuOH as monitored by UV-Vis absorption.

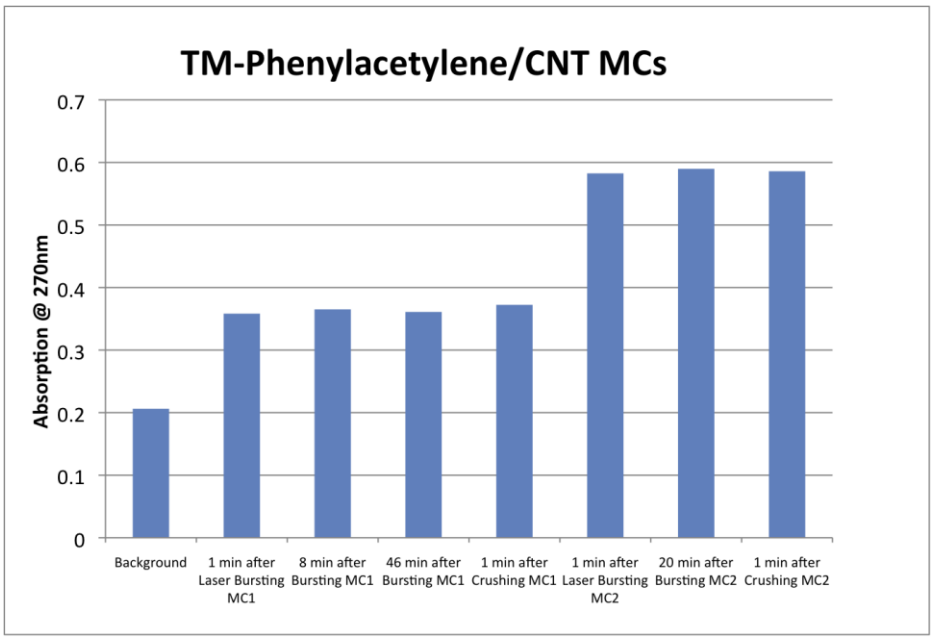

Figure 4-8. Laser induced release of phenylacetylene from TM-MCs in tBuOH.

4.4 Chemical Isolation and Release

4.4a Click Reaction

To demonstrate the concept that mutually reactive materials can be stored in intimate proximity and remotely released "on demand," phototriggerable phenylacetylene MCs were immersed in a solution containing benzyl azide under highly reactive click conditions.[12] The click reaction is a useful test system because when contacted in the presence of Cu (I), phenylacetylene and benzyl azide react rapidly to quantitatively give the corresponding triazole. To monitor the stability, chemical isolation, and the optothermal release ability of the MCs the benzyl azide concentration in the reaction vial was monitored by Gas Chromatography–Mass Spectrometry (GC-MS). Figure 4-9a shows the phenylacetylene capsules coexisting with the solution of azide and copper catalyst until irradiated after 24h. Laser-induced bursting of the MCs resulted in rapid consumption of benzyl azide with complete conversion within 1h. The spatial resolution of the laser also enabled the successive triggering of several MCs, resulting in the controlled and stepwise consumption of the starting material (Figure 4-9b). These results successfully demonstrate the ability of CNT filled MCs to isolate chemically reactive species and remotely trigger their release "on demand."

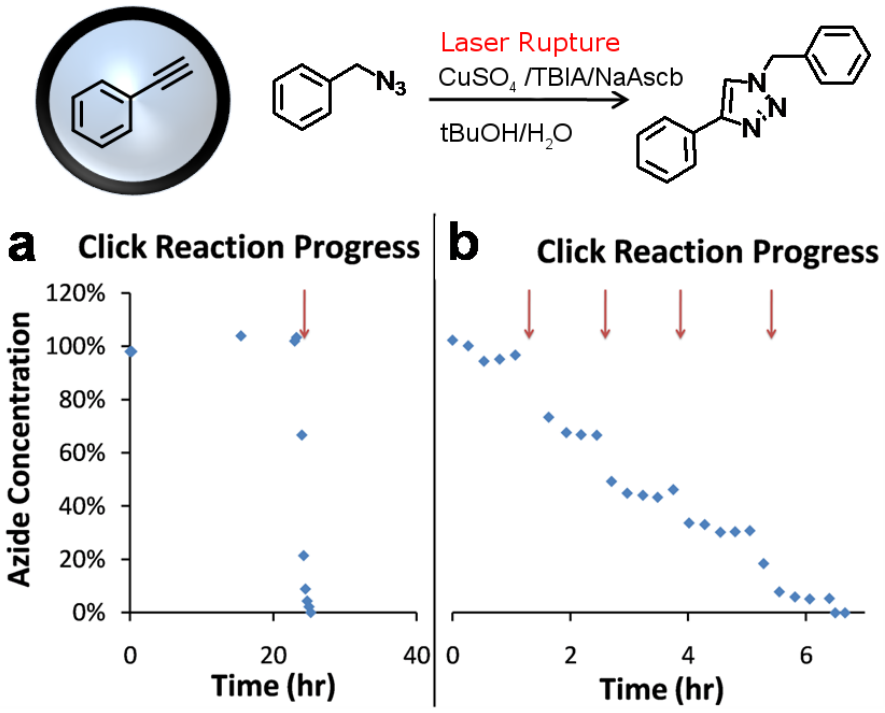

Figure 4-9. Click reaction progress as monitored by GC-MS via the consumption of benzyl azide. Red arrows indicate points of laser rupture. (a) Single shot release of multiple MCs to completely consume all of the azide. (b) Selective rupture of individual particles among a group, showing the ability to trigger the reaction in a stepwise fashion.

4.4b Catalyst Encapsulation – Controlled Polymerizations

As another demonstration of stable isolation and remote reaction initiation, we explored the "on-demand" laser induced polymerization of dicyclopentadiene (DCPD) via ring opening metathesis polymerization (ROMP). To this end, Grubb's second generation catalyst was encapsulated in toluene. Specifically, a solution of 2nd generation Grubb's Catalyst (5 wt. % in toluene) was encapsulated by the general procedure described above using terphthaloyl chloride with the following modifications: (1) the PVA, DETA, and organic solutions were evacuated and refilled with N_2 (without freezing) and MC formation was carried out under a nitrogen atmosphere, and (2) the MCs were isolated after a 2h set period. Significantly longer set periods can result in MCs that are inactive for polymerization, while significantly shorter set periods can produce MCs without the ideal free-flowing characteristics. If the MCs are not free-flowing (e.g. agglomerated bundles of MCs), there can be an increased background rate of DCPD curing presumably due to leakage of the catalyst.

These MCs can be dispersed in neat DCPD (1 mg MC/100 mg DCPD) for weeks without a noticeable increase in viscosity. In contrast, laser bursting of the capsules resulted in the polymerization of DCPD and gelling within minutes (Figure 4-10). This example further highlights the large "on-off" characteristics that can be obtained with these responsive MCs. The fact that the encapsulated small molecule catalyst maintains significant activity is notable, considering that free amines were used for encapsulation and that significant heating is necessary for release.

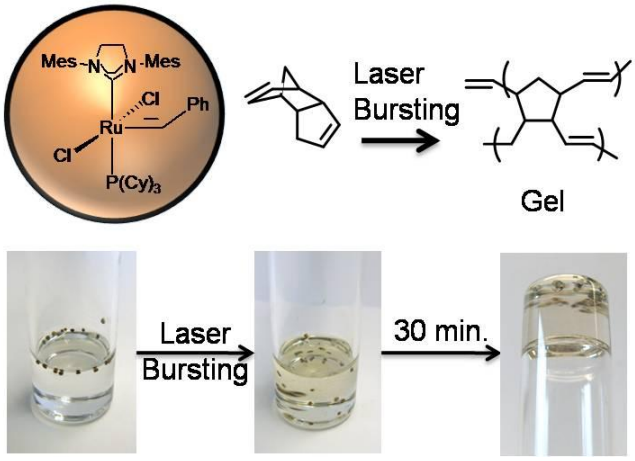

Figure 4-10. Ring opening metathesis polymerization of DCPD using encapsulated Grubbs Catalyst. Images of MCs in DCPD (left), shortly after bursting (center), and after reaction (right).

4.5 Wavelength Specific Bursting

To expand the scope of this technology we explored the capabilities of different light absorbing materials to induce MC rupture. Encapsulation of nanotubes, conjugated polymers, dyes and pigments have all shown optothermal bursting (*vide infra*). The capability to use a variety of absorbers opens up the possibility of selecting the MCs to burst based on the wavelength of laser light used. This extension allows application toward more complicated

reactions with multiple components, enabling fine control over multiple potential reactions and products within a single mixture. The properties of the product could be dictated by the wavelengths of light and order in which the MCs are burst. This technology has application in complex reactions on demand, off-set printing, and other remotely triggered applications. A potential reaction scheme is depicted in Figure 4-11. In this example, two separate potential reactions can be controlled depending on the wavelength of irradiation. Toward this goal, we have prepared wavelength specific MCs that can be selectively burst with either 785 nm or 532 nm light. Encapsulation was performed by roughly the same procedure as with CNT absorbers.

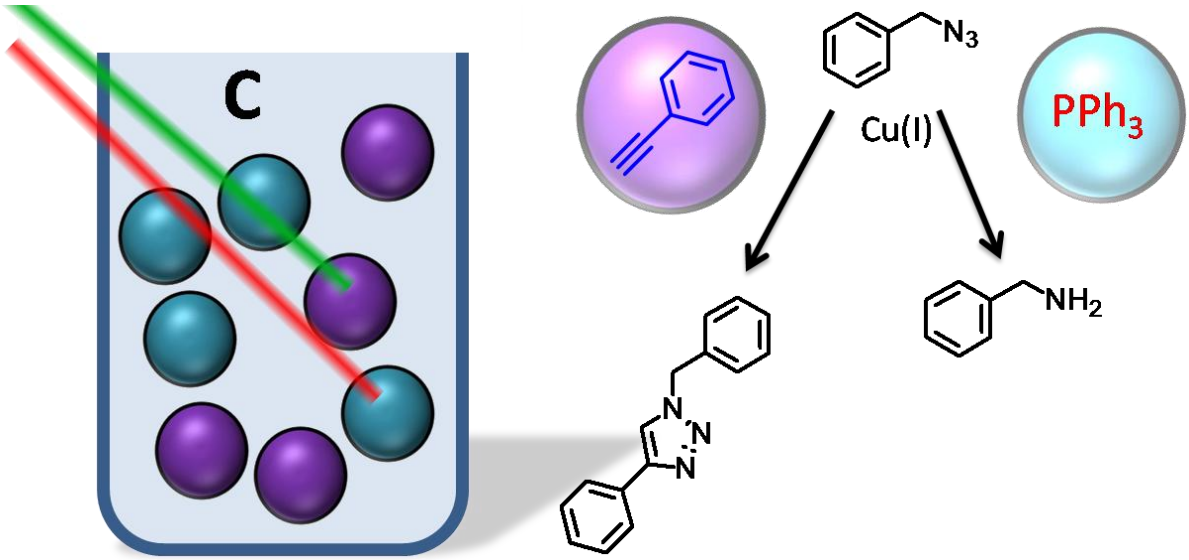

Figure 4-11. A potential reaction scheme utilizing two types of MCs sensitive to different wavelength light. The purple MCs efficiently absorb green light and contain phenyl acetylene. The blue MCs absorb red light and contain triphenyl phosphine. When placed in a solution of benzylazide and Cu(I) no reaction occurs until irradiation. If irradiated with green light the click reaction proceeds and the triazole is produced. If irradiated with red light, the azide is reduced and the amine is formed.

To test the laser power necessary to burst the microcapsules, a fiber coupled laser and a camera with zoom lens were mounted and focused on an xyz stage, as shown in Figure 4-12. The microcapsules were placed on a glass slide or thin slice of PDMS, to keep the MCs stationary during experiments. For testing, two modes were used, a slow ramping of the laser power and constant laser power. The two lasers used were rated as 400 mW 785 nm and 1000 mW 532 nm fiber coupled diode lasers.

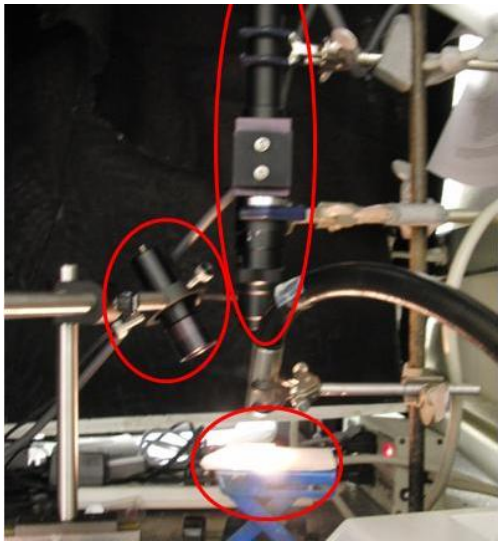

Figure 4-12. Microcapsule bursting setup. Focusing lens for laser is in left circle. Camera and magnifying mount is in the upper oval. The lighted stage is in the lower oval.

4.5a Visible Light Induced Bursting

For visible light absorbing MCs (vis-MCs), we chose to focus on the conjugated polymer poly-3-hexylthiophene (P3HT) as the absorber. P3HT is highly soluble in organic solvents and absorbs well at 532 nm and poorly at 785 nm. Encapsulation of P3HT in toluene produces liquid filled, free flowing MCs as shown in Figure 4-13. Consistent with poor absorption in the nIR, P3HT filled microcapsules would not rupture under 785 nm laser irradiation, but readily burst under 532 nm irradiation (specific bursting powers will be discussed in *Tuning Laser Bursting Power for Differential Absorption*).

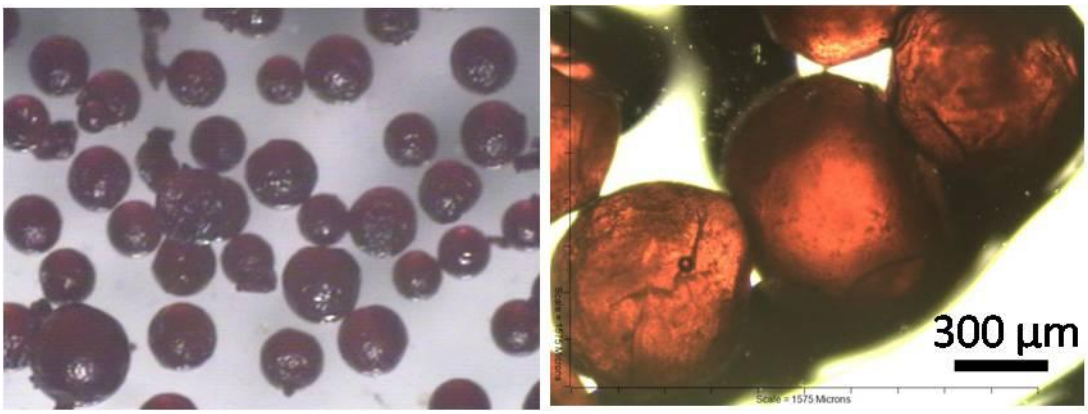

Figure 4-13. Free flowing P3HT filled MCs.

4.5b Near Infrared Induced Bursting

For nIR induced absorbing MCs (nIR-MCs), we investigated a variety of light absorbers from Epolin Inc. and Sigma Aldrich: IR783 (Sigma Aldrich), and Epolight 3030, 3036, 5548, and 9194. Solution phase absorption spectra of the dyes are shown in Figure 4-14. Unfortunately, unlike P3HT, nIR absorbers tend to absorb both in the nIR and at higher energies into the visible. This makes nIR-MCs susceptible to bursting by visible laser light. As an initial evaluation, we compared the solution phase absorption of the dyes at 785 nm and 532 nm (inset Figure 4-14). All dyes have an absorption ratio at 785 nm: 532 nm greater than seven. IR783 had a substantially higher absorption ratio (~300), but was not stable to encapsulation conditions.[13] We encapsulated the four Epolight dyes in toluene filled MCs (Figure 4-15). There was considerable variability in the suitability of the as-produced microcapsules. Epolight 9194 and 3036 produced free-flowing, liquid-filled nIR-MCs. Epolight 3036 and 5548 interfered with the encapsulation procedure and produced sticky and empty nIR-MCs, respectively. The nIR-MCs were then tested for laser bursting. In general, all nIR-MCs could be ruptured by both the 785 nm laser and the 532 nm laser. This is consistent with their appreciable absorption at both wavelengths as seen in the absorption spectra.

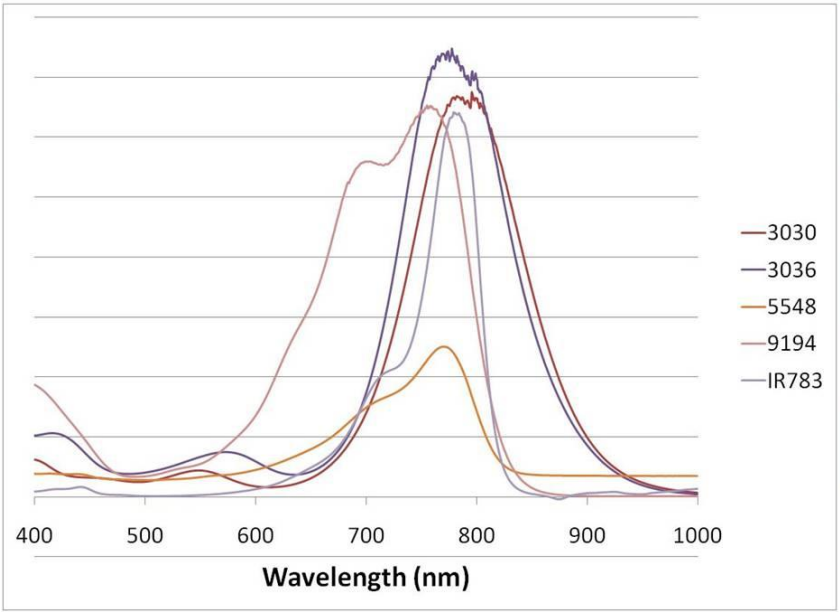

	Ratio (785:532nm)
3030	17.3
3036	13.1
5548	7.4
9194	10.8
IR783	303

Figure 4-14. Comparison of various n IR absorbing dyes from Epolin Inc. and Sigma Aldrich. The table shows the ratio of absorption at 785 nm to 532 nm.

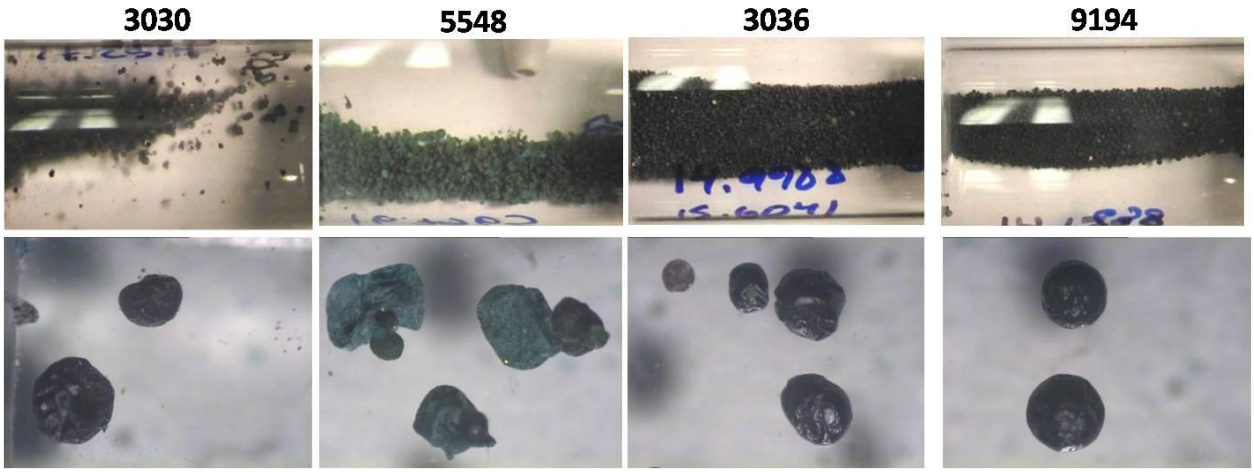

Figure 4-15. Optical images of microcapsules with four different nIR absorbing dyes obtained from Epolin, Inc. Epolight 9194 and 3035 produced free-flowing, burstable, liquid-filled microcapsules and were used for further testing.

4.5c Tuning Laser Bursting Power for Differential Bursting

The ability to selectively address nIR-MCs versus vis-MCs (and vice versa) would significantly broaden potential chemical release scenarios. Ideally, a single wavelength at any power would burst only the associated type of MC but, unfortunately, the nIR-MCs can also burst by higher energy light. To access selective bursting with the chosen absorbers careful tuning of the bursting properties was necessary. We hypothesized that the dye concentration would be a significant factor. To investigate this idea, we produced vis-MCs and nIR-MCs with varying dye concentrations. As predicted, P3HT filled microcapsules (Figure 4-16, Table 2) showed absorber concentration dependence: under slowly ramped laser power conditions 30 mg/ml P3HT vis-MCs burst at 188 ±4 mW (error is expressed as standard deviation) and 10 mg/mL P3HT vis-MCs burst at 297 ±73 mW. This ability to tune the conditions necessary for bursting the MCs should allow for increased wavelength selectivity.

As with the vis-MCs, the dye concentration influenced the power necessary for nIR-MCs bursting (Figure 4-16, Table 4-2). For Epolight 9194 nIR-MCs the burst power at 785 nm ranged in the following way: unburstable at 0.1 mg/mL; 380 ±30mW at 1 mg/mL; 244 ±17mW at 10 mg/mL. This trend was found to plateau at concentrations above 10 mg/mL for Epolight 9194. A similar trend was observed for 9194-nIR-MCs exposed to 532 nm irradiation. This is presumably a result of the dye being present in sufficient amounts to completely absorb incident light at these intensities and thus the addition of more dye does not result in great absorption or heating. 3036 nIR-MCs were also tested (Figure 4-16, Table 4-2), though their concentration dependence was not as obvious. Interestingly, the power necessary to burst nIR-MCs was similar at 532 nm and 785 nm.

Table 4-2. Concentration Dependence of Laser Power Necessary for Bursting

Vis-MCs (P3HT)	30 mg/mL	10 mg/mL		
Power (785 nm)	No burst	No burst		
Power (532 nm)	188 ±4 mW	297 ±73 mW		
nIR-MCs (9194)	23 mg/mL	10 mg/mL	1mg/mL	0.1 mg/mL
Power (785 nm)	224 ±31 mW	244 ±17 mW	383 ±30 mW	No burst
Power (532 nm)	243 ±45 mW	223 ±25 mW	401 ±30 mW	No burst
nIR-MCs (3036)	14 mg/mL	7 mg/mL		
Power (785 nm)	159 ±87 mW	193 ±50 mW		
Power (532 nm)	251 ±37 mW	218 ±64 mW		

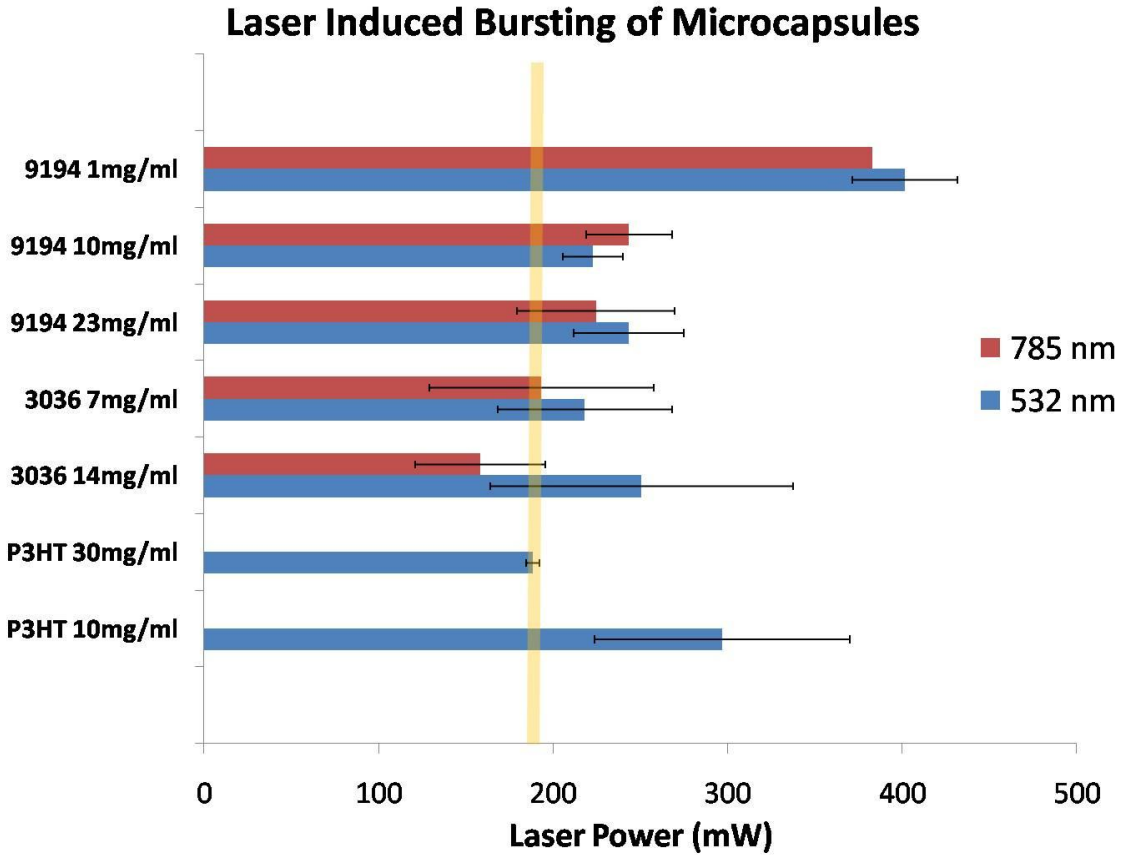

Figure 4-16. Laser induced bursting of microcapsules comparing various absorbers and the laser power and wavelength necessary to burst them. Microcapsules were all prepared under similar conditions. The orange line indicates the minimum power at 532 nm required to burst P3HT vis-MCs. For selectivity to occur, all nIR-MCs must not burst below this power at 532 nm.

For all nIR-MCs, a relatively broad range of bursting powers was observed. In an attempt to decrease this variability, we investigated the influence of the MC diameter on the bursting power. To decrease the diameter distribution we sieved the microcapsules through increasingly small wire meshes (Figure 4-17). Unfortunately, no correlation between diameter and bursting power (Figure 4-17 bottom) was observed. Further study of encapsulation conditions is necessary to decrease this variability.

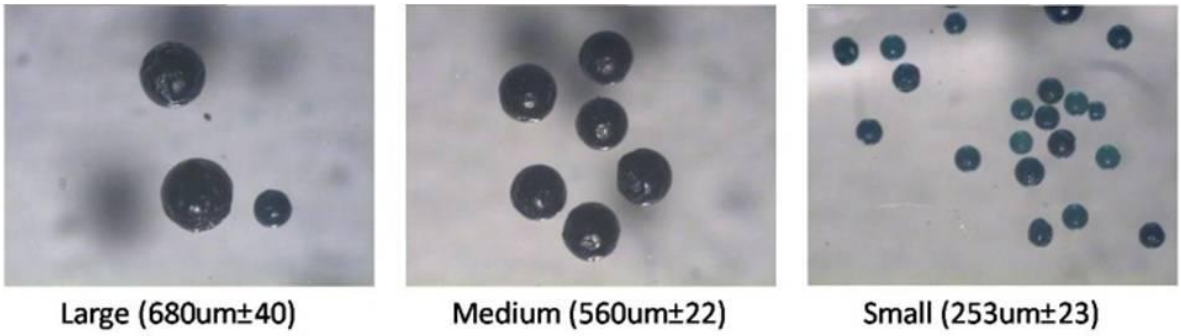

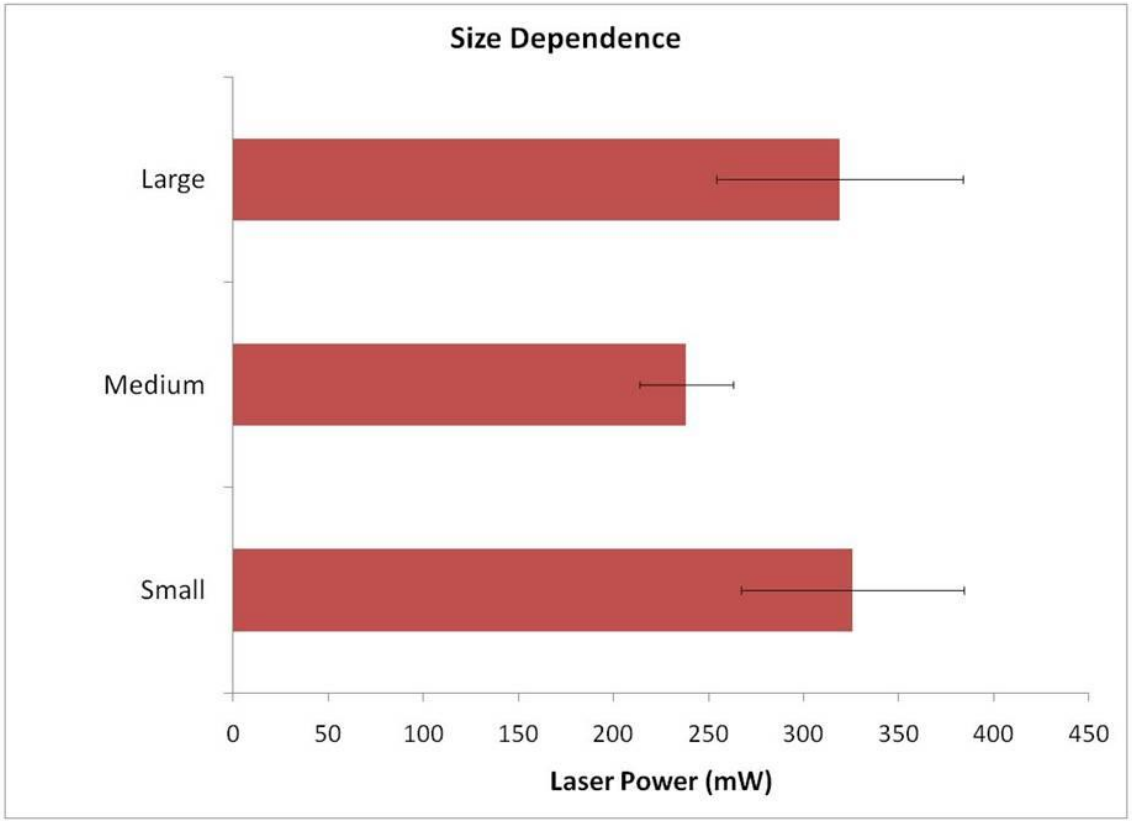

Figure 4-17. Free flowing, toluene-9194 nIR-MCs produced under standard conditions at 1000 rpm. MCs are passed through two sieves to isolate large, medium and small microcapsules. Laser bursting was tested at 785 nm and no diameter dependence was observed.

To obtain wavelength specific MC bursting it must be more difficult to burst nIR-MCs then vis-MCs using a visible laser. The orange line in Figure 4-16 indicates the minimum power necessary to burst high concentration P3HT vis-MCs at 532 nm (188 ±4 mW). For wavelength

selectivity, nIR-MCs must be burst by 532 nm light at higher intensities. As is evident in Figure 4-16, all 9194 nIR-MCs require more power at 532 nm light (are to the right of the orange line) and thus would be suitable to for selective bursting studies with 30 mg/mL P3HT MCs. This result was extended by mixing appropriate nIR-MCs and vis-MCs and exposing them to the appropriate power conditions. As expected, under controlled 532 nm exposure only the vis-MCs ruptured. Under 785 nm exposure only nIR-MCs burst. By careful selection of the concentration of absorptive material encapsulated, we were able to impart wavelength selectivity to our phototriggerable MCs. Before applications of wavelength specific MCs are sought, it will be worthwhile to further increase the 785/532 nm differential absorption of the nIR-MCs. This may be feasible by further studying the parameters that dictate bursting powers including alternative absorbers such as nIR-plasmonic nanoparticles - Au/SiO_2 nanoshells,[14] encapsulation of lower boiling point liquids, and adjusting MC wall thicknesses.

4.6 Conclusion

We have demonstrated the concept of phototriggerable, liquid-filled microcapsules via co-encapsulation of absorbing species using a simple and robust interfacial polymerization technique. The solid polyamide shell provides substantial protection from the external environment to its encapsulated liquid contents but remains breachable upon irradiation. We have demonstrated the concept of storage and remote release with mutually reactive small molecules and catalysts. The technology has been extended to include wavelength specific bursting conditions. This allows for multiple types of microcapsules to coexist and be selectively burst on demand.

---

1 (a) De Geest, B.G.; McShane, M.J.; Demeester, J.; De Smedt, S.C.; Hennink, W.E. *J. Am. Chem. Soc.* **2008,** *130,* 14480-14482 and references therein. (b) Mathiowitz, E.; Cohen, M. D. *J. Membrane Sci.* **1989,** *40,* 67-86.

2 Yow, H.N.; Routh, A.F. *Soft Matter* **2006**, 940-949.

3 White, S.R.; Sottos, N.R.; Geubelle, P. H.; Moore, J.S.; Kessler, M.R.; Sriram, S.R.; Brown, E.N.; Viswanathan, S. *Nature* **2001,** *409,* 794-797.

4 Santini, J.T.; Richards, A.C.; Scheidt, R.; Cima, M.J.; Langer, R. *Angew. Chem. Int. Ed.* **2000**, *39,* 2396-2407.

5 Misawa, H.; Kitamura, N.; Masuhara, H. *J. Am. Chem. Soc.* **1991,** *113,* 7859-7863.

6 For selected Au examples see: (a) Radt, B.; Smith, T, A.; Caruso, F. *Adv. Mater.* **2004,** *16,* 2184-2189. (b) Skirtach, A. G.; Karageorgiev, P.; Bédard, M. F.; Sukhorukov, G. B.; Möhwald, H. *J. Am. Chem. Soc.* **2008,** *130,* 11572-11573. For selected Ag examples see: (c) Radziuk, D.; Shchukin, D. G.; Skirtach, A. G.; Möhwald, H.; Sukhorukov, G. B. *Langmuir* **2007,** *23,* 4612-4617.

7 Yang, Z. P.; Ci, L.; Bur, J. A.; Lin, S. Y.; Ajayan, P. M. *Nano Lett.* **2008,** *8*, 446-451.

8 Mathiowitz, E.; Cohen, M. D. *J. Membrane Sci.* **1989,** *40*, 1-26.

9 (a) Mathiowitz, E.; Cohen, M. D. *J. Membrane Sci.* **1989,** *40*, 1-26. (b) Mathiowitz, E.; Cohen, M. D. *J. Membrane Sci.* **1989,** *40*, 27-41. (c) Mathiowitz, E.; Cohen, M. D. *J.*

Membrane Sci. **1989,** *40*, 43-54. (d) Mathiowitz, E.; Cohen, M. D. *J. Membrane Sci.* **1989,** *40*, 55-65. (e) Mathiowitz, E.; Cohen, M. D. *J. Membrane Sci.* **1989,** *40*, 67-86

10 Near-IR is attractive as it lies outside the optical absorption window of many organics.

11 Goodwin, R. D. *J. Phys. Chem. Ref. Data* **1989**, 18, 1565-1636.

12 Rodionov, V. O.; Presolski, S. I.; Gardiner, S.; L, Y-.H.; Finn, M. G. *J. Am. Chem. Soc* **2007,** *129*, 12696-12704.

13 IR 783 was not sufficiently soluble in organic solvents and when exposed to amines exhibited a blue shift in the absorption.

14 Cole, J. R.; Mirin N. A.; Knight, M. W.; Goodrich, G. P.; Halas, N. J. *J. Phys. Chem. C.* **2009,** *113*, 12090-12094.

Chapter 5:

Conclusions

We have extended the field of optothermally responsive materials to encompass three temperature dependent responses: surface energy, surface tension, and pressure. For all three applications we utilized the advantageous optothermal properties of carbon nanotubes to convert light energy into heat. By incorporating the nanotubes into functional composites they can be tailored to transfer heat appropriately for each application and produce interesting responses.

To modulate surface energies and remotely control the wettability of a surface we utilized the inherent topology and highly absorbing nature of vertically aligned carbon nanotubes as a coating material. To produce optothermally responsive wettabilities we developed a chemical vapor deposition technique to produce robust nanotube forests and a UV activated nanotube functionalization method that allowed the polymerization of *poly*-NIPAAm on the surface. This resulted in optothermal contact angles switches greater than 70º. The versatility of the functionalization technique also allowed for the formation of patterned superhydrophilic/superhydrophobic arrays.

The optothermal manipulation of surface tensions on the surface of a liquid provides an example of a direct means of converting solar energy into locomotion. Controlled linear motion, rotational motion, and volumetric expansion were realized with vertically aligned nanotube-plastic composites. This work may be scaled down to the microscale for application in microfluidic rotary pumps or controlled motion of micro-objects. Future work requires the production of composites that use the principle of wavelength specific absorption to produce controlled motion.

Optothermal modulation of the pressure of a liquid confined within an impermeable microcapsule has allowed for the remote initiation of the release of the encapsulated material. When a highly reactive species is stored in intimate contact with a reactive environment, remote triggering can result in small molecule synthetic reactions or a rapid polymerization. This technique has been extended to include wavelength specific bursting with the potential for complex reactions on demand.

The ability to harness the power of light in the form of heat and utilize it to produce interesting responses expands upon an under explored direction in the field of light responsive materials. Our investigation of optothermally modulated surface energy, surface tension, and pressure only begins to uncover the implications for these systems. In fact, the optothermal modulation of many temperature dependent phenomena remains completely uninvestigated. The results of these experiments have implications for fields as diverse as organic synthetic chemistry, adhesives, offset printing, microfluidic pumps, drug delivery, and self-cleaning surfaces.

Part II:

Carbon Nanotube Photovoltaics

Chapter 6:

Carbon Nanotube – Polymer Photovoltaics

With a looming energy crisis the development of methods for the cost-effective utilization of renewable resources is essential, with photovoltaics holding significant promise. Polymer based photovoltaics offer a robust, potentially economical alternative to the fragile and expensive silicon-based solar technology.[1] Specifically, they offer mechanical flexibility, a high degree of chemical and electronic tailorability, a high absorption coefficient, a low cost of fabrication, and a potential ease of processing. Conjugated polymers suitable for photovoltaics have low dielectric constants and thus shield charges poorly. As a result, light absorption produces a strongly bound electron-hole pair, or exciton. To extract free charges, the exciton must be split at an energetically suitable boundary, commonly referred to as donor/acceptor interface, from which the free charges can migrate to their respective electrodes. The lifetime of the exciton is on the order of 10^{-9} s which translates to a diffusion lifetime distance between 5 and 10 nm.[1] As a result, it is necessary for the donor and acceptor to be intimately mixed to increase the interfacial area and the likelihood of charge separation. This issue is resolved for polymer-based photovoltaic cells through a bulk heterojunction architecture, where the donor and acceptors are mixed to form a bi-continuous network. Devices using *poly*(3-hexylthiophene):[6,6]-phenyl-C_{61}-butyric acid methyl ester (P3HT:PCBM) blends have obtained efficiencies on the order of ~5% and exhibit robust processing capabilities.[2] However, fullerenes are not necessarily the optimal acceptor material for use in bulk heterojunction solar cells based on their minimal absorption of visible light, relatively high weight percentage of fullerene required (generally 45-80%)[1,3] and the tendency of fullerenes to phase segregate in polymer blends.[4] A variety of alternatives ranging from inorganic nanoparticles[5] and electron transporting polymers[6] to carbon nanotubes[7] have been investigated. Semiconducting single walled carbon nanotubes (SWNTs)[8] are especially attractive as electron accepting materials for solar cell applications[9] based on several potential advantages that they offer relative to fullerenes, such as a high aspect ratio, which could allow lower acceptor loadings,[10] and enhanced mechanical strength[11] for the realization of robust, flexible devices. Nonetheless, carbon nanotubes also present various challenges, such as insolubility, sample inhomogeneity (due to metallic and semiconducting components), and a propensity for phase segregation or bundling.

As a potential electron transporting component for organic photovoltaics an understanding of the physical and electronic properties of SWNTs is important.[12] Physically, SWNTs are single layer cylinders of sp^2-bonded carbon, with diameters on the order of a nanometer and lengths of hundreds to thousands of nanometers. Such high aspect ratios allow percolation of polymer networks at very low loading, ranging from 0.001 – 1 wt%.[13] For photovoltaic devices this would imply efficient charge extraction with minimal volume filling compared to the 45-80% fullerene necessary to fully percolate the polymer. By decreasing the non-absorbing electron transporting component of the active layer the thickness of the devices could be decreased while maintaining complete absorption. Thinner devices should result in lower series resistances and thus higher currents. To obtain efficient nanotube percolation the strength of the interaction between the polymer and the SWNTs must be optimized. For solubilizing carbon nanotubes both covalent and supramolecular strategies have been employed, although supramolecular interactions offer the advantage that the electronic structure of the carbon nanotube is not compromised.[14] We report here the investigation of a novel compatibilizing polymer.

The electronic properties of SWNTs are highly dependent on their physical structure. Specifically, the manner in which they are wrapped, their chirality (designated as (n, m)) strongly influences their band structure, varying between metallic and semiconducting.[15] To

facilitate charge separation and act as the electron transporting component, SWNTs must be semiconducting, thus a method for obtaining only semiconducting SWNTs is necessary. Synthetic methods have realized limited success isolating semiconducting or metallic SWNTs, though significant diameter control has been realized.[16] To this end considerable effort has been put forth to chemically[17] and physically[18] isolate semiconducting nanotubes based on their electronic structure and diameter. We investigated techniques reported to selectively functionalize or physically separate metallic SWNTs, though with minimal success. In an effort to overcome the presence of metallic carbon nanotubes we turned toward alternative device architectures including bulk heterojunction, bilayer, and horizontal, gated architectures.

Here we discuss our work investigating the utilization of nanotubes for organic photovoltaic applications, including: tailoring supramolecular interactions to homogenize nanotube/polymer composites; isolating semiconducting SWNTs; and constructing bulk heterojunction, bilayer, and horizontal photovoltaic devices.

6.1 Polymer-Nanotube Supramolecular Compatibilization

Relatively little work has been focused on the development of conjugated polymers that have a high affinity for nanotubes through supramolecular interactions that not only solubilize the nanotubes, but also lead to solution processable two-component blends. One of the best examples of a conjugated polymer with a high affinity for nanotubes is the polymer poly[(*m*-phenylenevinylene)-*co*-(2,5-dioctoxy-*p*-phenylene-vinylene)] (PmPV) which is known to strongly interact with carbon nanotubes via a suspected wrapping mechanism,[19] although the absorption of light is limited primarily to ultraviolet. A more attractive route to a conjugated polymer with a high affinity for carbon nanotubes and electronic properties suitable for solar cells, is to focus on analogues of P3HT, which has proven to be the most successful polymer in fullerene-based photovoltaics. Pristine poly(3-octylthiophene) (P3OT) has been found to give operational devices in blends with SWNTs, although power conversion efficiencies of <0.1% have been reported.[20] Since the electronic structure of SWNTs are compatible with accepting electrons from P3OT, such low efficiencies are perhaps due to the lack of any specific interaction between P3OT and the nanotubes, leading to a less than ideal composite microstructure. Pendant functionalization of polythiophenes is a way to induce functionality capable of strong interaction with carbon nanotubes, as a tool to generate bicontinuous networks of intimately mixed donor and acceptor while retaining the all thiophene backbone. A clear choice for such pendant functionalization is the polycyclic aromatic hydrocarbon Pyrene, which is known to give strong π-π interactions with carbon nanotubes and has been previously exploited as a pendant group in acrylate and styrenic copolymers for the purpose of solubilizing carbon nanotubes.[21] Pyrene is also of interest as it has been used as a small molecule dye in poly(3-octylthiophene)-SWNT solar cells as a sensitizing agent, resulting in significant improvement of device performance even in the absence of any specific interaction between the polymer and the dye functionalized nanotubes. As such, we report here the synthesis of a Pyrene functionalized alkylthiophene copolymer (Scheme 7.1) which promises to be an effective polymer for nanotube composite solar cells based on the ability of this polymer to form homogenous solution cast nanotube composite thin films and the electronic properties of this polymer which establish it as a viable material for use in solar cells.

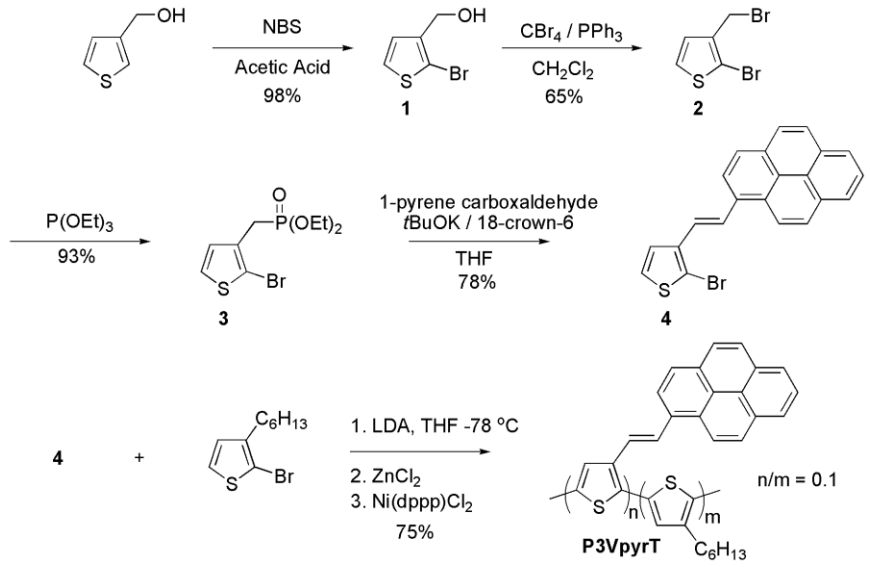

Scheme 7.1

The synthesis of the Pyrene-functionalized 3-alkylthiophene copolymer (poly(3-(2-(pryen-1-yl)vinyl)thiophene-*co*-3-hexylthiophene)) (P3VpyrT) is illustrated in Scheme 7.1 and was performed by Dr. Barry Thompson. Monomer synthesis begins with the commercially available 3-thiophene methanol and proceeds via bromination of the thiophene ring followed by conversion of the alcohol to the primary bromide **2**. Conversion to the corresponding phosphonate ester (**3**) allows subsequent coupling via the Horner-Emmons reaction with 1-pyrene carboxaldehyde to yield compound **4** as a mixture of the *trans* and *cis* olefins in a ratio of 7:3 as determined by ^{1}H NMR (see supporting information). Copolymerization of **4** (0.15 mol%) with 2-bromo-3-hexylthiophene (0.85 mol%) using the McCullough method for regioregular polythiophene synthesis[22] led to the random copolymer P3VpyrT which contained ~10 mol% of the Pyrene substituted repeat unit as determined by ^{1}H NMR. The molecular weight was found to be 10,150 g/mol (M_n) by SEC in dichlorobenzene (vs. PS standards) and the polymer was found to be soluble in a variety of common organic solvents including chloroform, THF, and dichlorobenzene.

6.1a Electronic Characterization

The electronic properties of P3VpyrT were investigated by UV-visible absorption spectroscopy in spin-cast films (chlorobenzene) as well as by cyclic voltammetry as drop cast electrode bound films. Figure 6-1a shows the absorption spectra of the polymer relative to P3HT. It can be seen that the absorption onset for P3VpyrT occurs at roughly the same wavelength as that for P3HT, suggesting that the two materials have approximately the same band gap. The major difference in the spectra can be seen at short wavelengths, where a strong shoulder centered at 400 nm in P3VpyrT corresponds to the contribution of the Pyrene dye, which is in direct conjugation with the polymer backbone. This type of broadened absorption

spectra has been previously observed in 3-vinyl substituted Polythiophene copolymers.[23] The electrochemical response for P3VpyrT shows a similar onset of oxidation to P3HT at ~0.45 V vs. Fc/Fc^+, indicating a similar HOMO level of about 5.5 eV relative to vacuum, based on the assumption that the Fc/Fc^+ redox switching potential is ~5.1 eV below the vaccum.[24] Overall P3VpyrT appears to have a very similar electronic structure to P3HT with the added advantage of a broadened absorption spectrum. As further proof of concept that this novel polymer possesses suitable characteristics for use in solar cells, the hole mobility of the polymer was also examined using the space charge limited technique.[25] The mobility of a P3HT sample was found to increase from 2.25 x 10^{-4} $cm^2V^{-1}s^{-1}$ to 5.33 x 10^{-4} $cm^2V^{-1}s^{-1}$ as a consequence of annealing at 150 ºC for 30 minutes, while P3VpyrT was found to undergo an increase from 5.48 x 10^{-5} $cm^2 V^{-1}s^{-1}$ to 1.33 x 10^{-4} $cm^2V^{-1}s^{-1}$ under the same conditions, indicating similar hole conduction proerties to P3HT.

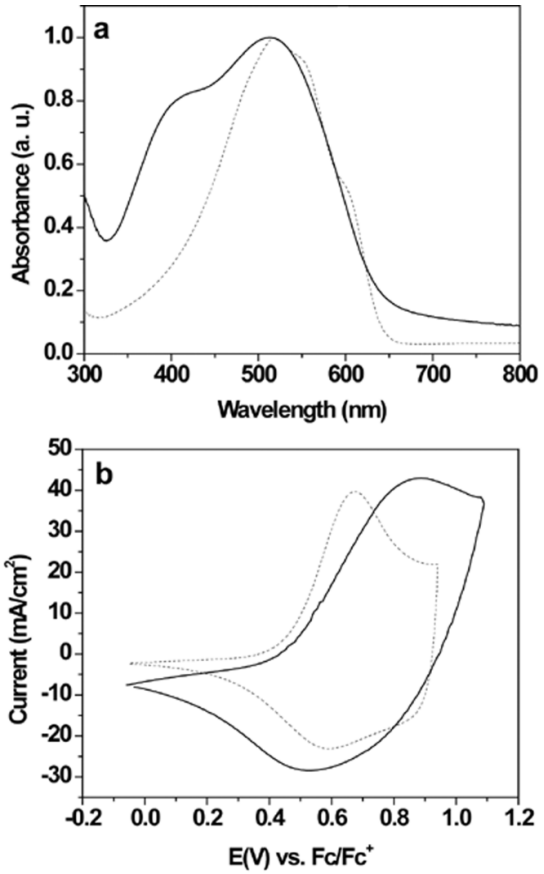

Figure 6-1. UV-Visible absorption spectra (a) for spin cast thin films of P3VpyrT (solid line) and P3HT (dashed line). Cyclic voltammograms (b) for P3VpyrT (solid line) and P3HT (dashed line) collected using thin polymer films drop cast on a Pt button electrode in 0.1M $TBAPF_6$ / acetonitrile at 50 mV/s using a silver wire pseudo-reference electrode calibrated vs. Fc/Fc+.

6.1b Electron and Optical Microscopy Characterization

As a means to evaluate the physical interaction between P3VpyrT and carbon nanotubes, spin coated composites were studied by TEM (Figure 6-2). Efforts to visualize HiPCO SWNTs in polymer nanotube blends proved to be uninformative due to difficulties in imaging the SWNTs within the films of P3VpyrT and P3HT (Figure 6-2). In order to establish the role of the covalently bound Pyrene moiety in P3VpyrT for enhancing the compatibility of polymer and nanotube relative to P3HT composites, multi-walled nanotubes were utilized as prepared by the water-assisted chemical vapor deposition method originally described by Ijima.[26] The nanotubes were observed by TEM to contain between 1-5 walls with average diameters of 8-10 nm and lengths on the order of tens of microns. These nanotubes were selected in favor of SWNTs for imaging purposes based on the ease of visualization. Polymer-MWNT composites containing 10 wt% of nanotube relative to the polymer (10 mg/ml) were prepared by blending P3VpyrT and P3HT with multi-walled carbon nanotubes, by first dispersing the nanotubes in dichlorobenzene under ultrasonication conditions, followed by addition of the polymer to the solution. The solutions were then stirred overnight at room temperature. At a concentration of 10 mg/mL in polymer, all solutions were opaque. Upon dilution with dichlorobenzene, the solutions based on P3HT and nanotubes remained opaque and somewhat cloudy, while the solutions based on P3VpyrT and nanotubes were more transparent and free of noticeable cloudiness.

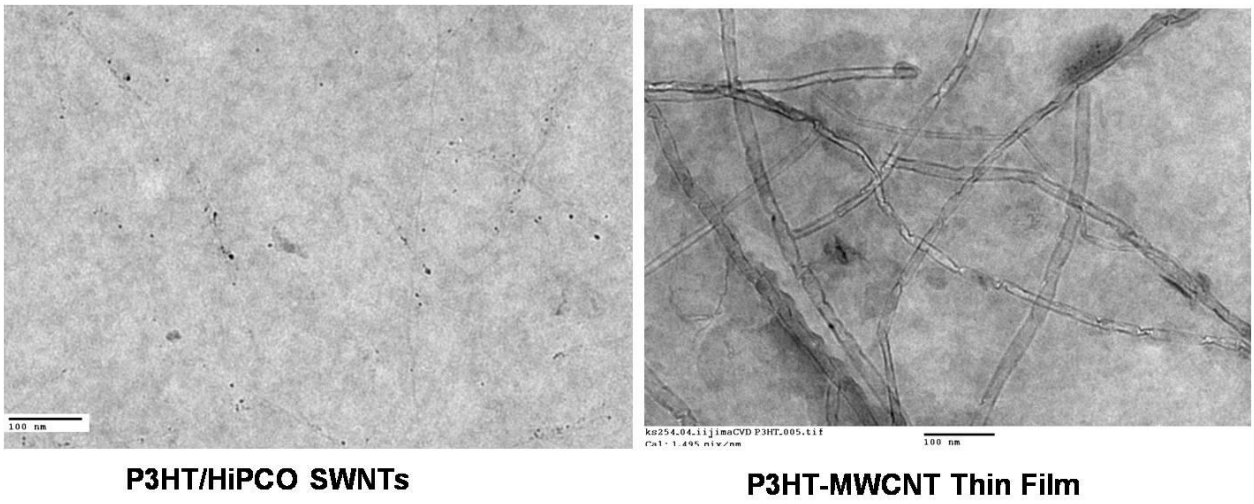

Figure 6-2. Transmission Electron Micrographs of P3HT-nanotube films. Scale bars indicate 100nm. MWNTs are considerably more easily visualized but significant information regarding macroscale assembly is elusive.

The solutions (10 mg/ml in polymer) were used directly to spin coat films onto salt plates for liftoff and analysis by TEM. While TEM did allow direct imaging of MWNTs it did not reveal an obvious difference between the two types of composites. Use of optical microscopy (Figure 6-3) revealed the superior ability of P3VpyrT to generate homogenous composite thin films in blends with MWNTs. Figure 6-3 illustrates a comparison between the optical micrographs of P3HT-MWNT (Figure 6-3a) composites with P3VpyrT-MWNT (Figure 6-3c) composites using a control film spin coated from a dichlorobenzene that was 10 mg/ml in P3HT with 10 wt% MWNT and 13 wt% *N*-(1-pyrenyl)maleimide relative to P3HT. This control is relevant as the 13

wt% of added Pyrene dye closely matches the Pyrene content of P3VpyrT as well as the relative amount of the same dye that was reported for use in P3OT-pyrene dye-SWNT solar cells.[20] From the images in Figure 6-3, it is clear that P3HT-MWNT (Figure 6-3a) and dye doped P3HT-MWNT (Figure 6-3b) composites form highly non-uniform films with regions of locally high MWNT concentration dispersed throughout the films. In contrast, Figure 6-3c shows that a film prepared from P3VpyrT-MWNT blend solutions under the same conditions. The film is significantly more uniform than the P3HT based films and suggests that P3VpyrT is interacting more strongly as a dispersing agent with the MWNTs even at this high concentration of nanotubes. This result suggests that P3VpyrT is a potentially useful electroactive polymer for the realization of polymer-NT composite solar cells, which is the focus of continuing work. The next steps are the isolation of semiconducting SWNT and the production of photovoltaic devices.

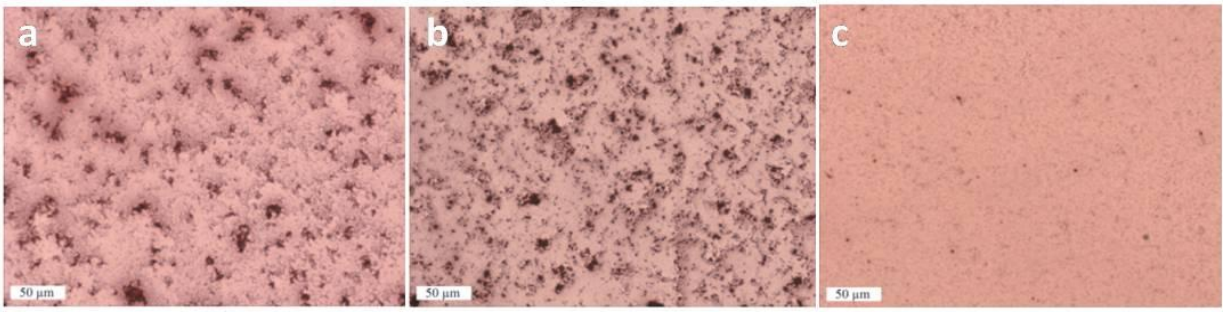

Figure 6-3. Optical microscope images recorded at 20X magnification for (a) P3HT-MWNT (10 wt%), (b) P3HT-dye (13 wt%)–MWNT 10 wt%, (c) **P3VpyrT**-MWNT composites cast from dichlorobenzene solution at a concentration of 10 mg/ml in polymer.

6.2 Isolating Semiconducting SWNTs

To produce devices with donor/acceptor interfaces suitable for exciton dissociation and photovoltaic devices, only small diameter, semiconducting SWNTs can be used. As all as-grown SWNTs contain both semiconductors and metals a means of enacting separation or selectively deactivating the metallic SWNTs is necessary. To this end we attempted to evaluate two literature procedures: the chemoselective functionalization of metallic SWNTs[27] using diazonium salts; and the physical separation using polymer or surfactant wrapping and centrifugation.

6.2a Selective Functionalization

Originally published by Smalley et al.[27] and later expanded by Tour et al.,[28] electrophilic diazonium based functionalization of SWNTs has been shown to first functionalize metallic SWNTs due to their electron rich nature. The basic functionalization scheme is shown in Figure 6-4. Briefly, SWNT are dispersed in an aqueous surfactant and then exposed to a low concentration of a diazonium salt, such as 4-chlorobenzenediazonium tetrafluoroborate. The electrophilic diazonium salt first reacts with the metallic SWNTs, which have a greater population close to the Fermi level. The functionalized metallic SWNTs can then be separated

from the bulk. Our plan was to isolate a population of semiconducting SWNTs and then fabricate polymer-SWNT photovoltaic devices.

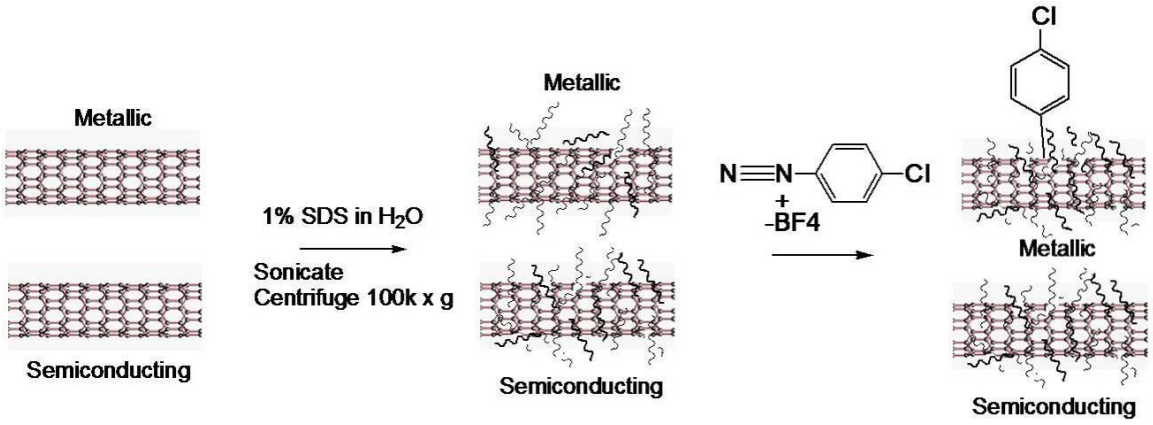

Figure 6-4. Semiconducting nanotube purification. SWNTs are first suspended in surfactant solution and sonicated and centrifuged to remove bundles.

To synthesize the diazonium salt we added nitrosonium tetrafluoroborate (15.6 mmol) to a dry flask in an inert atmosphere. Acetonitrile (10 mL) was added to the flask and the solution cooled to -30 □C. A solution of 4-chloroaniline (12.95 mmol) in acetonitrile (5 mL) was then added over 0.5 h. After addition, the mixture was warmed to room temperature and allowed to stir for 1 h prior to dilution with diethyl ether (250 mL). The precipitate was collected to give a light orange solid. This solid was purified by recrystallizing from methanol:hexanes to give a white crystal, verified by melting point and NMR.

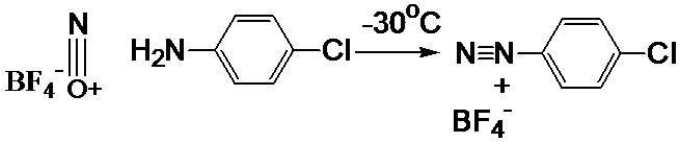

Figure 6-5. Nitrosonium tetralfuoroborate is reacted with 4-chloroanaline to form 4-chlorobenzenediazonium tetrafluoroborate.[29]

The nanotube functionalization procedure was adapted from literature precedent. Briefly, aqueous sodium dodecylsulfate (SDS)-coated SWNTs were loaded into a flask to which 4-chlorobenzenediazonium tetrafluoroborate was titrated. Samples were taken after each addition and monitored by UV-Vis. For well isolated SWNTs, UV-Vis-nIR spectroscopy shows semiconducting SWNTs transitions between 850-1,450 nm and 500-850 nm for the E^S_{11} and E^S_{22} transitions respectively, while metallic SWNTs exhibit an E^M_{11} transition at 420-520 nm.[30] Roughly proportional reduction in absorption peaks between 400-850nm were observed, indicating functionalization, but no selectivity (Figure 6-6). With a lack of selectivity we decided to attempt a physical separation as detailed in the next section.

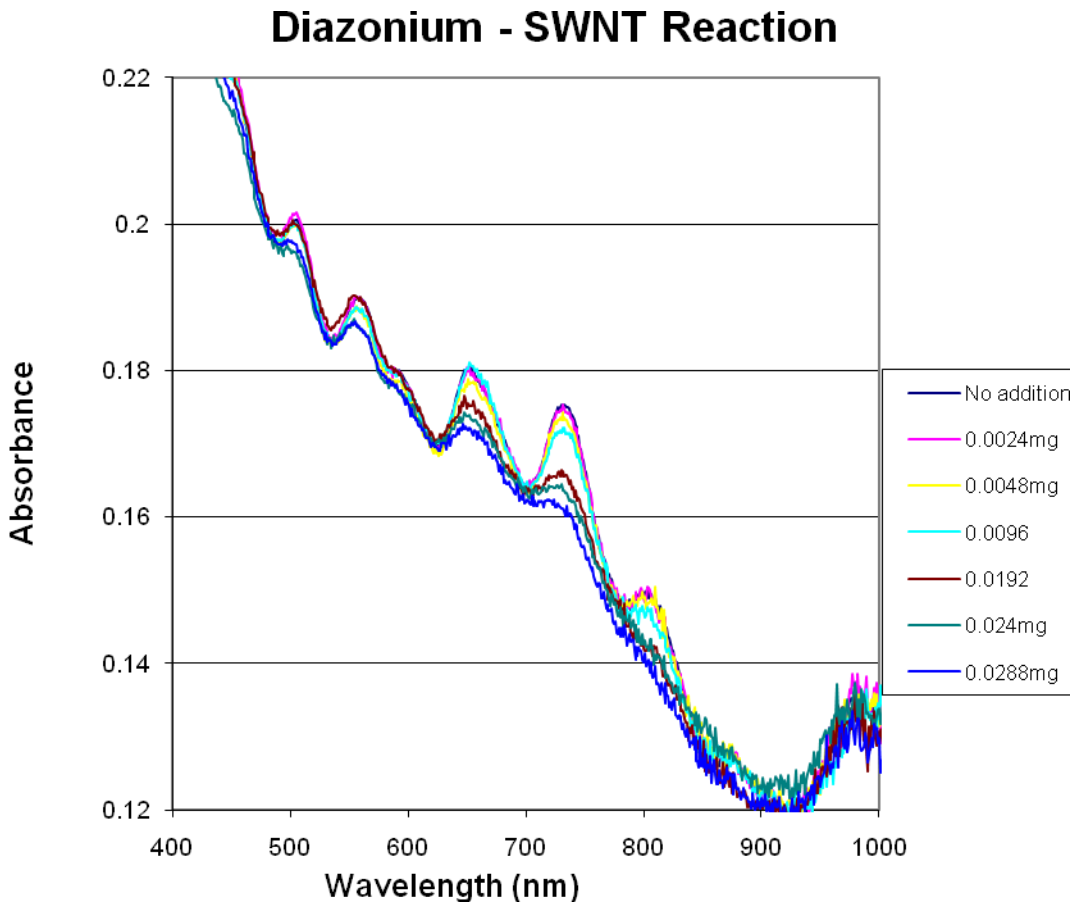

Figure 6-6. UV-Vis absorption spectrum of SWNTs after addition of diazonium salt. Functionalization of the SWNTs is evident by the decrease in the absorption peaks across the spectrum. Semiconducting and metallic nanotubes appear functionalized.

6.2b SWNT Separation: Polymer Wrapping and Density Gradient Centrifugation (with Yao Yue)

Recently two methods have been employed to physically separate SWNTs by chirality: polymer wrapping followed by centrifugation[31] and surfactant wrapping followed by centrifugation through a density gradient. [32] Both methods hold much potential for nanotube purification, but involve wrapping the nanotubes in a supporting material that must be removed prior to incorporation into photovoltaic devices. Despite these drawbacks we attempted to reproduce literature results in an effort to show proof-of-principle SWNT-polymer photovoltaic devices. For this work we used Southwest Nanotechnology CoMoCat SWNTs,[16] for their small diameters and small diameter distribution.

In principle, ultrasonic dispersion of SWNTs in a surfactant such as sodium cholate (SC) results in wrapped nanotubes (SC-SWNTs) of slightly varying density depending on their diameter and electrostatic attraction to the surfactant.[33] SC-SWNTs were subjected to ultracentrifugation at 220,000 x g for 10h, through an iodixanol density gradient to obtain diameter separated SWNT samples. The literature reports centrifuged samples to contain a

variety of bands containing SWNTs and ranging in color from purple to orange to black. Through a number of trials we were unable to reproduce the literature results and could only obtain two bands, a less dense purple band and a denser black band (Figure 6-7).

Figure 6-7. Separation of semiconducting SWCNTs by density gradient ultracentrifugation. The less dense purple band (right). The more dense black band containing mostly SWNT bundles(left).

To analyze the two bands, we fractionated the gradients and performed UV-Vis-nIR absorption and 2D photoluminescence spectroscopies. For well isolated SWNTs, UV-Vis-nIR spectroscopy shows semiconducting SWNTs transitions between 850-1,450 nm and 500-850 nm for the E^{S}_{11} and E^{S}_{22} transitions respectively, while metallic SWNTs exhibit an E^{M}_{11} transition at 420-520 nm.[34] Figure 6-8 shows the absorbance spectrum of SC-SWNTs: pristine, the purple band, and the black band. The purple band and the dispersed SWNTs show similar magnitude peaks in both the semiconducting and metallic regions indicating a poor separation based on electronic character. The black band has noticeably poorly resolved peaks indicating the presence of SWNT bundles. This suggests that density gradient centrifugation in our hands successfully removes SWNT bundles but gives no significant separation based on electronic properties.

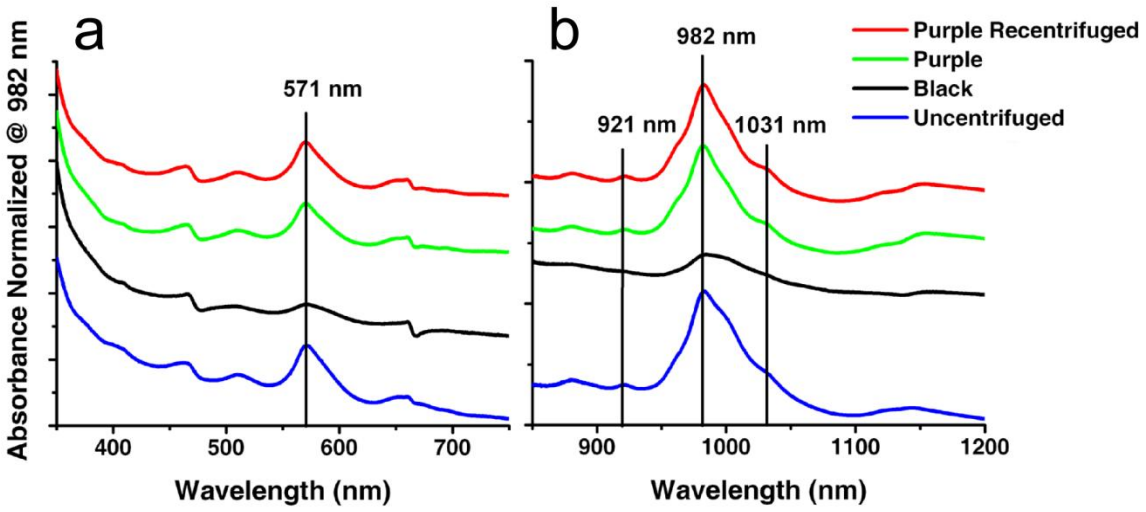

Figure 6-8. Sorting SWCNTs by electronic type using density gradient ultracentrifugation. Samples of CoMoCat SWNTs were separated using ultracentrifugation and fractionated by chromatic differences into a purple layer and a black layer. The increasing absorption at 571 nm, 921 nm, 982 nm, and 1031 nm in the purple sample relative to the black sample and uncentrifuged sample indicate an enhancement of semiconducting SWNTs by centrifugation.

To further characterize the samples we investigated the 2D photoluminescence (PL) of the dispersed SWNTs. Two-dimensional PL looks at the fluorescence of a suspended nanotube sample over a range of excitation wavelengths, giving distinct chirality information for semiconducting SWNTs in a quantitative fashion. As a reference, the excitation/emission peaks have been correlated to specific chirality SWNTs, allowing precise definition of the semiconducting SWNTs in a sample.[35] Unfortunately, metallic SWNTs fluoresce poorly and do not show up in PL so an estimate of electronic separation cannot be made. A typical PL spectrum of CoMoCat SWNT suspended in sodium cholate surfactant is shown in Figure 6-9. SWNTs of five different chiralities are clearly visible. After density gradient centrifugation only three chiralities are present in considerable quantities: (6, 5), (8, 3), and (7, 5). The peak ratio for (6, 5): (8, 3): (7, 5) SWNTs is 2.4: 1.8: 1 for an unpurified CoMoCat SWNT sample, and 3.3: 1.3: 1 after density gradient centrifugation. This shows a significant enrichment in the population of (6, 5) SWNTs and the removal of two chiralities. This data, taken in conjunction with absorbance data indicates that some diameter selectivity was obtained by density gradient centrifugation, but the degree of selectivity was not sufficient to isolate single chirality populations and thus only semiconducting SWNTs.

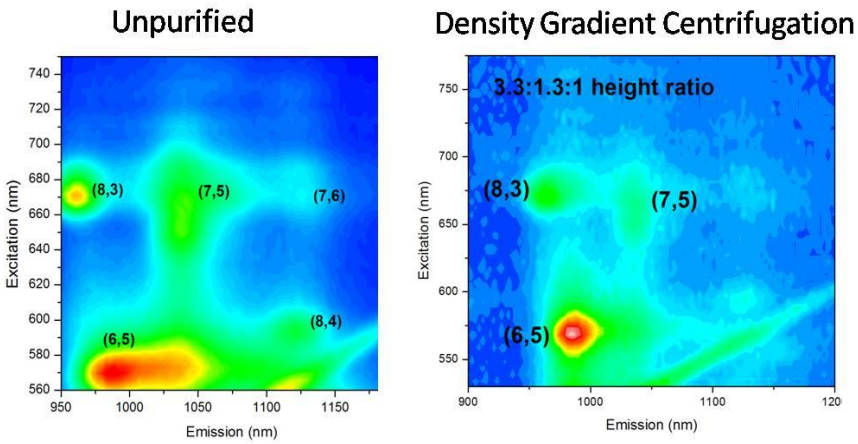

Figure 6-9. Photoluminescence characterization of unpurified and density gradient purified CoMoCat SWNTs. Color indicates magnitude of fluorescence with blue being minimal and white maximum. The peak ratio for (6, 5): (8, 3): (7, 5) SWNTs is 2.4: 1.8: 1 for unpurified CoMoCat SWNTs, and 3.3: 1.3: 1 after density gradient centrifugation. This is clearly a significant enrichment in (6, 5).

To further improve selectivity, we investigated polymer wrapping[31] of CoMoCat SWNTs with poly(9,9-dioctylfluorenyl-2,7-diyl) (PFO) followed by centrifugation at 85,000 x g. This simple procedure, as detailed in reference 31, produced low concentration samples highly enriched in (7, 5) SWNTs by PL (Figure 6-9). This high degree of selectivity is highly attractive, though removal of the wrapping surfactant remains a challenge. In hopes that other conjugated polymers could enact similar separations we investigated P3HT polymer wrapping followed by centrifugation but were unable to characterize the resulting separation due to the strong fluorescence signal from the conjugated polymer. Future work should investigate the removal of the P3HT via dialysis or filtration followed by resuspension of the NTs in surfactant for PL characterization.

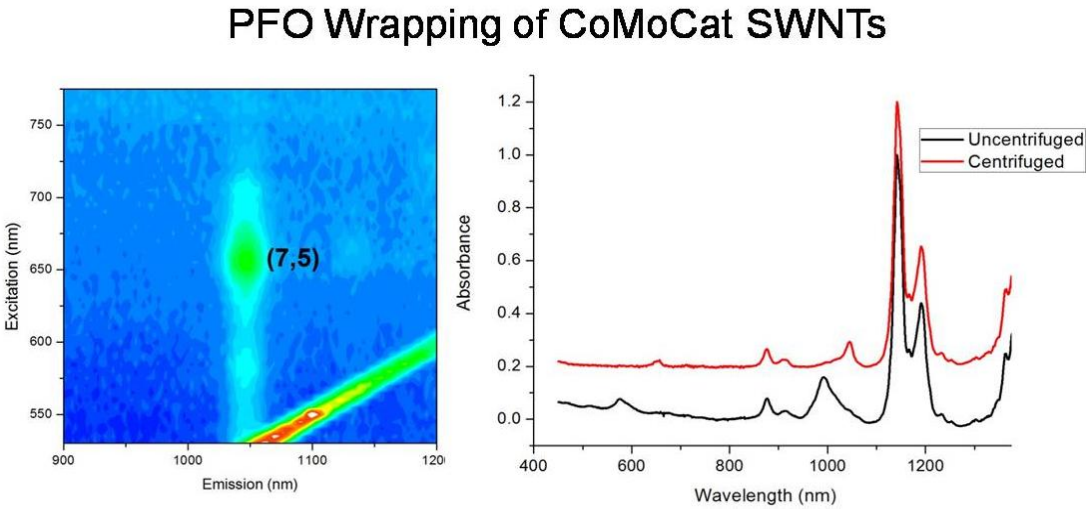

Figure 6-10. Spectroscopic characterization of PFO wrapped SWNTs. PL (left) and UV-Vis-nIR absorbance (right). PL shows predominantly (7, 5) SWNTs.

6.3 Device Fabrication and Testing

6.3a Bulk Heterojunction Devices

Photovoltaic devices were constructed in a layered structure with the photoactive layer consisting of SWNTs and P3HT or P3VpyrT sandwiched between two electrodes, ITO and Al. Glass substrates coated with a 150 nm sputtered ITO pattern of 20 Ω/sq resistivity were obtained from Thin Film Device, Inc. The ITO-coated glass substrates were ultrasonicated for 20 min each in acetone, and then 2 % Helmanex soap water, followed by extensive rinsing and ultrasonication in deionized water, and then isopropyl alcohol. The substrates were then dried under a stream of air. A dispersion of PEDOT:PSS (Baytron-PH500) in water was filtered (1 μm glass) and spin coated at 3400 RPM for 60 s, affording a ~20-30 nm layer. The substrate was dried for 15 min at 140 □C in air and then transferred into an Argon glove box for subsequent procedures. Separate solutions of polymer and carbon nanotubes were prepared in chlorobenzene or chloroform at a concentration of 30 mg/ml and ~0.1 or ~1 mg/ml respectively. The solutions were stirred for 24 hrs and polymer solution was passed through 0.45μm PTFE syringe filter before they were mixed. The blend solution was applied to the substrate and spun at 1200 RPM for 60 s on top of the PEDOT:PSS layer. The substrates were then placed in an evaporation chamber and pumped down in vacuum (~10^{-7} torr) before evaporating a ~100 nm Al layer through a shadow mask on top of the photoactive layer. The configuration of the shadow mask afforded eight independent devices on each substrate, and each device has an active layer of ~0.03 cm^2. The mechanical removal of part of the organic layer allowed contact with the ITO, and adding conductive paste to the removed area to ensure electrical contact completed the device. Thermal annealing was performed after Al deposition by directly placing the completed device on a temperature-controlled hotplate at 150 □C inside the glove box. Devices were cooled to room temperature before testing. Testing of the devices was performed under an argon atmosphere with an Oriel Xenon arc lamp with an AM 1.5G solar filter. Current–voltage behavior was measured with a Keithley 236 SMU. Eight devices were averaged for each experiment.

All bulk heterojunction devices made with SWNTs and P3HT were characterized by extremely low shunt resistances (i.e. shorting). This prevented observation of substantial photocurrent and open circuit voltages. The low shunt resistance is assumed to be the result of two factors: a high conductivity mismatch between SWNTs and the polymers, and the propensity for carbon nanotubes to aggregate, resulting in large bundles spanning the electrodes. We had anticipated that suspension of the SWNTs in solution with P3VpyrT would increase the compatibility and decrease the likelihood of bundles shorting the devices. Unfortunately this was not the case, and all SWNT:P3VpyrT devices shorted. This suggests two things: that the substantial conductivity mismatch between SWNTs and polymer must be dealt with to obtain efficient devices and the isolation of semiconducting nanotubes is likely necessary. To work around our inability to isolate semiconducting SWNTs and increase the shunt resistance and eliminate shorting, we turned to a bilayer architecture in which the polymer component and the nanotube components form two separate layers (Figure 6-11).

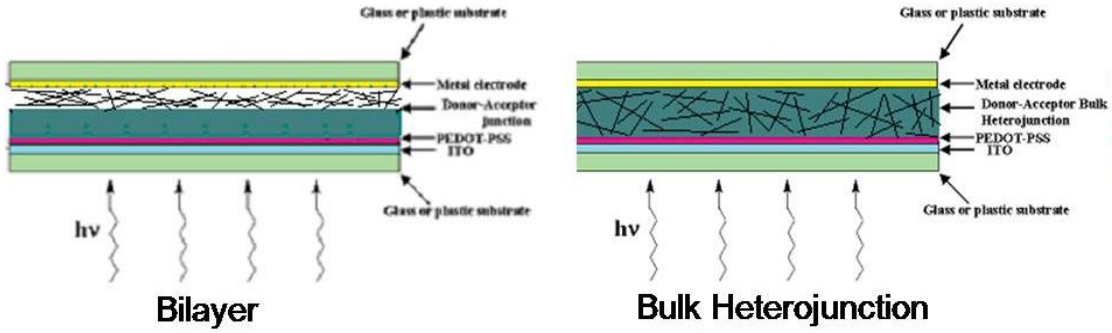

Figure 6-11. Schematics depicting various potential device architectures.

6.3b Bilayer Devices

As shown in Figure 6-11, bilayer devices consist of a p-type layer and an n-type layer sandwiched between two electrodes. In this configuration anticipated efficiencies are small, as the effective active layer is only within the exciton diffusion length of the interface, but the conductivity of a single layer should not dominate the device and photovoltaic properties can be observed and evaluated. We compared SWNT:P3HT and SWNT:P3VpyrT devices and found that both could produce photovoltaic effects (Figure 6-12).

A difficulty with fabricating bilayer devices is that for one layer to be spun on top of another the two materials have to have orthogonal solubility (i.e. are insoluble in a solvent that the other is soluble in). SWNTs have limited solubility in all solvents, though repeated sonication, centrifugation, and decanting the supernatant results in low concentrations of suspended SWNTs in chloroform or ethanol. Briefly, devices were fabricated by spin casting the polymer out of chlorobenzene onto an ITO:PEDOT:PSS substrate. SWNTs were then cast out of EtOH. The top contact was thermally evaporated as discussed for bulk heterojunction devices. The reverse architecture was also investigated, where SWNTs were spun directly onto the ITO:PEDOT:PSS substrate from chloroform and the polymer was cast on top of it. Surprisingly, we found appreciable efficiencies with an ITO:PEDOT:CNT:P3HT:Al device conformation, with negative photocurrents (Figure 6-12). This indicates that the SWNTs are acting as hole transporters and the polymer is acting as an electron transporter. Though it is difficult to make a conclusion regarding the precise cause of the results, two possible scenarios exist: oxygen or defect doping of SWNTs during purification and handling results in p-type transport; or the SWNTs are simply acting as extended metallic electrodes into the P3HT layer. Efficiencies for ITO:PEDOT:CNT:P3HT:Al devices ranged from 0.001 % to 0.002 % with annealing. To improve photon conversion efficiency we moved to a hybrid bulk heterojunction / bilayer device architecture where a BHJ of nanotubes and conducting polymer is spun onto a surface, followed by quickly spin-coating another conducting polymer buffer layer. Devices were made using P3VpyrT/SWNT:P3HT and produced a V_{oc} of as high as 0.38 V and I_{sc}'s of 2 uA after annealing. This translates to efficiencies on the order of 0.005 %. Though these efficiencies are small, they suggest that SWNTs may be a suitable component for organic photovoltaic devices, in particular because the relatively high V_{oc} indicates a proper band alignment. Unfortunately, without the ability to isolate semiconducting SWNTs the ability to produce functioning macroscopic devices remains limited. As a final means of attempting to remove the metallic

nanotubes we investigated current induced metallic nanotube breakdown,[36] a method that selectively destroys metallic NTs by Joule-heating.

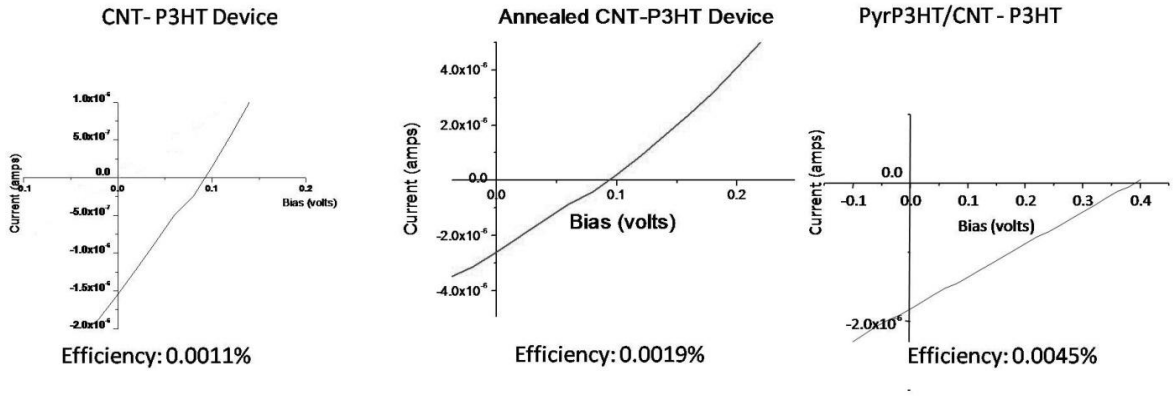

Figure 6-12. Bilayer device current-voltage curves and efficiencies for three devices.

6.3c Microelectrode device construction:

Interdigitated Pd, Ag, or Pt electrodes were patterned onto silicon substrates with 200 nm SiO_2 layer using e-beam lithography in an FEI scanning electron microscope or photolithography and deposited using a Thermionics E-beam evaporator (Brian Kessler). HiPCO or CoMoCat SWNTs were suspended in chloroform via sonication and centrifuged to remove bundles. The supernatant was decanted and used for these studies. A film of nanotubes was then spin-cast onto the substrate from the chloroform solution at 2000 rpm (Figure 6-13). The conductivity of the devices was monitored by current-voltage measurements. Devices were gated to increase the resistance of the semiconducting nanotubes and then subjected to high voltages (10-100 V) to blow out the metallic SWNTs, leaving devices with semiconducting character. Polymer (P3HT) was then deposited by spin coating, in an Argon environment. The substrates were then annealed at 125-150 □C for 10-30 minutes.

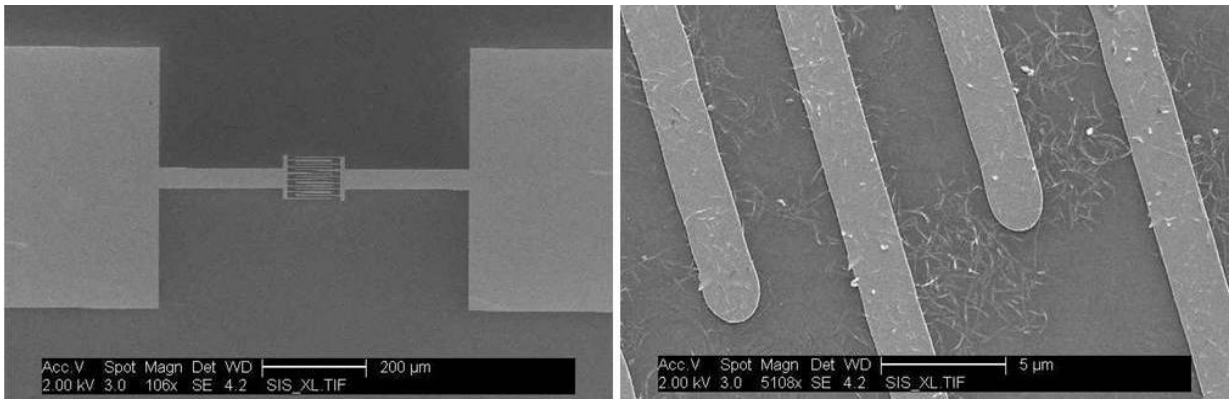

Figure 6-13. SEM Micrographs of interdigitated Pd electrodes. (Left) zoomed out. (Right) zoomed in micrograph showing a nanotube network. Nanotubes are visible as white in color create a continuous network between the electrodes. Nanotubes dark in color are sitting between the electrodes.

Interdigitated electrode device architectures resulted in semiconducting networks of SWNTs. Observation of photocurrent after spin coating a layer of P3HT and annealing at 120 °C for 30 minutes suggests one of two things (Figure 6-14): that charge transfer is occurring between the polymer and the nanotubes; or that an optical gating of the nanotubes is occurring. It is important to note that as the devices have symmetric Pd electrodes one would not expect to observe a photovoltaic effect. The important information from this curve is the relative amount of charge transport at a given bias, and as is shown in Figure 6-14 bottom, the amount of current flowing increases upon illumination with light. In this device current is amplified by ~6-9% on the same order as that reported in the literature.[37]

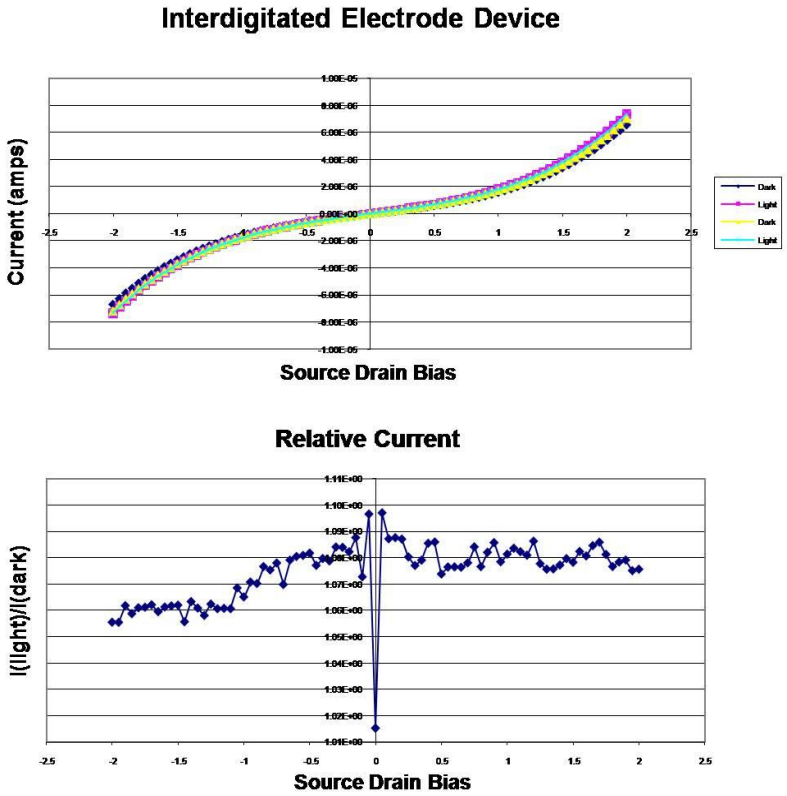

Figure 6-14. (Top) IV curve for a typical device contacted with interdigitated finger electrodes, a layer of SWNTs, and a layer of P3HT. (Bottom) Photocurrent for a given source/drain bias indicate a photoactive affect on the order of 6-9% of the total

To improve device performance we attempted to passivate the silicon surface with a self-assembled monolayer of hexamethyldisilazane (HMDS) prior to SWNT deposition. This greatly enhanced the photocurrents to 5 x base current, as shown in current vs. time curve in Figure 6-15. This hinders charge trapping at the interface between the polymer and the surface, but unfortunately metastable states are still observed after illumination. This is presumably the result of the reaction of hydroxyl moieties on the surface with excited electrons in the polymer. The resulting anions appear to be long lived trapping states, which can act as a negative gate for the nanotube devices, thus influencing their conductivity. Further optimization of monolayer

formation, nanotube deposition, and polymer deposition are required to improve photocurrent on/off ratios. In addition, it is necessary to investigate asymmetric electrodes to observe a photovoltaic effect.

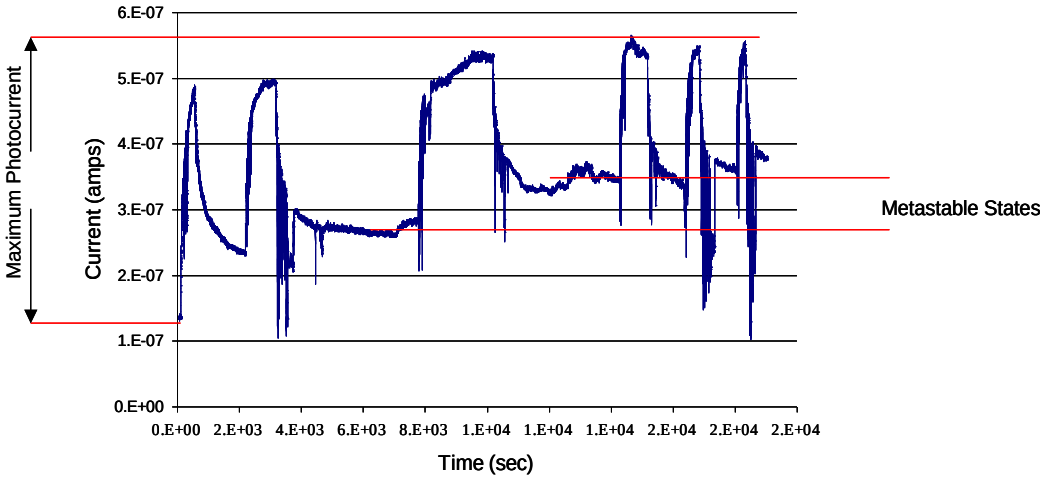

Figure 6-15. Current vs. time upon exposure of an interdigitated electrode bilayer device to light. The light is turned on and off repeatedly resulting in increases and decreases in current respectively. Metastable charge trapped states appear to result in gating of the nanotubes, increasing base current levels.

6.4 Conclusion

To summarize, SWNTs appear to be promising materials for organic photovoltaics. We have successfully investigated polymer functionalization to produce supramolecular interactions and more homogenous polymer/nanotube films. We had limited success reproducing selective nanotube functionalization and centrifugation to remove metallic SWNTs but investigated a variety of device architectures to probe photovoltaic suitability and photocurrent production. Functioning bilayer and hybrid bilayer devices were fabricated with modest efficiencies.

1 Thompson, B. C.; Fréchet, J. M. J. *Angew. Chem. Int. Ed.* **2008,** *47,* 58-77.

2 Li, G. ; Shrotriya, V. ; Huang, J. ; Yao, Y. ; Moriary, T. ; Emery, K. ; Yang, Y. *Nat. Mater.* **2005,** *4*, 864.

3 Shaheen, S. E.; Brabec, C. J.; Sariciftci, N. S.; Padinger, F.; Fromherz, T. *Appl. Phys. Lett.* **2001**, *78*, 841-843.

4 Sivula, K.; Ball, Z. T.; Watanabe, N.; Fréchet, J. M. J. *Adv. Mat.* **2006**, *18*, 206-210.

5 (a) Beek, W. J. E.; Wienk, M. M.; Janssen, R. A. J. *J. Mater. Chem.* **2005**, *15*, 2985-2988. (b) Huynh, W. U.; Dittmer, J. J.; Alivisatos, A. P. *Science* **2002**, *295*, 2425-2427.

6 Koetse, M. M.; Sweelssen, J.; Hoekerd, K. T.; Schoo, H. F. M. ; Veenstra, S. C.; Kroon, J. M.; Yang, X.; Loos, *J. Appl. Phys. Lett.* **2006**, *88*, 083504.

7 (a) Bhattacharyya, S.; Kymakis, E.; Amaratunga, G. A. J. *Chem. Mater.* **2004**, *16*, 4819-4823. (b) Kymakis, E.; Alexandrou, I.; Amaratunga, G. A. J. *J. Appl. Phys.* **2003**, *93*, 1764-1768. (c) Kymakis, E.; Amaratunga, G. A. J. *Appl. Phys. Lett.* **2002**, *80*, 112-114.

8 White, C. T.; Mintmire, J. W. *J. Phys. Chem. B* **2005**, *109*, 52-65.

9 Guldi, D. M.; Rahman, G. M. A.; Zerbetto, F.; Prato, M. *Acc. Chem. Res.* **2005**, *38*, 871-878.

10 Grossiord, N.; Loos, J.; Regev, O.; Koning, C. E. *Chem. Mater.* **2006**, *18*, 1089-1099.

11 Coleman, J. N.; Khan, U.; Gun'ko, Y. K. *Adv. Mater.* **2006**, *18*, 698-706.

12 For a review of the physical and electronic properties of carbon nanotubes: Saito, R.; Dresselhaus, G.; and Dresselhaus, M. S. *Physical Properties of Carbon Nanotubes, 1st ed.;* Imperial College Press: London, 1998.

13 Sandler, J. K. W.; Kirk, J. E.; Kinloch, I. A.; Shaffer, M. S. P.; Windle, A. H. *Polymer* **2003,** *44*, 5893-5899.

14 Star, A.; Liu, Y.; Grant, K.; Ridvan, L.; Stoddart, J. F.; Steuerman, D. W.; Diehl, M. R.; Boukai, A.; Heath, J. R. *Macromolecules* **2003**, *36*, 553-560.

15 Wildoer, J. W. G.; Venema, L. C.; Rinzler, A. G.; Smalley, R. E.; Dekker, C. *Nature* **1998,** *391*, 59.

16 Lolli, G.; Zhang, L.; Balzano, L.; Sakulchaicharoen, N.; Tan, Y.; Resasco, D. E. *J. Phys. Chem. B.* **2006,** *110*, 2108-2115

17 Strano, M.; Dyke, C. D.; Usrey, M. L.; Barone, P. W.; Allen, M. J.; Shan, H.; Kittrell, C.; Hauge, R. H.; Tour, J. M.; Smalley, R. E.; *Science* **2003,** *301*, 1519.

18 Arnold, M. S.; Green, A. A.; Hulvat, J. F.; Stupp, S. I.; Hersam, M. C. *Nature Nano.* **2006,** *1*, 60.

19 (a) Lei, S.-B.; Wan, L.-J.; Wang, C.; Bai, C.-L. *Adv. Mater*. **2004**, *16*, 828-831. (b) Star, A.; Stoddart, J. F.; Steuerman, D.; Diehl, M.; Boukai, A.; Wong, E. W.; Yang, X.; Chung, S.-W.; Choi, H.; Heath, J. R. *Angew. Chem. Int. Ed.* **2001**, *40*, 1721-1725.

20 (a) Bhattacharyya, S.; Kymakis, E.; Amaratunga, G. A. J. *Chem. Mater.* **2004**, *16*, 4819-4823. (b) Kymakis, E.; Alexandrou, I.; Amaratunga, G. A. J. *J. Appl. Phys.* **2003**, *93*, 1764-1768. (c) Kymakis, E.; Amaratunga, G. A. J. *Appl. Phys. Lett.* **2002**, *80*, 112-114.

21 (a) Bahun, G. J.; Wang, C.; Adronov, A. *J. Polym. Sci.: Part A: Polym Chem.* **2006**, *44*, 1941-1951. (b) Lou, X.; Daussin, R.; Cuenot, S.; Duwez, A.-S.; Pagnoulle, C.; Detrembleur, C.; Bailey, C.; Jerome, R. *Chem. Mater*. **2004**, *16*, 4005-4011.

22 McCullough, R. D.; Lowe, R. D.; Jayaraman, M.; Anderson, D. L. *J. Org. Chem.* **1993**, *58*, 904-912.

23 Hou, J.; Huo, L.; He, C.; Yang, C.; Li, Y. *Macromolecules* **2006**, *39*, 594-603.

24 Thompson, B. C.; Kim, Y.-G.; Reynolds, J. R. *Macromolecules* **2005**, *38*, 5359-5362.

25 Goh, C.; Kline, R. J.; McGehee, M. D.; Kadnikova, E. N.; Fréchet, J. M. J. *Appl. Phys. Lett.* **2005**, *86*, 122110.

26 Hata, K.; Futuba, D. N.; Mizuno, Namai, T.; Yumura, M.; Ijima, S. *Science* **2004**, *306*, 1362-1364.

27 Strano, M.; Dyke, C. D.; Usrey, M. L.; Barone, P. W.; Allen, M. J.; Shan, H.; Kittrell, C.; Hauge, R. H.; Tour, J. M.; Smalley, R. E.; *Science* **2003,** *301,* 1519.

28 Kim, W.; Usrey, M. L.; Strano, M. S. *Chem. Mater.*, **2007,** *19,* 1571–1576. Dyke, C. A.; Stewart, M. P.; Tour, J. M. *J. Am. Chem. Soc.* **2005,** 127, 4497–4509.

29 Adapted from Strano, M. et al. *Science* **2003,** *301,* 1519.

30 Fagan, J. A.; Simpson, J. R.; Bauer, B. J.; De Paoli Lacerda, S. H.; Becker, M. L.; Chun, J.; Migler, K. B.; Hight Walker, A. R.; Hobbie, E. K.. *J. Am. Chem. Soc.* **2007,** *129,* 10607-10612.

31 Nish, A.; Hwang, J.; Doig, J.; Nicholas, R. J. *Nature Nano* **2007,** *2,* 640-646.

32 Arnold, M. S., Green, A. A., Hulvat, J. F., Stupp, S. I., Hersam, M. C., *Nature Nano.* **2006,** *1,* 60-65.

33 Procedures can be obtained from: Arnold, M. S., Green, A. A., Hulvat, J. F., Stupp, S. I., Hersam, M. C., *Nature Nano.* **2006,** *1,* 60-65.

34 Fagan, J. A.; Simpson, J. R.; Bauer, B. J.; De Paoli Lacerda, S. H.; Becker, M. L.; Chun, J.; Migler, K. B.; Hight Walker, A. R.; Hobbie, E. K.. *J. Am. Chem. Soc.* **2007,** *129,* 10607-10612.

35 Bachilo, S. M.; Strano, M. S.; Kittrell, C.; Hauge, R. H.; Smalley, R. E.; Weisman, R. B. *Science* **2002,** *298,* 2361.

36 Avouris, P. *Chemical Physics* **2002,** *281,* 429-445.

37 Star, A.; Lu, Y.; Bradley, K.; Gruner., G. *Nano Lett.* **2004,** *4,* 1587.